Synthesis and Properties of Functional Nanoparticle Thin Films

A thesis submitted to attain the degree of

DOCTOR OF SCIENCES of ETH ZURICH
(Dr. sc. ETH Zurich)

presented by

DERYA ERDEM

M.Sc. Metallurgical & Materials Engineer, METU, Turkey
born on 05.09.1986
citizen of Turkey

accepted on the recommendation of
Prof. Dr. Markus Niederberger
Prof. Dr. Laura J. Heyderman
Prof. Dr. Jennifer L. M. Rupp
Prof. Dr. Vanessa Wood
Dr. Nicolas Pilet

2016

Abstract

In this work, a versatile and generalized liquid phase thin film deposition technique, which relies on spin coating of preformed nanoparticle dispersions, is elaborated and exemplified on various multifunctional systems. Existing deposition methodology is engineered and optimized for fabrication of various thin film materials on a wide composition and thickness range, in order to address different application requirements with a single low-cost approach. In the framework of this thesis, a brief explanation of the physical effects is presented in chapter 1 to construct the theoretical background for the understanding of the targeted functionalities in the final thin films. Subsequently, in chapter 2, the essence of the method is shown on crack free ferroelectrically switchable $BaTiO_3$ thin films of macroscopically controlled thickness. The origin of the cracking issue and related thickness threshold during colloidal deposition of thin films is identified as the incomplete outgassing of the organics at the sintering step. Pre-removal of organics in a calcination step at a carefully elaborated temperature aids removal of harsh tensile stresses, which would otherwise lead to crack formation during sintering. As a proof of concept, 3 μm thick crack free $BaTiO_3$ thin films are successfully deposited via repeated spin coating-calcination cycles followed by one sintering step. The ferroelectric switching characteristics of the final films are unambiguously proven by the aid of piezoresponse force microscopy. In chapter 3, the methodology is extended to fabricate crack free $CoFe_2O_4$-SiO_2 nanocomposite thin films in 30-90 wt% SiO_2 composition range for magnetic and magneto-optical applications. It is shown that via SiO_2 incorporation, refractive index, band gap and absorption coefficients can be tuned effectively, which facilitates the integration of $CoFe_2O_4$ based nanostructured thin films into optical systems. Moreover, perpendicular magnetic anisotropy was maintained in thin films of up to 50 wt% SiO_2 content, owing to in-plane tensile stresses imposed from the substrate as a result of constrained sintering conditions. In chapter 4, as a state of art of the presented deposition technique, $BaTiO_3$-$CoFe_2O_4$ based strain mediated magnetoelectric heterostructures are fabricated on a wide thickness and composition range and in two different connectivity schemes to achieve coupling between the ferroelectric and ferromagnetic orders of the composite. For the first composite geometry, $CoFe_2O_4$ has been dispersed into $BaTiO_3$ matrix of 5-50 wt% $CoFe_2O_4$ content, while in the other geometry, multilayered heterostructures are formed via alternating stacks of $BaTiO_3$ and $CoFe_2O_4$ on top of each other. It is shown by the aid of high resolution transmission electron microscopy analysis that formation of intermetallics and smearing of the interfaces in final sintered films for both composite geometries is avoided, which is a prerequisite for an efficient strain mediated magnetoelectric coupling. Impedance and switching spectroscopy measurements on the co-dispersed $BaTiO_3$-$CoFe_2O_4$ nanocomposite thin films point out that only dilute samples of less than 10wt% $CoFe_2O_4$ content can be electrically poled. In addition, magnetic measurements prove the presence of superparamagnetic order in these dilute composites. Finally, the X-ray magnetic circular dichroism measurements at Fe edge indicated formation of an in-plane easy magnetic axis with congruent formation of an out-of-plane hard magnetic axis upon in-plane electrical poling. This shows that strain mediated voltage control of magnetic order at ambient conditions is enabled in nanoparticle based liquid phase processed films, which is shown for the first time for this type of films in the literature to the best of our knowledge. In chapter 5, the presented low-cost thin film deposition approach for systems of various functionalities is concluded with an additional outlook regarding potential applications and device implementation.

Zusammenfassung

In dieser Arbeit wird eine vielseitige und allgemein anwendbare Flüssigphasendünnfilmabscheidetechnik entwickelt und Beispielhaft an verschiedenen multifunktionellen Systemen eingesetzt, die auf dem Spincoaten von vorgeformten Nanopartikeldispersionen basieren. Ein existierendes Abscheideverfahren wird für die Herstellung von verschiedenen Dünnfilmmaterialien mit breitem Zusammensetzungs- und Dickenbereich verwendet, um Anforderungen unterschiedlicher Anwendungen mit einer einzigen, günstigen Methode gerecht zu werden. Im Rahmen dieser Arbeit werden im ersten Kapitel kurz physikalische Effekte erläutert, um den theoretischen Hintergrund für das Verständnis der beabsichtigten Funktionalitäten der fertigen Dünnfilme zu haben. Anschliessend, in Kapitel 2, werden die Grundmechanismen des Beschichtungsverfahrens an rissfreien, ferroelektrisch schaltbaren $BaTiO_3$ Dünnfilmen, mit makroskopisch kontrollierbarer Dicke, gezeigt. Die Ursache eines Rissproblems und des damit verbundenen Dickenlimits während der kolloidalen Abscheidung von Dünnfilmen, wurde als unvollständiges Ausgasen der Organik während des Sinterschrittes identifiziert. Die vorherige Entfernung der Organik in einem Kalzinierungsschritt bei einer präzise bestimmten Temperatur hilft bei der Entfernung von zerstörerischen Zugspannungen, welche ansonsten zur Entstehung von Rissen bei der Sinterung führen würden. Als ein Machbarkeitsnachweis, wurden 3 µm dicke, rissfreie $BaTiO_3$ Dünnfilme erfolgreich mit Hilfe wiederholtem Spincoatings und Kalzinierens, gefolgt von einem einzelnen Sinterungsschrittes, abgeschieden. Die Charakteristika des ferroelektischen Schaltens der fertigen Filme werden mit Hilfe von Piezoresponse Kraftmikroskopie gezeigt. Im 3. Kapitel ist das Verfahren für die Herstellung von rissfreien $CoFe_2O_4$-SiO_2 Nanokompositdünnfilmen erweitert worden, die einen SiO_2 Gehalt zwischen 30 und 90 Gew% aufweisen und für magnetische und magnetooptische Anwendungen geeignet sind. Es wird gezeigt, dass mit der Einbettung von SiO_2 der Brechungsindex, die Bandlücke und der Absorptionskoeffizient effektiv eingestellt werden kann, was eine Verwendung von $CoFe_2O_4$ basierten nanostrukturierten Dünnfilmen in optischen Systemen vorantreibt. Des Weiteren wurde eine senkrechte magnetische Anisotropie in Dünnfilmen mit bis zu 50 Gew% SiO_2 beibehalten, die durch Zugspannungen erzeugt wurden, welche vom Substrat, auf Grund der einschränkenden Sinterbedingungen, verursacht wurden. In Kapitel 4 werden, als modernes Beispiel des gewählten Beschichtungsverfahrens, $BaTiO_3$-$CoFe_2O_4$ basierte belastung vermittellte magnetoelektrische Heterostrukturen in einem ausgedehnten Dicken- und Zusammensetzungsbereich und in zwei verschiedenen Verknüpfungsarten hergestellt, um eine Kupplung zwischen den ferroelektrischen und ferromagnetischen Strukturen des Komposites zu erreichen. Während in der ersten Kompositgeometrie $CoFe_2O_4$ in $BaTiO_3$ mit bis zu 50 Gew% dispergiert wurde, wurden in der zweiten Geometrie Multischichtheterostrukturen mit aufeinander abgeschiedenen $BaTiO_3$ und $CoFe_2O_4$ Schichten hergestellt. Es wird mit Hilfe von hochauflösenden, transmissionsmikroskopischen Analysen gezeigt, dass die Bildung von intermetallischen Phasen und das Verschmieren der Phasengrenze im fertig gesinterten Film für beide Kompositgeometrien verhindert wurden, was eine Voraussetzung für eine effektive, belastung vermittelte magnetoelektrische Kupplung ist. Impedanzspektroskopische und Schaltungs-spektroskopische Messungen an den codispergierten $BaTiO_3$-$CoFe_2O_4$ Nanocompositedünnfilmen zeigen, dass nur verdünnte Proben mit weniger als 10 Gew% $CoFe_2O_4$ elektrisch gepolt werden können. Zusätzlich beweisen magnetischen Messungen das Vorhandensein von superparamagnetischer Ordnung in diesen verdünnten Kompositen. Zuletzt deuten Röntgen-magnetische circular dichroismus-Messungen, bei einer elektrischen Polung der Probe horizontal zur Probenebene, auf die

Bildung einer magnetischen Easy-achse horizontal zur Probenebene mit gleichzeitiger Bildung einer hart magnetischen achse senkrecht zur Probenebene. Dies zeigt, dass Belastung vermittelte Spannungskontrolle von magnetischer Ordnung bei Normalbedingungen in nanopartikelbasierten flüssigphasenprozessierten Filmen möglich ist. Unserem Wissen nach wird dies hier zum ersten Mal für diesen Typ von Film in der Literatur beschrieben. In Kapitel 5 wird das hier vorgestellte günstige Dünnfilmabscheideverfahren für Systeme mit verschiedenen Funktionalitäten noch einmal zusammengefasst und ein Ausblick hinsichtlich möglicher Anwendungen und Device-implementierung wird gegeben.

Contents

Introduction

The use of nanomaterials and nanostructured thin films has undergone a major breakthrough recently, owing to the advances in the synthesis and characterization techniques which provide control and monitoring of the properties down to atomic scales. Emergence of new phenomena at the nanoscale as well as miniaturization demand for increased storage densities[1] are among the main challenges which drive the researches into fabrication and characterization of nanostructured thin films. In this sense; rapid, reliable and low-cost thin film deposition techniques are required to meet the widespread interest in nanostructured thin film based novel devices and applications.

Liquid phase thin film deposition techniques are proven to be versatile low-cost alternative to gas phase deposition techniques. The associated capital costs are one or two orders of magnitude smaller. Moreover, an optimized liquid phase deposition process with improved device properties can be obtained in days, whereas this might take up to months for gas phase techniques. In addition, liquid phase deposition methods offer better control over stoichiometry. Early work involves sol-gel based liquid phase deposition of SiO_2 thin films for anti-reflection coatings,[2] which is readily extended to TiO_2, ZrO_2 and Al_2O_3 coatings.[3] However, the realization of multifunctional thin film structures, such as ferroelectrics and magnetic ceramics, could take place only recently.[4] The main challenges encountered are to account for compositional corrections, either due to loss of highly volatile components or component diffusion into substrate, as well as formation of cracks, side phases and intermediates.[4]

From this aspect, nanoparticle based liquid phase deposition of thin films presents a promising avenue towards nanostructured multifunctional materials with tailored properties, by virtue of the predefined nature of the nanoparticles in terms of stoichiometry, size and crystallinity. In this work, the aim is to engineer a generalized nanoparticle based liquid phase deposition approach, to produce single phase as well as composite multifunctional metal oxide thin films, on a wide thickness and compositional scale, and applicable to different composite geometries. For this purpose, the following milestones paved the way towards a facile and generalized thin film deposition approach:

Optimizing a rapid synthesis method to yield nanoparticles of desired phase and properties, which later serve as nanostructured entities for the functional films

Finding a proper stabilizing agent for highly concentrated nanoparticle dispersions

Engineering the nanoparticle based liquid phase deposition process in order to beat the thickness limit and address different applications with a single method

Taking a further step towards nanostructured composites for fine-tuned properties

Deposition of artificial multiferroic heterostructures with different connectivity schemes; not only to enable the dual presence of multiple ferroic orders, but also to achieve coupling between them

1. Review of related physical phenomena

In this part, some basic concepts of the relevant physical phenomena will be briefly discussed to form a basis for the following representation and discussion of the outcomes obtained within the framework of this thesis.

1.1. Magnetism & materials

Magnetization is a vector sum of induced and permanent magnetic moments per unit volume in a material. In order to study the magnetization behavior of a material under an applied magnetic field, magnetic susceptibility χ concept is introduced and given as:

$$\chi = \delta M/\delta H \quad (1)$$

where M is magnetization and H is external magnetic field. The response of a material to an external magnetic field can be grouped under three categories: diamagnetism, paramagnetism and ferromagnetism. In diamagnetic materials, the magnetic moments in the material align themselves in the opposite direction to the applied magnetic field, and the associated susceptibilities are in the range of -10^{-4} to -10^{-6}. Cu, Ag, Pb, etc. are common diamagnetic materials among others. In paramagnetic materials, the moments are aligned in the parallel direction to the applied field and susceptibility of these materials lies between 10^{-3}-10^{-5}. Al, W, Li can be given as typical examples to the paramagnetic materials.

1.1.1. Ferromagnetism

In ferromagnetic materials, such as Fe, Ni and Co, the magnetic moments are also aligned in parallel direction to the applied magnetic field, however the associated susceptibilities are much larger (10^3 to 10^6) and these materials exhibit spontaneous magnetization. Cooperative alignment of the unpaired spins of the valence electrons due to exchange interactions is responsible for the observed large susceptibilities and spontaneous magnetization phenomena. Briefly, the exchange interactions arise as a result of the Pauli exclusion principle and Coulombic repulsions. Electrons of the same spin are forbidden to share the same orbital according to the Pauli exclusion principle, so they would occupy different orbitals at the same time minimizing the Coulombic repulsions. Especially in the case of 3d transition metals, the wave functions of the d orbitals are narrow and the electrons can easily move to the next vacant orbital according to the Pauli exclusion principle in order to minimize the Coulombic repulsions. This would suggest a shift in the energies of electrons with one spin with respect to the electrons of the opposite spin, which in turn causes imbalanced number of electrons occupying the lower energy level corresponding to a certain spin. Therefore, the material would be spontaneously magnetized even in the absence of an external magnetic field. However, in the case of insulating ferromagnets and 4f metals, the valence electrons are localized and cannot move freely within the band structure. This time, Weiss molecular field theory is applied to explain the driving force for the occurrence of ferromagnetism. In this model, the elementary magnetic moments are strongly coupled to each other due to quantum mechanical exchange interactions, originating from unequal numbers of up and down spin electrons. At high temperatures, thermal entropic effects randomize the magnetic moment alignment of the localized electrons, but at temperatures lower than Curie temperature (T_c), the molecular fields are large enough to spontaneously magnetize the material even in the absence of net magnetic fields. The susceptibilities arising from this kind of exchange is expressed as:

$$\chi = \frac{C}{T - Tc} \quad (2)$$

where C is the Curie constant and T is temperature.

Ferromagnetic Hysteresis

The macroscopic fingerprint of a ferromagnetic material would be its hysteretic type of response to applied cyclic magnetic fields. The hysteresis behavior is explained by the domain model. According to the model, the ferromagnetic materials are subdivided into magnetic domains, which are regions of same spin. The exchange interactions in the material would be minimized if the material consists of a single domain, however this would increase the total energy of the material because of the magnetostatic energy. Therefore, domains form in the structure in order to minimize the presence of any magnetic dipoles at the material surface, thereby minimizing the magnetostatic energy, as depicted schematically in Figure 1.1
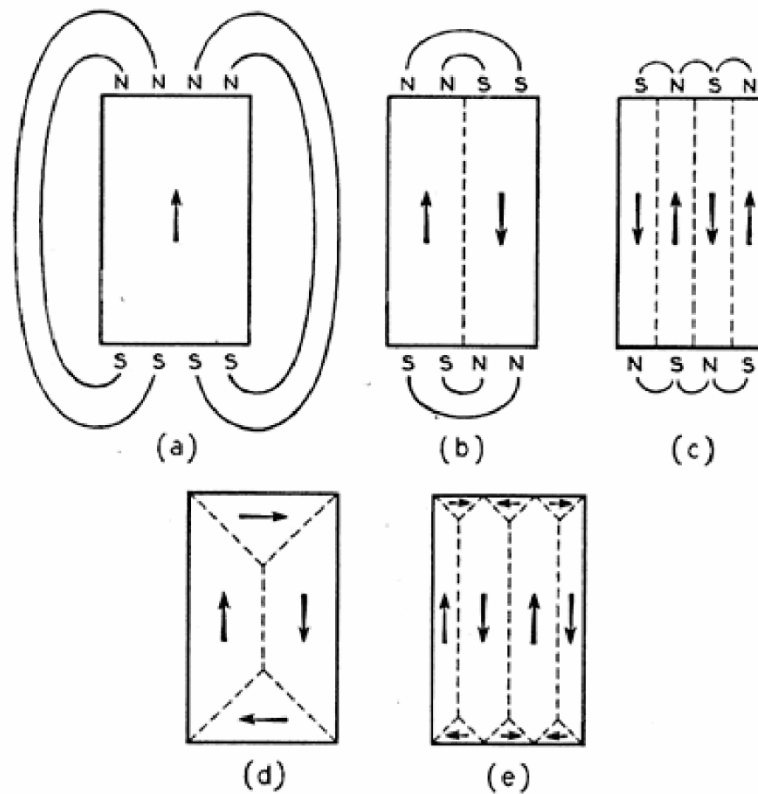
Figure 1.1 The minimization of magnetostatic energy in a magnetic material via formation of domains.[5]

When a magnetic field is applied, the domains having a favorable orientation with respect to the applied magnetic field grow at the expense of the others. At this stage, the magnetization is reversible, i.e. when the field is removed, the material would have zero net magnetization. If, instead, the applied magnetic field is increased further, the domains would continue to grow and they would come across a defect (such as a grain boundary, dislocation etc.) in the crystal eventually. From this point on, the domain wall would be pinned by these defects and become immobile. At some point, the material would possess a single domain structure with the magnetization vector pointing along the easy magnetization axis towards the applied magnetic field, and at even higher fields close to the magnetic saturation, the magnetization of

the material will take place by magnetization rotation. The magnetization processes corresponding to different portion of the hysteresis loops are shown in Figure 1.2.
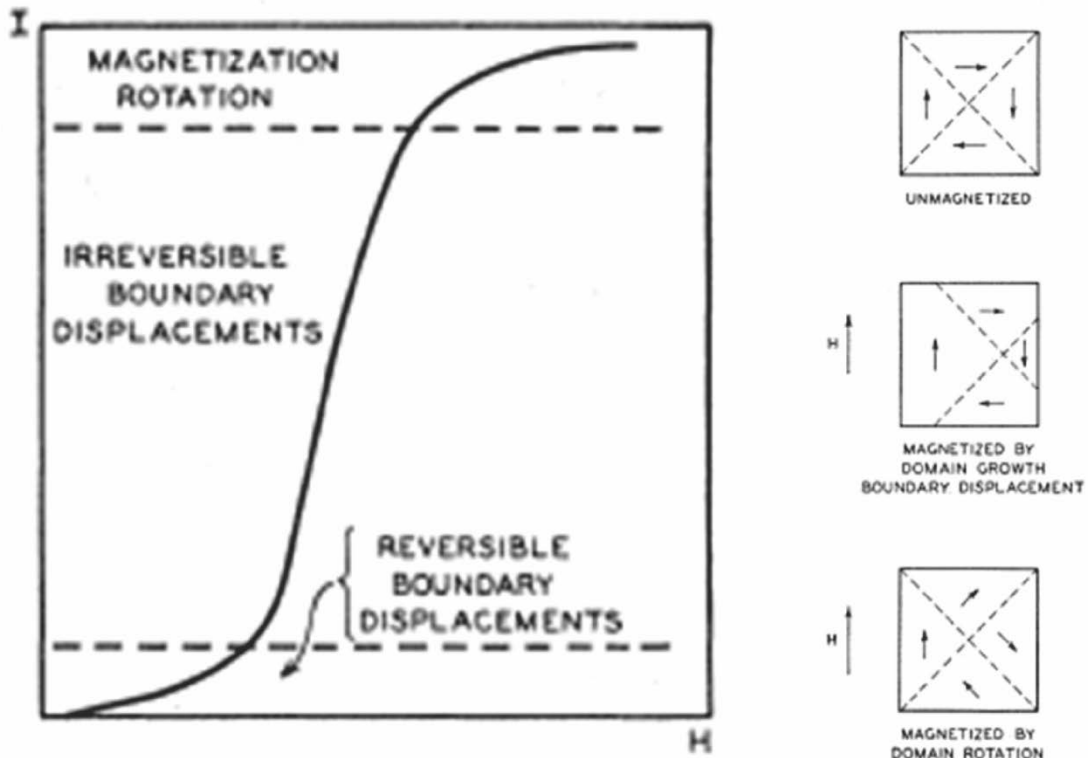
Figure 1.2 Fundamental magnetization processes.[5]

If the magnetic field is removed after saturation, the mobile domains will be reverted in opposite direction to the induced magnetization in the sample, in order to minimize the magnetostatic energy. However, this energy is not large enough to set the immobilized domain walls free from the crystal imperfections; therefore there will a net remnant magnetization (M_r) in the material even in the absence of a field. Additional magnetic fields are required in order to fully demagnetize the material, termed as the coercive field, H_c.

Up to now, elementary processes related to ferromagnetism are explained. This will be followed by brief explanations of various magnetic phenomena in the next sections.

1.1.2. Ferrimagnetism
The magnetization behavior and the type of magnetic ordering encountered in insulators differ from typical ferromagnetic materials. In insulators, two different magnetic sublattices exist, in one the magnetic moments couple to the applied field in the parallel direction, whereas in the other the coupling takes place in the opposite direction, i.e. antiferromagnetically. A net magnetization occurs in such a system because the magnetization in one sublattice overcomes the other one. This behavior is called ferrimagnetism. The technologically most important ferrimagnets are the ferrites, consisting of magnetic metal oxides. $CoFe_2O_4$ and $NiFe_2O_4$ are among the most widely used cubic ferrites.

1.1.3. Magnetic anisotropy
Magnetic anisotropy is the orientational dependence of the magnetic energy as represented in Equation 3:

$$E = K_i V \sin^2\theta \quad (3)$$

Where θ is the angle between magnetization vector and the magnetic field, V is the volume of a magnetic particle and K_i, anisotropy coefficient, is the energy density originating from an anisotropy source "i".[6] There are three main sources of the magnetic anisotropy, being magnetocrystalline, strain-induced and exchange anisotropy. Additionally, there is a so-called shape anisotropy associated with the demagnetized fields from the surfaces and boundaries. All of these anisotropy effects will be explained briefly in the following sub-sections.

Magnetocrystalline anisotropy

In a solid system, the orbital moments originating from the orbital motion of an electron around the nucleus, are strongly coupled to the lattice. Furthermore, the electron spins are coupled to the orbital moments due to spin-orbit coupling. This means, when the spins try to align themselves along the direction of the applied field, the orbital moments would have to reorient themselves too, and this would be strongly affected from the crystallographic directions. The easy magnetization axis is the direction in which the materials can be magnetized with little resistance. Similarly, the crystallographic directions in which the materials resist to the magnetization along magnetic field are termed as the hard magnetization axis. Different crystal structures have different easy axis, as expected, due to different crystal symmetries. For BCC Fe, for instance, the easy axis is <100>, while for FCC Ni this is <111> and for HCP Co it is <1000> direction.[7] In an amorphous material, no magnetocrystalline anisotropy is observed, due to lack of long range order. Similarly, polycrystalline materials also possess very little magnetocrystalline anisotropy, since the anisotropies of individual grains balance themselves out in macroscopic length scales.

Strain-induced anisotropy

Mechanical strains also impose a source of anisotropy, known as strain induced anisotropy. Again, a shape or bond length change in the lattice would affect the reorientation of the orbital moments and cause anisotropy. Strain induced anisotropy is given by:

$$Ks = \frac{-3\sigma\lambda}{2} \quad (4)$$

Where K_s is the strain induced anisotropy constant, σ denotes stress, λ the magnetostriction constant. The easy axis created via strain induced anisotropy can lie perpendicular or parallel to the direction of applied stress, depending on the sign of magnetostriction constant. For negative magnetostrictive materials, tensile stresses would create easy axis in the perpendicular direction whereas for positive magnetostrictive materials, the easy axis would form parallel to the tensile stress.

Exchange anisotropy

Exchange anisotropy occurs at a ferromagnet-antiferromagnet interface as a result of exchange coupling between two magnetic materials. This creates a preferential direction in the form of an unidirectional anisotropy in the ferromagnetic phase.[6]

1.1.4. Magnetostriction

Magnetostriction is a property related to the change in material's dimensions when it is magnetized. The converse magnetostrictive effect also exists, that is when the dimensions of a magnetostrictive material are changed, the material becomes magnetized. Magnetostriction, λ,

is defined as $\Delta L/L$ where L denotes the length of the sample. λ can be measured in longitudinal and transverse directions, depending on the direction of measured strain with respect to the applied magnetic field. Magnetostriction arises also as a result of spin-orbit coupling, and magnetic materials, which have a high atomic number, generally exhibit a high magnetostriction effect.[8] Intuitively, it also takes different values for different crystallographic directions. Moreover it can take positive or negative values, such as Fe, which expands along the direction of magnetization ($\lambda_{Fe}>0$) and Ni, which contracts along the direction of magnetization ($\lambda_{Ni}<0$).

1.1.5. Size effects in magnetic materials – superparamagnetism

Driven by the increased bit density need from the microelectronics industry in order to store more data in a compact volume, magnetic materials are miniaturized. The size effects start to appear, when the size of the smallest dimension of a magnetic material starts to become comparable to magnetic domain sizes. Magnetic domain size is determined as a result of an energy balance between exchange energy and magnetic anisotropy energies due to magnetocrystalline or magnetostrictive effects. For instance, in a material with huge magnetocrystalline anisotropy, the domain wall width would be small, in order to minimize the number of magnetic moments in unfavorable crystallographic directions.[7] However, exchange energy is minimized when the neighboring magnetic moments are as close to parallel as possible and the transition of magnetization vectors within a domain wall is as smooth as possible, which imposes a larger domain size. At sufficiently small grain sizes, the energy decrease by minimization of magnetostatic energy (which is a volume energy) via formation of domains is not enough to compensate the energy gain due to creation of domain boundaries. In this case, single domain grains or particles will form. This means, magnetization in these materials cannot occur through domain wall motion. Instead, coherent rotation of spins is required, which in turn will increase coercivity in comparison to the multi-domain state. In the single domain regime, the coercive field, H_c is inversely proportional to particle size, since the magnetic anisotropy energy, which is associated with particle volume, would decrease as well, as schematically depicted in Figure 1.3 a-b.[6]

a)
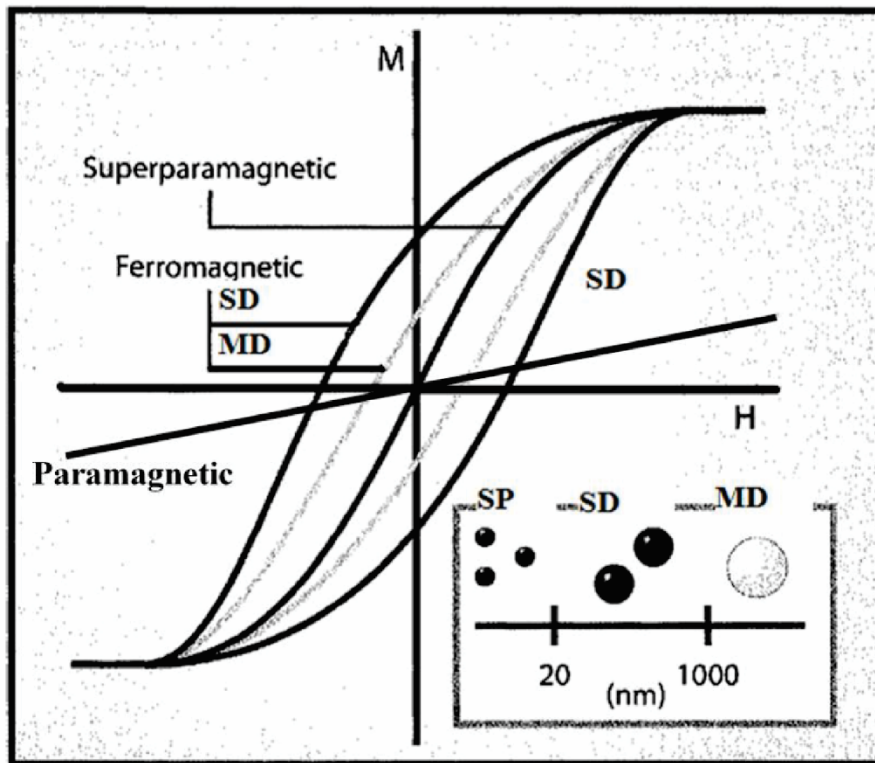
b)
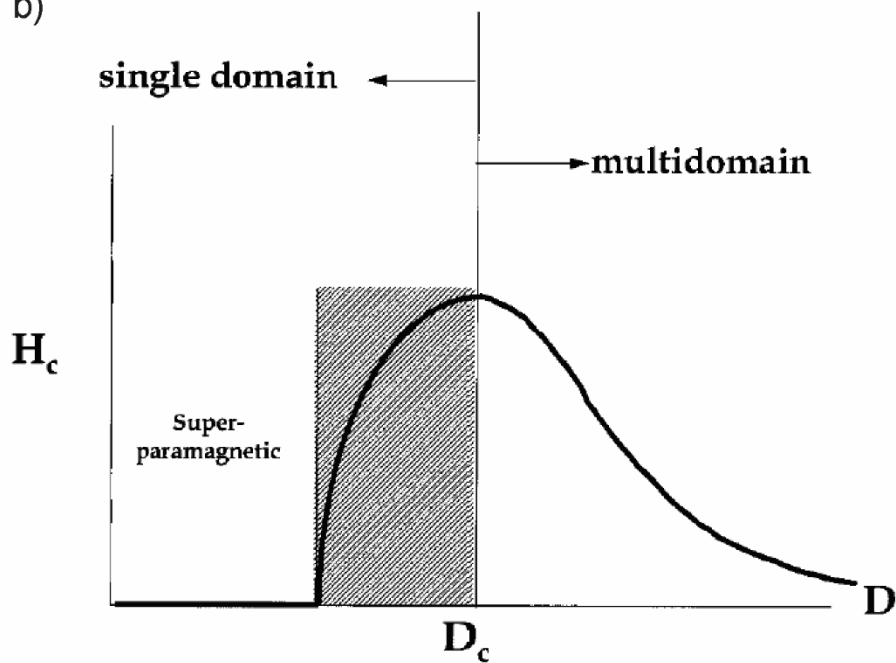
Figure 1.3 a) Hysteresis curves of different magnetic structures revealing the effect of particle size b) dependence of coercive field (H_c) on particle size.[6]

If the particle size gets too small, the thermal energy will overcome the magnetic anisotropy energy and spins will fluctuate randomly at room temperature, causing a phenomenon named "superparamagnetism", as shown schematically in Figure 1.4.

Figure 1.4. Schematic representation of superparamagnetism

In contrast to paramagnetism, superparamagnetic materials respond well to an external magnetic field and have large susceptibilities due to the exchange interactions of magnetic dipoles in superparamagnetic materials. Therefore, the hysteresis curves of superparamagnets are non-linear, whereas these curves are linear for paramagnetic materials. However, as in the case of paramagnets, there is no net magnetization remaining when the magnetic field is removed. Superparamagnetic materials possess a characteristic feature called "blocking temperature", T_B, below which the thermal energy is not sufficient to randomize the magnetization and the material can be magnetized permanently. Roughly T_B can be calculated from equation (5):

$$K_{eff}V = 25k_BT_B \quad (5)$$

Where K_{eff} is the effective magnetic anisotropy coefficient, k_B is the Boltzmann constant and V volume of the particle. Experimentally, they are derived from measurements of zero field cooling (ZFC) and field cooling curves (FC). The material is cooled to 5-10 K in the absence of magnetic field. Then the induced magnetization in the sample is measured under constant applied field, while the temperatures are measured gradually in order to obtain ZFC curves. The magnetization starts to increase with increasing temperatures, since with increasing thermal energy more "frozen" spins are activated, and they can reorient themselves with respect to the applied field. However, if the thermal energy becomes too large so that the magnetic anisotropy energy of a particle is exceeded, the spins will be fluctuated and the induced magnetization will drop. The temperature, at which the induced magnetization in the sample reaches maximum, would then correspond to T_B. In the case of FC curves, the material is continuously cooled under a constant external magnetic field, while the induced magnetization is being recorded. For a typically superparamagnetic material, the magnetization will increase monotonously in the FC curve, due to less and less spins being thermally randomized with decreasing temperatures. Ideally, ZFC and FC curves should be the same until T_B and first separate when the temperature is lower than T_B.

As it can be inferred from the above explanations, superparamagnetism imposes a size limit for magnetic memory applications because of the vanishing coercivity and remnant magnetization as a result of thermal effects. Since there is no net magnetization remaining when the magnetic field is removed, recording of any data is not possible.[9] One possible way to scale down the magnetic materials for increased bit densities is to tune the magnetic anisotropy energy of a particle, so that energy barrier required for spins to fluctuate becomes larger than thermal energy, E, at room temperature, which is in the order of $E \sim k_BT_R$, where T_R is room temperature. This can be achieved via inducing certain texture (for magnetocrystalline anisotropy) or shape (shape anisotropy), as well as strains.[9]

1.1.6. CoFe₂O₄

$CoFe_2O_4$ is a commonly used ferrimagnetic material owing to its attractive magnetic properties combined with its electrically insulating nature. It has an inverted spinel structure with face centered cubic symmetry, where Co^{2+} ions sit on the octahedral sites whereas Fe^{3+} ions are distributed into octahedral and tetrahedral sites. As a ferrimagnet, it has two magnetic sublattices corresponding to octahedral and tetrahedral sites. The Fe^{3+} ions at the tetrahedral sites are coupled to the Fe^{3+} ions at the octahedral sites antiferromagnetically, which cancels out all magnetization from Fe^{3+} ions. Instead, all the induced magnetization in this material originates from the spin reorientation of Co^{2+} at the octahedral sites. The presence of Co^{2+} donates this material high magnetocrsytalline anisotropy and high magnetostriction, due to strong spin-orbit coupling interactions. For single crystalline $CoFe_2O_4$, max. magnetostriction of $540X10^{-6}$ has been measured along <100> direction.[10] Polycrystalline $CoFe_2O_4$ is reported to exhibit a magnetostrictive strain of approximately $170X10^{-6}$.[11] As a comparison, polycrystalline Fe_3O_4 exhibits a strain at magnetic saturation of around $60*10^{-6}$ whereas this value reaches to $5500*10^{-6}$ for $Tb_{0.5}Zn_{0.5}$ alloy.[12]

1.2. Ferroelectric phenomenon & materials

Ferroelectric materials are insulating systems with spontaneous electrical polarization at zero electrical field. Electrical polarization is defined as the density of dipole moments per unit volume.[13] The spontaneous polarization in ferroelectric materials can arise from permanent dipoles in the lattice due to displacement and off-centering of ions or due to order-disorder mechanisms. Especially in displacive ferroelectrics, the change in polarization states highly involves strain, since the polarization changes occur due to movement of ions in the lattice. Similar to ferromagnets, this spontaneous polarization can be switched using electrical fields, and likewise the polarization vs. applied electric field curves also follow a hysteresis behavior. Ferroelectric materials too, loose their spontaneous electrical polarization above T_c. Below T_c, ferroelectric materials are in a polar state and composed of a multi-domain structure, where each domain is a region of uniform electrical polarization vector. The direction of electric polarization changes abruptly from one ferroelectric domain to the other; therefore the domain wall widths are much smaller as compared to the magnetic domain walls. A process called 'poling' is applied to align these ferroelectric domains in parallel direction to the applied DC electrical field and brings the material ideally into a single domain state. For poling, the applied electrical fields should be larger than the coercive voltage so that the ferroelectric switching can take place in the domains which have an unfavorable orientation with respect to the applied electrical field. An important point to be considered is that the applied voltages do not exceed the dielectric breakdown strength of the material, which is in the range of few V for most of the thin films. After the voltage is removed, a fraction of polarization can recover. However in most cases there is enough remnant polarization (P_r) after poling. This process is particularly useful in terms of maximizing the strain response of a ferroelectric material in the application direction of electric fields, owing to the pre-aligned ferroelectric domain structure. It is at this point useful to describe parameters determining the interaction between strains and electrical fields.

1.2.1. Piezoelectricity

Piezoelectricity is the generation of electrical polarization upon application of strains. The converse effect, occurrence of strain, i.e. change in sample dimensions when an electric field is applied, is termed as electrostriction. One of the relevant parameters is defined as the longitudinal piezoelectric coefficient, d_{33}, which has units in terms of either pC/N or pm/V, depending on either the direct or converse piezoelectric effect is being measured. Typical piezoelectric coefficients range from 2.3 pm/V for quartz, which is a non-ferroelectric

piezoelectric, to 10-20 pm/V for $LiNbO_3$ and 100 pm/V for lead zirconium titanate,[14] and range between 5-50 pm/V for $BaTiO_3$.[15]

1.2.2. Ferroelectric hysteresis

An important outcome of domain switching is the occurrence of ferroelectric hysteresis. At small electric fields, the ferroelectric domains of favorable orientations align themselves and the polarization increases linearly with increasing electric field. When the magnitude of the electric field is increased further, the domains with unfavorable orientations will also re-orient themselves in directions that are crystallographically as close as possible to the direction of electric field. As the domain switching reaches completion, the electrical polarizations become saturated (termed as saturation polarization, P_s), and do not change upon further increase of electric field amplitude. Upon reversing the electrical field, polarization reversal takes place by heterogeneous nucleation of newly formed domains (usually at the electrodes) or by growth of existing domains. The domains can grow either along the polar direction, or in lateral directions.[16] As the field is reduced to zero, not all the domains are switched and a measurable macroscopic polarization persists to exist, termed as remnant polarization (P_r). In order to achieve full polarization reversal, the electric field should be further increased in the reverse direction. The value of the electric field, where half of the electric polarization is switched, is defined as coercive voltage (E_c). An ideal hysteresis curve would be symmetrical, with equal P_r, P_s and E_c. However, mechanical constraints, presence of charged defects, or thermal treatments can affect the shape of the hysteresis curve as well as the magnitude of the hysteresis features. An example hysteresis curve with important features is depicted in Figure 1.5.
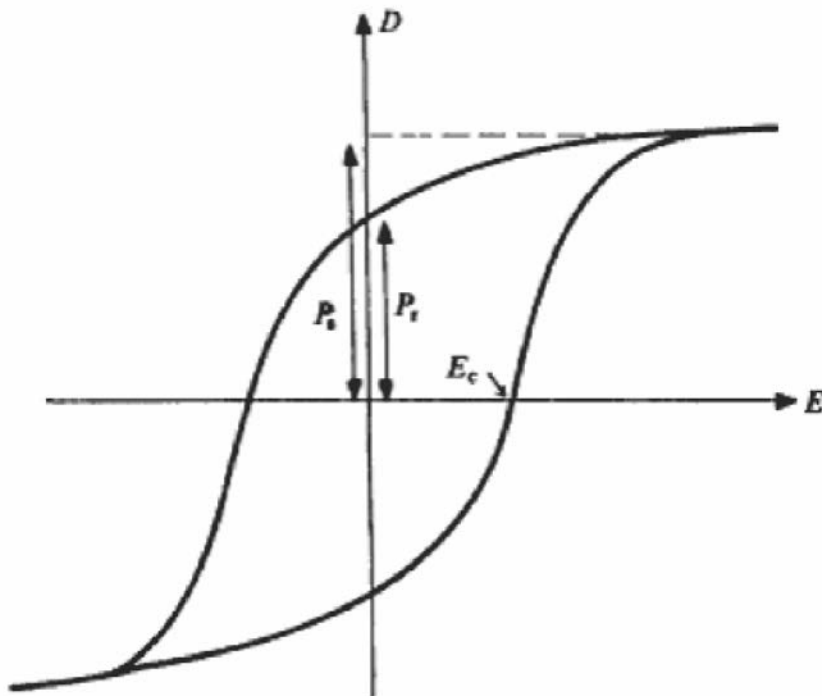

Figure 1.5 Ferroelectric hysteresis loop displaying E_c, P_r and P_s.[16]

 In order to measure the electrical polarization and hysteresis characteristics, a full ferroelectric device is fabricated with top and bottom electrodes electric contacts. Then, the sample is connected in series to a reference capacitor with very large capacitance and a small AC voltage is applied. Ideally, only displacive currents should flow in the circuit and the ac potential across the ferroelectric vs the potential across the capacitor curves are drawn. From the

potential across the reference capacitor, the displacive charges flowing in the circuit can be calculated and this should be equal to the charges flowing through the ferroelectric, since they are connected in series.

1.2.3. BaTiO$_3$

BaTiO$_3$ is a lead free displacive type ferroelectric material with perovskite crystal structure. Ba^{2+} ions occupy cube corners, Ti^{4+} ions sit at the cube center, surrounded by O^{2-} octahedron. At room temperature, BaTiO$_3$ adopts a tetragonal crystal structure, in which Ti^{4+} ions are at a slightly off-centered position. Owing to the non-centrosymmetric structure of the tetragonal phase, a net dipole moment and spontaneous polarization exist due to the relative displacement of the Ti^{4+} ions with respect to the oxygen octahedron. Above T$_c$, BaTiO$_3$ undergoes a phase transformation and adopts a cubic crystal structure, which in turn do not possess permanent dipoles and therefore is paraelectric. The cubic and tetragonal crystal structures are presented in a comparative manner in Figure 1.6. BaTiO$_3$ undergoes two more phase transitions, from tetragonal to orthorhombic at 278 K and from orthorhombic to rhombohedral at 183 K. All these 3 phases are ferroelectric with <100>, <110> and <111> as polar axes, respectively, which correspond to the atomic displacements in reference to their cubic positions.
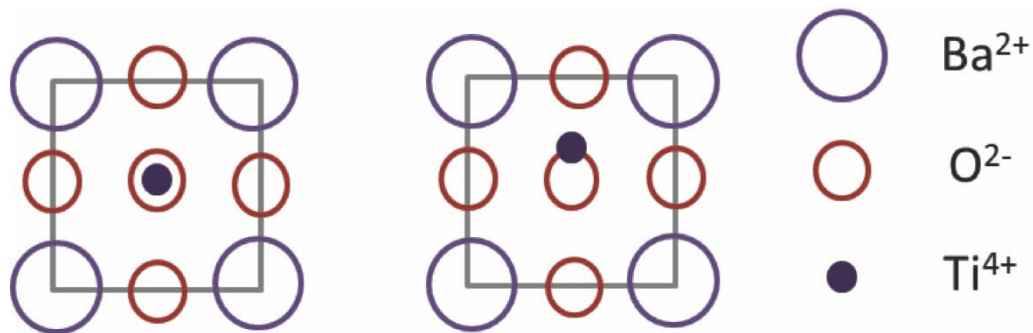
Figure 1.6 Side views of cubic (left) and tetragonal (right) crystal structures of BaTiO$_3$.

1.2.4. Size effects in ferroelectrics

Perception of size effects on the ferroelectric properties is somewhat less straightforward as compared to the size effects in magnetic materials. Firstly, a certain number of dipoles is required for the long range stabilization of electrical polarizations. In this sense, if the material dimensions along the polar axis become smaller, the ferroelectric phase may be destabilized due to insufficient number of dipoles for long range interactions. However, theoretical treatments to predict the minimum dimension, at which long range stabilization vanishes, are far from matching the experimental findings. In fact, many effects contribute to the size limits observed in ferroelectrics. For instance, sample stoichiometry, grain boundaries, dead layers etc. may destabilize the ferroelectric phase in thin films of 100 nm thickness. For BaTiO$_3$, the tetragonality measured in terms of c/a scales down with size as well, with a parallel decrease in polarization. In contrast to polarization, the coercive electrical field, E$_c$, increases significantly upon film thickness reduction, which is expressed empirically as $E_c \sim t^{-2/3}$. This effect has been attributed to the surface pinning of domain walls, the effect of depolarization fields on the nucleation of ferroelectric domains and the presence of a non-ferroelectric layer at the ferroelectric- electrode interface.[17]
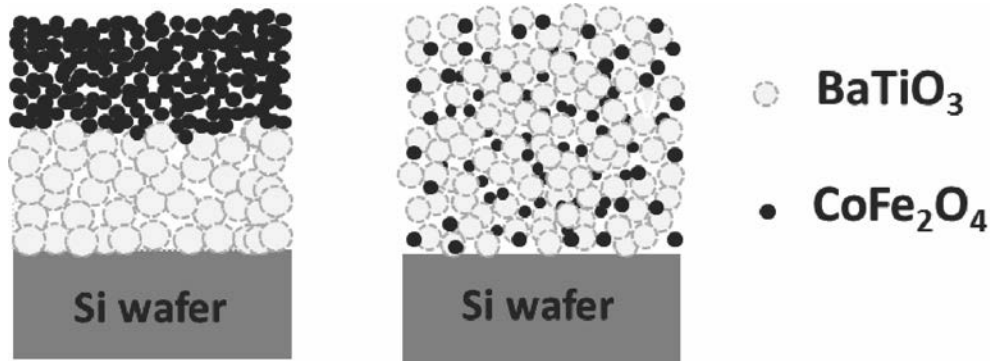
1.3. Magnetoelectric coupling

Materials which possess more than one ferroic order (ferroelectricity, ferromagnetism or ferroelasticity) are called multiferroic materials. Particularly interesting multiferroic materials are the ones with the dual presence of ferroelectric and ferromagnetic order, which exhibit

magnetoelectric coupling. These materials have attracted wide attention in recent years not only due to the interesting and broad physics underlying the coupling mechanisms, but also because of their application potential to novel devices, which enable low power consumption, fast response dynamics, miniaturized device architecture and heterogeneous read/write operations for memory elements.[18] Single phase multiferroic materials are rare and offer limited magnetoelectric coupling under ambient conditions. The reason for their scarcity can be briefly explained in a simple system as follows: A ferroelectric perovskite requires an A-site cation with empty d-shells to promote hybridization between O and A-site cations upon polarization. However, ferromagnetism requires half-filled d orbitals for the spins to align themselves with respect to the magnetic field. Due to this fact, single phase multiferroics are limited to few systems, such as $BiFeO_3$, hexagonal manganites etc.[19] In this sense, artificial multiferroic heterostructures are advantageous since they offer respectable room temperature magnetoelectric coupling. There are three main magnetoelectric coupling mechanisms in these systems, namely exchange, charge mediated and strain mediated magnetoelectric coupling. Exchange coupled multiferroics involve antiferromagnets, and therefore are out of scope of this thesis. Charge mediated coupling is briefly the accumulation of spin polarized electrons at the positive side of a dielectric and their depletion at the negative side. This way, a net magnetization is induced at the ferromagnetic electrode- insulator junction upon application of an electric field and is an interface effect.[20] However, volatility and large energy consumption (due to high voltages applied) issues are linked to these kind of artificial multiferroic heterostructures.[21] In this sense, the strain mediated magnetoelectric coupling mechanism is more promising and was investigated in the framework of this thesis.

1.3.1. Strain mediated magnetoelectric coupling

This type of magnetoelectric coupling is found in artificial multiferroic heterostructures which rely on composites of piezoelectric- and magnetostrictive constituents. In case of an electric field, the piezoelectric material undergoes strain due to converse piezoelectric effect. This strain can be transferred to the magnetostrictive state at the piezoelectric-magnetostrictive interface, and the stress causes a change in the magnetic phase due to magnetostriction. For enhanced magnetoelectric coupling, it is obvious that constituents with high piezoelectric and magnetostrictive coefficients are required, as well as a large interfacial area to facilitate the strain transfer. Moreover, high insulating properties are desired for the magnetostrictive phase for an efficient electrical polarization in the ferroelectric phase upon application of electrical fields. For these reasons, $CoFe_2O_4$ has been chosen as the ferrimagnetic component, due its high magnetostriction and electrically insulating nature and $BaTiO_3$ as the ferroelectric constituent due to its high piezoelectric coefficient and lead-free chemistry. In this work, $CoFe_2O_4$ and $BaTiO_3$ have been mixed in two composite geometries, namely as alternating lamina of $CoFe_2O_4$ and $BaTiO_3$ stacked on top of each other for the multilayered connectivity or dispersion of $CoFe_2O_4$ nanoparticles into $BaTiO_3$ matrix, i.e. co-dispersed connectivity, which are represented schematically in Figure 1.7.

Magnetoelectric coupling can be reported in terms of magnetic field effects on electric order of the material, termed as direct magnetoelectric coupling, or vice versa, namely the converse magnetoelectric effect. Investigation and quantification of the latter effect is rather difficult because of the non-linearity in magnetic order originating from closure domains.[22] However, the electric (or voltage) control of magnetism bears more technological importance, since it enables miniaturization in magnetic systems and opens up possibilities for more efficient memory applications. In the next section, brief literature review will be presented on direct and converse magnetoelectric coupling effect in strain mediated magnetoelectric composites with a focus on the latter.

Figure 1.7 Multilayered and co-dispersed magnetoelectric composite geometries

1.3.2. Literature examples on magnetoelectric coupling effect in strain-mediated multiferroic thin film composites

One of the early works in the field investigates direct magnetoelectric coupling effect in a $BaTiO_3$-$CoFe_2O_4$ nanocomposite thin film system, which consists of $CoFe_2O_4$ nanopillars distributed in $BaTiO_3$ matrix. The direct magnetoelectric coupling is observed as an asymmetry in the local charge distribution of Ti^{4+} ions, which is measured to be different along transverse and film thickness directions in case of an applied in-plane magnetization. The measured effect is interpreted as formation of in-plane electrical polarization which is induced by out-of-plane magnetization in the $CoFe_2O_4$ phase.[23]

The converse magnetoelectric coupling in thin film composites is often reported based on the indirect changes in the amplitude as well as in the orientation of magnetization through modification of magnetic anisotropy with the help of electric induced strains.[24, 25] Direct electric induced switching in the magnetization of $CoFe_2O_4$ in $BiFeO_3$-$CoFe_2O_4$ system is demonstrated via x-ray magnetic circular dichroism and magnetic force microscopy measurements.[26] The measurements show re-orientation of magnetic easy axes via strain.[26] Moreover, the voltage controlled magnetization switching is directional in the presence of an applied magnetic field: the electrically-induced magnetization switching was greater in the oppositely magnetized regions of the sample in comparison the regions of parallel magnetization with respect to the applied magnetic field due to dominating Zeeman energy (MHcosθ).[27]

Another work, which involves a $CoFe_2O_4$ layer on $BaTiO_3$ substrate, reports direct correlations of changes in the magnetic anisotropy in the $CoFe_2O_4$ layer to the strain modulations in $BaTiO_3$ substrate.[28] A different approach harvests converse magnetoelectric effect to manipulate magnetic anisotropy in multiferroic composites for non-volatile voltage control of superparamagnetism [29] or to decrease the magnetic write-fields for magnetic memory applications.[25] Further demonstrations of this approach are carried out in Ni-PMN PT[30] and Co-PMN PT[31] systems as an electrically induced magnetic easy axis rotation, where non-volatile 90° magnetization reversal takes place due to strain mediated coupling between ferroelectric substrate and the Ni and Co nanoislands. Moreoever, the magnetization reversal is shown to reach 180° in case of an applied magnetic field following voltage pulses.[31]

1.4. Magneto-optical effects

Magneto-optics deal with the interaction of electromagnetic radiation with magnetically polarized matter. When light encounters a magnetic medium, its plane of polarization will be rotated. This effect is termed as Kerr effect for the reflection, and Faraday effect for transmission. The Kerr rotation is twice as large as the Faraday rotation. This effect is already utilized in many applications, such as imaging of magnetic domains, spectroscopy, magneto-optical waveguides and magneto-optical data recording. To understand the origin of magneto-

optical effects, plane polarized light should be decomposed into its right and left circularly polarized components. The orbital momentum of the photons in the circularly polarized light is equal but of opposite sign for different circular polarizations. Due to spin-orbit coupling, magnetization causes atomic levels to split into two sub levels corresponding to spin-up and spin-down, termed as Zeeman splitting. When a photon interacts with an electron, both energy and orbital momentum should be conserved. Therefore, only specific transitions are allowed as shown in Figure 1.8, each transition corresponding to one circular polarization.[32]
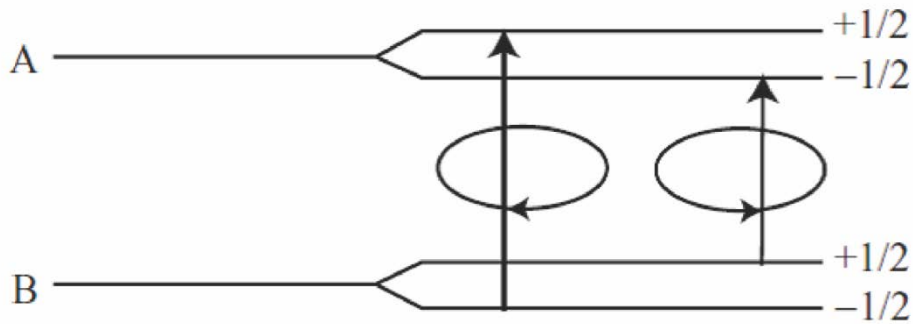
Figure 1.8 Zeeman splitting and transitions corresponding to circular polarizations of the light.[32]

In addition, the lower energy level in the ground state contains statistically more electrons then the higher energy level, which means the left circularly polarized light will be absorbed more than the right circularly polarized light, known as circular dichroism. This in turn imposes a rotation in the polarization plane of the light, when the circularly polarized components are recombined into a plane polarized light.

1.5. Selected methods & instrumentation

In this section, selected characterization methods and the underlying physical principles, which are used throughout the thesis, will be explained.

1.5.1. Synchrotron techniques for magnetic characterization

Synchrotron radiation turned out to be extremely useful technique for characterization of magnetic materials, due to its element and orbital selectivity, magnetic sensitivity, possibility to calculate spin and orbital moments separately with the aid of sum rules, defined nature of core level excitations and high energy sensitivity.[33] Soft X-rays are more sensitive to the magnetic nature of the sample, therefore the measurements are performed usually in the 0.5-1.6 keV range.[33] For the elemental edges (Fe, Co and Ti) measured in this work, it covered the L edge corresponding to 2p→3d transitions. The measurement technique relies on the dichroic absorption of soft X-rays in a magnetized medium. The effect is termed as X-ray magnetic circular dichroism (XMCD) and is obtained via subtraction of X-ray absorption spectra (XAS) intensities taken using right and left circularly polarized light (Γ^+-Γ^-).[34] 2p core level orbitals are split into two states under an external magnetic field termed as $2p_{3/2}$ and $2p_{1/2}$, due to Zeeman splitting. According to selection rules, circularly polarized light creates spin polarized electrons, because of the angular momentum transfer and spin-orbit coupling. Upon incidence of right circularly polarized light onto magnetized material, the majority of excited electrons from $2p_{3/2}$ carry a spin of m_s=+1/2, while the majority of excited electrons from $2p_{1/2}$ carry a spin of m_s=-1/2. In the case of a left circularly polarized light, the sign of the electron spin polarizations will be reversed. Now, the unoccupied states in the 3d

conduction band should be considered. If H>0, all energy states for spin-down (m_s=-1/2) will be occupied (at T= 0 K) and the 3d spin-up states will be available. Since light do not interact directly with the spin of the electrons, there will be a large transition possibility for spin-up polarized $2p_{3/2}$ electrons created by right circularly polarized X-rays. However, left circularly polarized light creates a majority of spin-down polarized electrons at the $2p_{3/2}$ level, and the spin-down states at the 3d valence band are full. This means that the probability of this transition is low. Therefore, the right circularly polarized light will be absorbed more than the left circularly polarized light, creating X-ray magnetic circular dichroism effect. At the $p_{1/2}$ level, the XMCD signal would have the reverse sign, due to the oppositely spin-polarized nature of excited electrons. The effect is summarized in Figure 1.9.[35]
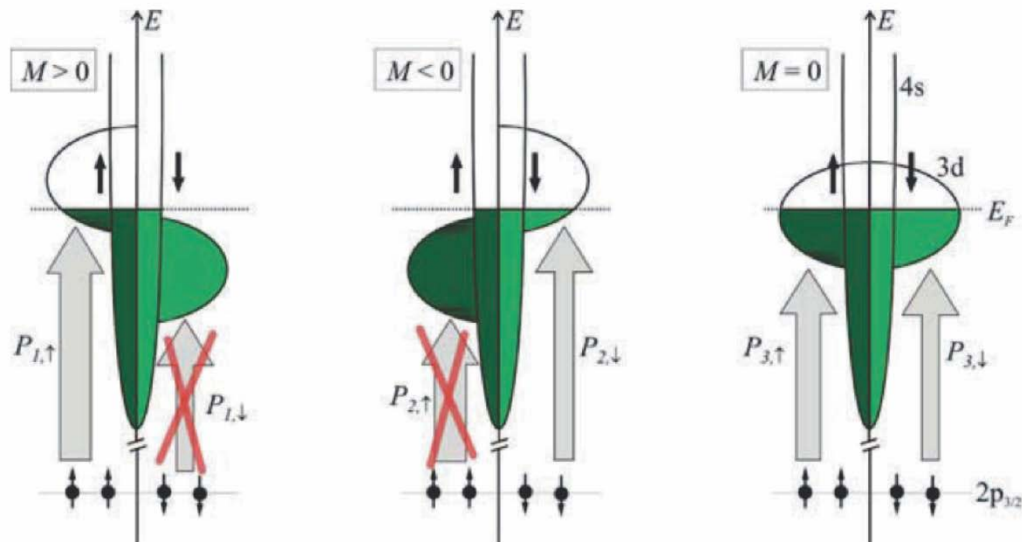
Figure 1.9 The electronic transitions from $2p_{3/2}$ level into 3d conduction band[35]

1.5.2. Magneto-optical Kerr microscopy

Magneto-optical Kerr microscopes exploit the changes in the reflected light upon an encounter with magnetic medium as discussed in the magneto-optical effects part (Chapter 1.4), either as a change in intensity or as a rotation in the plane of polarization. The microscope can operate in longitudinal, polar or transverse geometry, depending on the angle between the propagation vector of the light and the sample magnetization, shown schematically in Figure 1.10 a-c.
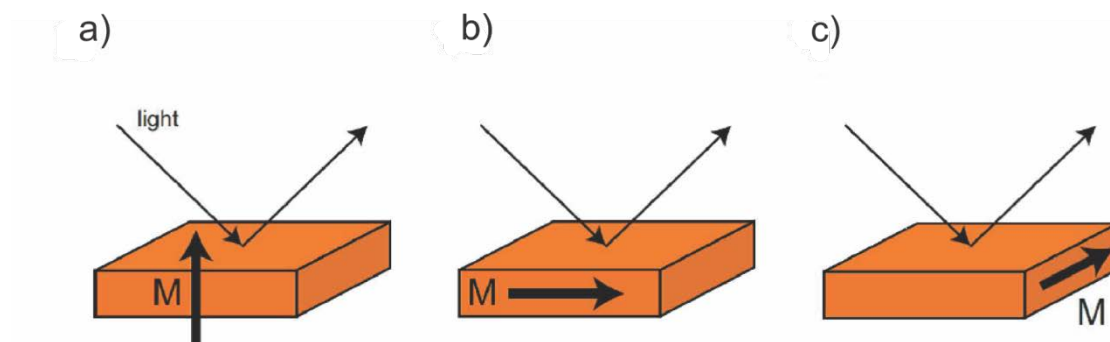

Figure 1.10 a) Polar, b) longitudinal and c) transverse Kerr effect measurement geometries[36]

For the longitudinal configuration, polarizer-analyzer combination is used. When the angle between the polarizer and analyzer is 90°, an intensity minimum should be measured. Nevertheless, the Kerr effect will cause a rotation in the reflected light, which would have component lying in the favorable direction to the analyzer, resulting in some intensity. The amount of rotation, therefore the intensity falling onto the detector, is proportional to the magnetization. This technique can be used to image magnetic domains as well as to carry out magneto-optical hysteresis measurements on a pre-selected area of the sample.

1.5.3. Piezoresponse force microscopy

Piezoresponse force microscopy (PFM) relies on the converse piezoelectric effect to image the ferroelectric domains or to study the ferroelectric switching characteristics on the nanoscale. Briefly, a pre-set small AC voltage in the 10-100 kHz range is applied to a conductive PFM tip, and the thickness changes or surface deformations due to the converse piezoelectric effect are tracked with the help of a photodiode coupled to the PFM cantilever. PFM can be operated in different ways: If the torsions created on the cantilever are recorded, that is when the applied electrical field is perpendicular to the ferroelectric domains, it is the lateral PFM operation mode, and if the cantilever deflections and buckling are tracked, as a result of parallel or anti-parallel orientation of electrical field to the ferroelectric domains, then it is vertical operation mode.[37] The basic mechanism underlying cantilever deflections in vertical PFM is as follows: A conductive PFM tip is brought into contact with the sample surface. If the bias applied on the tip is parallel to the direction of the vertical polarization in the ferroelectric domain, the sample surface will expand and cause an upward bending in the PFM tip, detected as a positive deflection in the photodiode. If the bias is antiparallel to the vertical polarizations, the sample surface will contract and will cause a negative deflection in the photodiode,[38] as depicted in Figure 1.11.
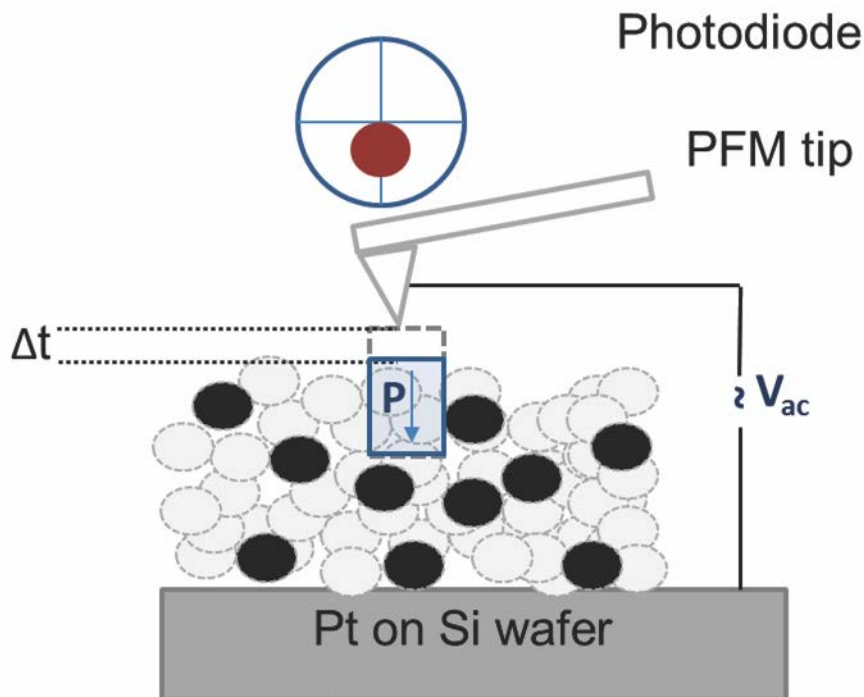
Figure 1.11 Schematic operation of vertical PFM

The governing equation relating the applied electrical field and the surface deformations is given below:[38]

$$\Delta t = d_{33} V + \frac{M333}{t} V^2 \qquad (6)$$

Δt is the vertical surface displacement, t is sample thickness, V is applied voltage ($V=V_{ac}+V_{dc}$), d_{33} is the longitudinal piezoelectric coefficient and M_{333} is the electromechanical coupling coefficient. M_{333} is independent of domain polarization and gives an inherent background signal. Therefore, the PFM measurements in this work are carried out in remnant mode ($V_{dc}=0$) in order to minimize this effect.

As mentioned before, the standard ferroelectric characterization technique involves fabrication of a device including electrodes and contacting wires. In this sense, characterization of ferroelectrics through measurement of piezoelectric characteristics via PFM is advantageous and serves as a readily available and fast characterization method, because AFM tip serves a top contact and top electrode, so that fabrication of top electrodes and contacting wires can be avoided. Next, the principle of local piezoelectric hysteresis measurements using PFM will be explained briefly.

1.5.4. Measurement of local piezoelectric hysteresis loops

Switching spectroscopy PFM technique is adopted to measure the local piezoelectric hysteresis loops. The PFM tip is held at a fixed position, while an additional V_{dc} is applied in incremental steps between $\pm V_{max}$. Between the dc voltage pulses, the d_{33} is read in remnant mode. Here, V_{dc} should be large enough to saturate the hysteresis, but should not exceed the dielectric breakdown voltage of the sample. The read voltage, V_{ac}, should be kept under the coercive voltage of the sample in order to avoid back-switching of the PFM signal created by DC voltage pulses. The evolution of the PFM signal with varying voltage is based on the dependence of d_{33} on dielectric permittivity and polarization. At first, a ferroelectric domain is nucleated under the PFM tip, and polarization, dielectric permittivity and d_{33} continues to increase as the forward and lateral growth of the domain take place.[39] Hence, d_{33} vs voltage curves provide a deep insight into the ferroelectric switching characteristics of the sample.

The brief explanation and introduction of the physical effects and characterization techniques is concluded here and some insights related to the synthesis of thin films and nanoparticles will be provided in the next sections.

1.6. Deposition techniques

There are two main classes of thin film deposition techniques, being vacuum based deposition techniques; including evaporation, magnetron sputtering, pulsed laser deposition, molecular beam epitaxy, chemical vapor deposition, and wet chemistry based liquid phase deposition techniques, namely dip coating, spin coating and spray coating. Choice of deposition technique depends on many factors, such as required film thickness, deposition rates, stoichiometric control, growth mode (i.e. epitaxy), processing times and temperatures. Liquid phase deposition approaches are preferred to the vacuum based thin film deposition techniques because of their advantages such as moderate processing temperatures, easy stoichiometry control, no need for sintered targets, low costs and possibility to scale up. With the incorporation of nanoparticles into liquid phase thin film deposition technique, other advantages would also come into play, for instance monodispersed and nanosized nature of building blocks, which facilitate homogenous mixing and enhanced interfacial areas for the synthesis of novel composite architectures. However, difficulties in achieving epitaxy and residual porosity even after sintering remain to be the main challenges related to this process.

In this work, a nanoparticle based liquid phase deposition method is adopted, in order to benefit from monodispersed and predefined building blocks for final sintered films. This enables full control over size, phase and the functionalities in the final sintered thin films, which is crucial in terms of targeted properties and potential device implementation of these materials.

In the following sections, common liquid phase thin film deposition techniques will be introduced, namely dip coating, spin coating and spray coating.

1.6.1. Dip coating

The dip coating process involves the upward withdrawal of a substrate at constant rate from a solution containing either the precursors or the nanoparticles of the desired phase. The dip coating process can be viewed as three stages: At first stage, the substrate is contained in the solution phase long enough to allow for complete wetting of the substrate. During the deposition and drainage stage, a thin layer of precursor is drawn along the pulling direction, thereby allowing for the film deposition. Excess liquid will drain from the surface. Finally, the volatile liquid evaporates, which causes concentration of the inorganic species and aggregation, followed by gelation and formation of a dry gel layer.[40] Pulling speed (U), viscosity(η), density (ρ), and liquid-vapor surface tension (γ_{LV}) influence the film thickness. For moderate pulling rates, it can be expressed as:[40]

$$t = \frac{(\eta U)2/3}{\gamma_{LV}1/6(\rho g)1/2} \quad (7)$$

The main drawbacks of the process are the non-uniformity in film thickness (termed as wedge effect), development of fatty edges due to solvent drainage and partial removal of the film due to solvent vapor refluxing.

1.6.2. Spin coating

Spin coating is a very popular and widespread coating technique, since it is a rapid deposition method to produce thin films of high quality and uniformity on planar substrates.[41] It consists of three main stages: dispense of the coating solution and substrate wetting, fluid flow dominated thinning and evaporation of the solvent.[41] Using a pipette or syringe, the coating solution is dispensed onto substrates, spinning of the substrate at a low speed (typically around 200 rpm) at this stage aids the spreading of the coating solution, termed as dynamic dispensing. Subsequently, the substrate is accelerated to moderate spinning speeds (between 500-1000 rpm), in order to spin-off the excess solvent and improve the film uniformity. At the end, final spinning speeds of typically a couple of thousands rpm are reached to evaporate the solvent. The thin film thickness is controlled by spinning speed, solvent concentration and viscosity. Common practice is to carry out few experiments and find out dependence of thickness on concentration and spinning speed. Certainly, environmental conditions such as relative humidity and ambient temperature are also crucial parameters. Therefore, the experimental conditions are kept constant by conducting the spin coating process in a controlled environment, such as a glovebox. In this work, the deposition of nanoparticle thin films is carried out in a synthetic air filled laminar flow controlled glovebox, which is equipped with a dip and spin coater, plasma cleaner, hot plane and an oven, as shown in Figure 1.12. Owing to the minimized dust and particle contamination in the glovebox, thin films of high quality and uniformity are deposited.

In addition to the aforementioned factors, acceleration rates and duration time at the final stage are among the key parameters in terms of controlling thin film uniformity and thickness. In this respect, volatility of the solvent plays also a key role while determining spin coating parameters; generally solvents of moderate evaporation rates are desired for thin films of high quality.[42] In the following sub-sections, these factors affecting film quality and spin coating defects will be explained in further detail.
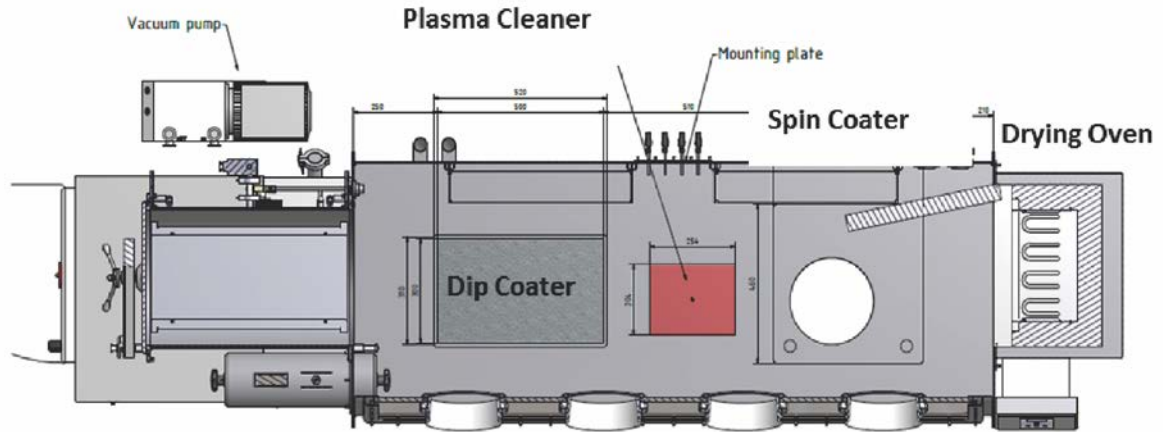
Figure 1.12 Top view of the synthetic air laminar flow controlled glovebox

Striations

Striations are the radial thickness modulations caused mainly by the uneven capillary forces and surface tension gradients during the evaporation of highly volatile coating solvents. Regions of higher surface tension drive fluid away from regions of lower surface tension, generating thickness undulations, as depicted schematically in Figure 1.13[43] They are characterized macroscopically by a granular region at the substrate center, whereas towards the edges these features become elongated. By avoiding high acceleration rates and spinning speeds, striations can be circumvented.
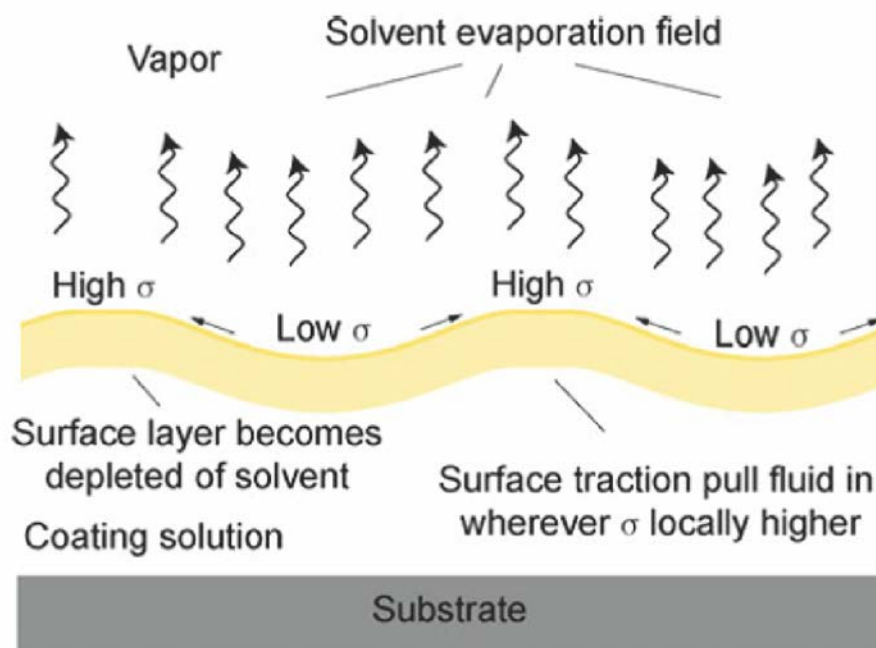
Figure 1.13 Evolution of surface tension gradients and consequent thickness undulations[43]

Comets

Comets are the streak patterns pointing radially outwards and caused by the defects which are stuck onto the substrate surface and obstruct of the flow around them. In order to get rid of

19

comets, spin coating solutions and the ambient should be kept particle and dust-free, which can be achieved by filtering the solutions, filling the spin coater bowl with filtered air or containing the whole spin coating equipment under laminar flow controlled fume hoods or gloveboxes.

Chuck marks

Thickness variations occurring at physical contact locations to vacuum fixture are called chuck marks. Thermal effects are believed to be the root cause of this phenomenon. Evaporative cooling takes place during spin coating. At the contact locations to the vacuum fixture, these cooling effects are better compensated and faster evaporation of the solvent takes place. This results in thicker coatings on the areas corresponding to the vacuum fixture. As expected, thermally insulating substrates are more prone to developing such defects.

Gradual radial thickness variations

Non-Newtonian changes in the solvent viscosity during spin coating can lead to formation of either convex or concave radial variations in thin film thickness.[43] For instance, thickness at the edges will decrease for shear thinning fluids, since the flow rate increases at larger radius. Another common related defect is the generation of edge-beads, originating from difficulties in detaching of the liquid at the wafer edges due to surface tension impediment. Edge beads are relatively local, few millimeters wide along the periphery at the substrate and depend on spin speed, solution volatility and surface tension.[43]

1.6.3. Spray coating

This method involves generation of a mist of precursor droplets in the form of aerosols and deposition on a preheated substrate. The film genesis takes place as a result of nucleation and aggregation of aerosol droplets. The main advantage of this process as compared to spin coating is the possibility of coating complex structures, such as non-planar substrates or trenches.[44]

1.7. Nanoparticle synthesis

In this work, nanoparticles are used as building blocks for the deposition of thin films. In this section, nanoparticle synthesis in non-aqueous solvents will be described, since it is the adopted synthesis route in this work. Non-aqueous solvents have several advantages over the aqueous systems, such as better monodispersity, higher crystallinity and accessibility of a wider composition range.[45] The main difference comes from the slower reaction kinetics in organic solvents due their stronger coordination to precursors and nanoparticle surfaces. The strong solvent-nanoparticle coordination provides often high colloidal stability without the use of surfactants.[46] Therefore, the non-aqueous synthesis approach turned out to be a versatile tool for nanoparticles.[47] The formation of nanoparticles in non-aqueous solvents involve reactions between precursors (typically metal halides, acetates, acetylacetonates, nitrides etc.) with the organic solvents, typically alcohols, aldehydes and ketones, as oxygen supplying agents.[45] Benzyl alcohol is a common alcohol used in the non-aqueous synthesis of metal oxide nanoparticles, because it reacts readily with many metal oxide precursors. The reactions involve relatively simpler mechanisms, benzyl alcohol has a higher boiling point, and it acts as a reducing and growth control agent, which makes it a suitable choice for many applications.[48] In cases where a non-reductive and less coordinating synthesis solvent is desired, ketones and aldehydes are preferred instead of benzyl alcohol.[46] In this work, benzyl

alcohol and acetophenone are used for the synthesis of $CoFe_2O_4$ and $BaTiO_3$ nanoparticles, respectively.

At this point, it is also useful to review the microwave and conventional heating techniques employed to heat the synthesis mixture to the synthesis temperature.

1.7.1. Microwave heating

Microwave routes are employed widely in the synthetic chemistry in the recent years. The heating occurs as a result of interactions between the incoming electromagnetic radiation and the sample. Materials which possess high dielectric loss tangent at microwave frequencies will absorb the electromagnetic radiation effectively and volumetric heating takes place, as compared to the conventional heating where the heating occurs through radiative heat transfer from material surface to interior. The dependence of heating on sample absorption provides high selectivity, which is not accessible by conventional heating techniques. In addition, microwave heating is fast and efficient, applicable on a wide variety of systems including aqueous and non-aqueous systems, and yields samples of higher purity since the side reactions are suppressed.[49] The main disadvantage of the method is the possible temperature inhomogeneities, which may degrade the final nanoparticle quality.[50]

1.8. Selected literature on liquid phase deposition of functional thin films

1.8.1. Liquid phase deposition of ferroelectric thin films

The application field of the ferroelectric thin films emerges as the demand for low voltage electronics continues.[51] Liquid phase deposition to process ferroelectric thin films for various applications is a low cost and facile alternative to the vacuum based deposition methods. In this section, nanoparticle based and liquid phase deposition of ferroelectrics with a focus on $BaTiO_3$ will be reviewed.

Recently, a wide variety of reports appeared in the literature on chemical solution deposition of ferroelectric thin films. Chemical solution routes are grouped into sol-gel based and metallo-organic decomposition (MOD) synthetic approaches, depending on the reactivity of the precursors used. In case of sol-gel based thin film synthesis, the reactivity is high and extensive condensation occurs, whereas MOD precursors are relatively inert and do not undergo significant condensation. Due to high temperatures and large volume changes associated with MOD, their use is limited.[52] Therefore, sol-gel approaches to synthesize ferroelectrics with an emphasis on $BaTiO_3$ will be presented here.

In principle, sol-gel synthesis of ferroelectric thin films can be carried out in various ways. Often, the processing involves spin or dip coating of alkyl-chain carboxylate (typically barium acetate) and a metal alkoxide (typically titanium isopropoxide) followed by annealing between 550-850 °C.[53, 54] High processing temperatures employed to induce crystallization limits the integration of this process to conventional Si-based semiconductor technology, because of formation of intermetallics, diffusion of species, de-wetting of the bottom electrode etc. In this manner, considerable research goes into direction of low temperature processing of ferroelectrics, which relies on new methods to induce crystallization; such as laser- and microwave-assisted crystallization.[55] Other approaches focus on improving the final film quality and ferroelectric properties. For instance, crack-free $BaTiO_3$ thin films of sub 100 nm have been synthesized via controlling the drying kinetics.[56] Another work focused on synthesizing ferroelectric films of controlled porosity, through introduction of polymers into the precursor solution and their subsequent pyrolysis, with promising ferroelectric characteristics due to restricted substrate clamping due to residual porosity.[57] As a further step, an intentional mesoporous structure has been introduced in $BaTiO_3$ thin films to induce strains in the structure for enhanced T_c.[58] Through carefully designed synthesis parameters, highly oriented or dense and columnar $BaTiO_3$ thin film microstructures have been also obtained.[59]

Despite these several approaches for liquid phase deposited $BaTiO_3$ thin films of desired ferroelectricity, the final films are of low quality and exhibit limited or no functionality. The problems arise due to a transient oxo-carbonate phase of $BaTiO_3$ occurring during crystallization, which lowers the ferroelectric response, or often the crystallinity is low, accompanied by cracks, side phases and other defects.[60]

1.8.2. Liquid phase deposition of ferrimagnetic thin films

Ferrimagnetic materials bear technological importance in the field of high frequency applications, since alternating field induced eddy currents are suppressed due to the insulating nature of ferrimagnets. $CoFe_2O_4$, being a hard magnetic ferrimagnet, is particularly interesting for high density recording media, due to its high coercivity, as well as mechanical and chemical stability. In this respect, sol-gel based liquid phase deposition of ferrite thin films will be reviewed with an emphasis on $CoFe_2O_4$.

Most of the deposition approaches involve preparation of spin coating of a sol, which is based on metal chlorides or nitrates, followed by subsequent pyrolysis and annealing for crystallization.[61, 62] Hybrid approaches based on nanoparticle slurry formulations have been reported as well to prepare thick $CoFe_2O_4$ films for MEMS applications.[63] Correlation of coercivity to annealing temperature appears in many reports, mainly due to grain size-coercivity dependence in the nanosized regime.[64] Furthermore, side phases, especially CoO and α-Fe_2O_3 has been reported, which is detrimental in terms of measured magnetization at saturation, owing to the antiferromagnetic nature of CoO and α-Fe_2O_3.[62, 65] In some systems, a change in the measured magnetization at saturation has been shown, due to variation in cation redistribution during crystallization.[66] Additionally, highly oriented and epitaxial thin film microstructures could be obtained via tuning sol concentration or annealing temperature.[67]

In summary, sol-gel based liquid phase deposition approaches are more flexible in terms of inducing anisotropic, highly oriented or epitaxial thin film structures, which are shown to be beneficial to enhance the ferroelectric or ferromagnetic properties through preferential orientation or strain-related effects. However, as mentioned above, these processes are commonly combined with side phases, cracks, incomplete crystallization, difficulty in size control etc. When precursors of the ferroelectric and ferromagnetic phases are combined, for instance for artificial multiferroic heterostructures, then interdiffusion of species into each other and formation of intermetallics at the phase boundaries would be added to the aforementioned issues. In this respect, using preformed nanoparticles of defined crystallinity, phase and size is an effective low cost liquid phase film deposition approach, not only to produce single phase thin films of desired functionalities, but also for composites, either with carefully tuned properties or for the emergence of novel functionalities, such as magneto-optical thin films with perpendicular magnetic anisotropy or magnetoelectric coupling.

2. Single component BaTiO$_3$ thin films

In this chapter, optimization of the nanoparticle based liquid phase thin film deposition process to enhance the available film thickness range is demonstrated on example system BaTiO$_3$. The underlying issues related to premature cracking of the nanoparticle thin films during processing are identified and mitigated. At the same time, high transparency and ferroelectric switching characteristics of the films are maintained at the end of the film process. The results presented in this chapter are taken from the publication "Liquid-Phase Deposition of Ferroelectrically Switchable Nanoparticle-based BaTiO$_3$ Films of Macroscopically Controlled Thickness" by D. Erdem, Y. Shi, F.J. Heiligtag, A.C. Kandemir, E. Tervoort, J.L.M. Rupp, M. Niederberger in J. Mater. Chem.C, 2015, 3, 9833.

Abstract
BaTiO$_3$ films are extensively used in many electrical devices, because the material offers remarkable dielectric and ferroelectric properties. Here, we demonstrate a powerful, nanoparticle-based deposition route to BaTiO$_3$ films with systematic thickness control over a wide range up to several microns. The unusual control over the film thickness at maintenance of crack free nanostructures, phase and ferroelectric properties of the BaTiO$_3$ films allows to fabricate various future devices of different thickness requirements with a single deposition method. For this, films are deposited from stable dispersions of BaTiO$_3$ nanocrystals, synthesized via an efficient microwave-assisted non-aqueous sol-gel approach. Crack-free films of controlled thickness are obtained by a carefully elaborated, alternating process of spin-coating and intermediate drying. According to X-ray diffraction and confocal Raman microscopy, the final, sintered films consist of BaTiO$_3$ nanocrystals of about 20 nm in a hexagonal-tetragonal phase mixture. The nanoparticulate films display outstanding optical characteristics exceeding 90 % transparency above 500 nm and a band gap of 3.5 eV. Latter band gap is larger than the classic bulk material`s band gap of 3.2 eV, indicating a more electrically insulating nature of the films. Piezoresponse force microscopy gives evidence for the potent ferroelectric switching. This newly accessible film processing route with wide film thickness tuning allows for desired ferroelectric response at advantage of a wide film thickness to implicate building blocks for various applications e.g. ferroelectric random access memories, microelectromechanical systems devices or Bragg reflectors.

Introduction
Driven by the rapid development of our digital information era and the demand to transfer and compute data at low energy consumption, developing new functional thin film memories represents one of the major scientific challenges of our century. An important material in the pursuit of this quest is BaTiO$_3$, which has a variety of engineering applications as high k dielectric in field effect transistors,[1, 68] in ceramic capacitors,[69] ferroelectric based random access memory devices[56] and resistive random access memories,[70] microelectromechanical systems (MEMS) devices, multiferroics[71, 72] and planar Bragg reflector waveguides.[73] Among them, capacitor and memory based applications require thin films in sub-micron ranges due to operation voltage[74] and information storage density concerns, whereas film devices of micrometer thicknesses are desired for MEMS. In these applications the dielectric, ferroelectric and multiferroic responses exhibit pronounced size effects and it is important that the BaTiO$_3$ nanoparticles are larger than the ferroelectric limit.[75] Additionally, the composition should be phase pure to reach the targeted ferroelectric functionality.[76]

State-of-the-art BaTiO$_3$ deposition techniques succeed in producing nano-grained structures with large effective surface area to sample volume ratios. Yet, these methods are often

23

restricted to the sub-micron film thickness ranges due to slow deposition rates and cost limitations.[77] In principle, wet chemistry-based approaches are superior to vacuum-based techniques in terms of costs.[78, 79] However, traditional approaches such as sol-gel technique or pyrolysis reveal severe limitations for films thicker than one micrometer due to solvent evaporation.[80] Additionally, they often show non-desired phases such as biphasic amorphous-crystalline structures[81] or difficulties in controlling the phase-stability.[82] The reason for all these problems in depositing a crack-free film is that pyrolysis, crystallization and grain growth proceed in parallel, involving evaporation of solvents to drive the kinetics.[81] Cracking of the films due to internal crystallization processes and grain growth stresses are particularly pronounced above a critical film thickness, leading to failure in device processing. Therefore, the utilization of dispersions containing crystalline nanoparticles should represent a promising strategy to produce films with a greatly enlarged thickness range, because crystallization processes and the associated tensile stresses during sintering are avoided. In this respect, doctor blading of nanocrystal slurries, assisted by plasticizers for green strength, perform well for micrometer thick films, but fail to produce films of nm thickness.[83] Other approaches to make nanocrystalline BaTiO₃ films with thicknesses from some tenths of nanometers to several microns include colloidal film deposition techniques such as spin and dip coating of nanocrystal dispersions. Typically, the dispersion media are organic due to their good substrate wetting properties and high volatility.[43] Although non-aqueous sol-gel methods often lead to well-dispersible nanoparticles and thus are widely employed,[84] additional surface functionalization with sterically stabilizing molecules to improve the stability of the dispersions might be required.[85]

However, this additional amount of organics introduces capillary stresses during its thermal removal, already resulting in premature cracking in films of just sub-micrometer thickness.[40, 86]

While colloidal dispersion techniques have been applied to SiO₂,[87, 88] TiO₂,[89] and SnO₂[90, 91] based films with thicknesses in the sub-micron range, no deposition technique is available to produce one of the most relevant electroceramics, namely, BaTiO₃, with a broader range of film thicknesses. As a matter of fact, wet chemical deposition routes bridging the gap between the different methods and thus covering a broad range of thicknesses would be highly beneficial from a technical as well as from a scientific point of view (Figure 2.1). Moreover, integration of nanoparticle thin films into devices is often problematic and it is challenging to achieve the targeted functionality due to unwanted size effects and film quality issues related to impurities, surface roughness, porosity, cracks and other inhomogenieties. In this paper, we describe a simple liquid phase deposition route to BaTiO₃ films with controlled thicknesses up to the micron range using BaTiO₃ nanoparticle dispersions. Phase-pure BaTiO₃ nanoparticles with high crystallinity and larger than the ferroelectric size limit are obtained through an efficient microwave-assisted non-aqueous synthesis, offering well-defined nanoparticle building blocks for achieving the targeted ferroelectric functionality. The films prepared from these dispersions by spin coating were sintered and thereby enlarged volume fractions of grain boundary to grain can be realized, which is of great interest to tune the dielectric and ferroelectric properties over a wider range when compared to classical wet chemical methods such as sol-gel based deposition methods,[53, 92, 93] or spray pyrolysis.[94] One of the main parameters that can be adjusted to widen the accessible film thickness range is the optimization of the drying process. For this reason, we had a closer look at the drying process and based on these investigations we developed engineering guidelines for the selection of the optimal drying temperature regime to ensure the removal of the organic impurities without cracking. For the deposition Si and Pt/SiO₂/Si substrates were chosen, because they are compatible with the conventional Si semiconductor technology. As a proof-of-concept for the functionality of the films, the ferroelectric and optical responses were

tested, representing a first step toward future integration of these films into ferroelectric/multiferroic devices.
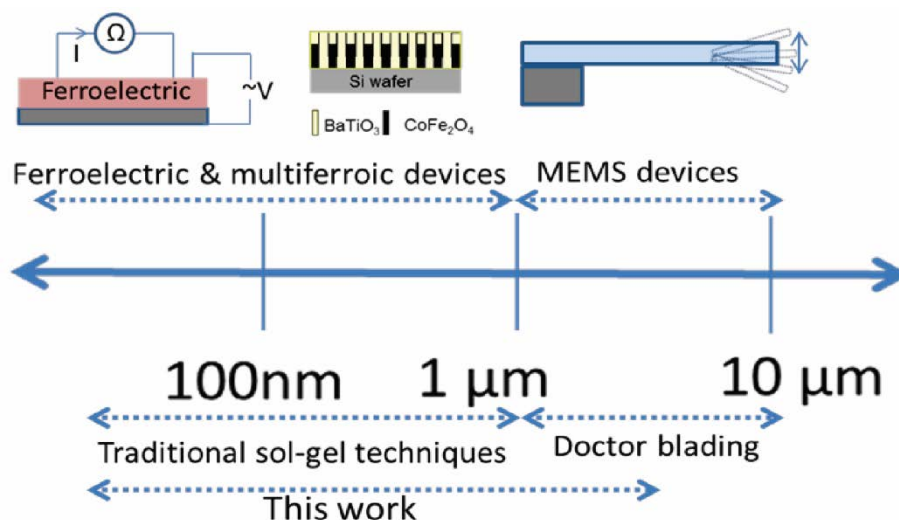
Figure 2.1 Overview of various device applications with their required film thicknesses and the corresponding liquid phase deposition for BaTiO$_3$ thin films.

Results and Discussion

BaTiO$_3$ with crystal sizes in the range of 10 nm are synthesized in acetophenone as solvent.[95] The nanoparticles are large enough to exhibit pronounced ferroelectric properties in contrast to BaTiO$_3$ nanoparticles prepared in benzyl alcohol[96] (although also these small particles of 5 nm exhibited some ferroelectric properties[97]). The as-synthesized nanoparticles are functionalized with 2-(2-(2-methoxyethoxy)ethoxy)acetic acid (MEAAA),[98] transformed into stable dispersions and then used for the deposition of BaTiO$_3$ films with varying thicknesses by several spin-coating and drying cycles. These steps are repeated until the desired thickness is reached. Finally, all films are sintered at 700 ^{o}C. The film preparation procedure is summarized in Figure 2.2a. A transmission electron microscopy (TEM) image of the as-synthesized nanoparticles and a cross-sectional scanning electron microscopy (SEM) image of the resulting film after sintering are shown in Figure 2.2b and 2.2c, respectively. X-ray diffraction (XRD) and Raman spectroscopy are employed for the structural analysis of both the as synthesized nanoparticles and the nanoparticle thin films. All diffraction peaks in the XRD of the nanoparticles and the films can be indexed to the cubic BaTiO$_3$ phase without any crystalline side phases such as BaCO$_3$, Figure 2.2d, in agreement with the literature.[99] For comparison, XRD patterns of both powder and thin film samples are measured using thin film optics to have the same instrumental contribution to peak broadening which, however, reduces the signal-to-noise ratio. The average crystallite size is estimated to be 13 nm and 20 nm using the Scherrer equation on the (110) reflection[100] for the nanoparticles and the films, respectively. In this size regime, it is not possible to differentiate between tetragonal and cubic BaTiO$_3$ due to the peak broadening at sub-140 nm grain size.[101, 102] Hence, we perform Raman spectroscopy to further elucidate the near order characteristics, Figure 2.2e.
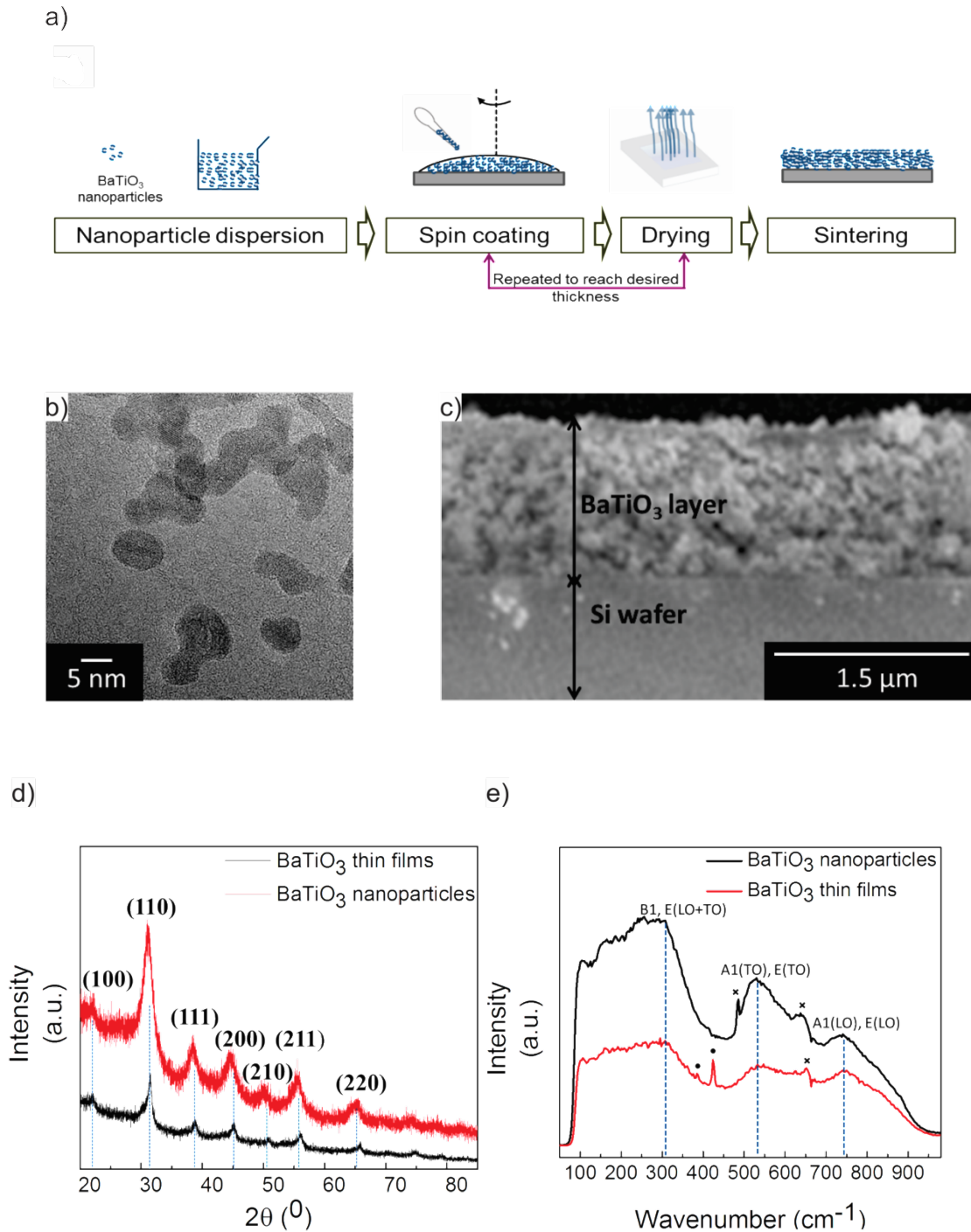
Figure 2.2 a) Flowchart of the film deposition process, b) TEM image of the as-synthesized BaTiO$_3$ nanoparticles, c) cross-sectional SEM image of a 1 μm thick BaTiO$_3$ nanoparticle film, d) XRD of BaTiO$_3$ nanoparticles and nanoparticle films, e) Raman spectra of BaTiO$_3$ nanoparticles and nanoparticle films.

The nanoparticles and films are characterized by three broad Raman modes at 170 cm^{-1} (*A1* mode of *T1*), 307 cm^{-1} (*TO* mode of *B1*), 530 cm^{-1} (*TO* mode of *A1*) and 740 cm^{-1} (*LO* mode of *E*).These Raman bands are in agreement with the stretching and bending modes for tetragonal BaTiO$_3$, Table 1 and Ref.[103] The small Raman peak assigned to the *TO* mode of *B1* exhibits broadening and a lowered intensity in comparison to the Raman spectrum of bulk BaTiO$_3$, indicative for small tetragonal distortions and a generally small particle size. We observe a blue shift for the *TO* mode of *A1* and the *LO* mode of *E* in comparison to the single crystal BaTiO$_3$ data pointing to lattice strain.[104] Additional E_{1g} and A_{1g} Raman vibrations marked with an asterisk originate from the presence of additional hexagonal phases of BaTiO$_3$, Table 2.1.

Table 2.1 Assignment of the observed Raman bands

Raman shift (cm^{-1})	This Work		BaTiO$_3$		Literature
	Symmetry	Crystal Structure	Nanoparticles	Thin Films	
307	B1, E(LO+TO)	Tetragonal	*	*	[103]
488	E$_g$	Hexagonal	*	*	[105]
530	E(TO), A1(TO)	Tetragonal	*	*	[104]
640	A$_{1g}$	Hexagonal	*	*	[105]
740	E(LO), A1(LO)	Tetragonal	*	*	[104]

The co-presence of the hexagonal and tetragonal BaTiO$_3$ phases is reported in the literature for particles with average size below 40 nm.[101] The Raman bands marked with a dot in the film spectrum originate from the substrate. We summarize the assignment of all Raman vibrations together with a comparison of literature data in Table 2.1.

In the following section, we investigate the complex interplay between the organic residues and the drying kinetics for the fabrication of nanoparticle-based BaTiO$_3$ films to elaborate the upper limit of the film thickness accessible by this process. As it is typical for a non-aqueous synthesis route and for a dispersion based on organic solvents, all kinds of organic residues have to be carefully removed to avoid capillary stresses and subsequent cracking of the films during sintering.

To get thick films, several spin coating and drying steps are required. Using a dispersion with a nanoparticle concentration of 60 mg/ml every spin contributes to about 100 nm to the film thickness. According to SEM cross section analysis, a crack-free, approx. 450 nm thick film composed of BaTiO$_3$ nanoparticles was deposited via four cycles of spin coating-intermediate drying at 200 °C, followed by a single final sintering at 700 °C, Figure 2.3a. The intermediate

drying temperature was high enough to ensure evaporation of the dispersing medium (e.g. ethanol), enabling the stacking of the BaTiO$_3$ nanoparticles without dissolution of the previous coatings into a multilayer structure. However, delamination between the layers becomes a problem, when a critical thickness of approx. 500 nm is exceeded after depositing the 5th cycle, as revealed by a SEM cross section image in Figure 2.3b.

To gain a fundamental understanding of the role of drying and compaction for this particular case of nanoparticle deposited films and to give hands on engineering guidance on how to deposit crack-free and micrometer thick films, thermogravimetric analysis (TGA) and Fourier transform infrared (FTIR) spectroscopy were carried out, Figure 2.3c,d. In the TGA, up to a temperature of 500 °C, a weight loss of approx. 15 wt% is measured, Figure 2.3c. The onset temperature of the main weight loss is around 300 °C, and it is attributed to the outgassing of organics without affecting BaTiO$_3$, which is stable in this temperature range.[106] We analyze the organics in an as-deposited film and in a film dried at 200 °C by transmission FTIR, Figure 2.3d. Both spectra reveal three absorption bands at 3500 cm^{-1}, 2880 cm^{-1} and below 2200 cm^{-1} (below 2200 cm^{-1} the glass substrate absorbs). We ascribe the first two IR absorption bands observed at higher wavenumbers to the O-H stretching vibrations of adsorbed water,[107] and to aliphatic C-H stretching vibrations[108] originating from the stabilizing agent MEEAA. For comparison, the FTIR spectrum of MEEAA is also shown in Figure 3c, revealing two additional strong absorption bands in the glass absorption region. These bands at 1735 cm^{-1} and 1100 cm^{-1} belong to C=O and C-O-C vibrations.[109] It is interesting to note that the absence of any absorption bands from the aromatic ring of acetophenone between 3000-3100 cm^{-1} indicates that no acetophenone is bound to the surface of the BaTiO$_3$ nanoparticles. Accordingly, acetophenone does not play any significant role in the drying chemistry. Heating the as-deposited films to 200 °C results in a significant reduction of the IR absorption band intensity for the aliphatic species and for the water vibrations. These absorption band intensities are even more reduced in the sample dried at 500 °C. The outgassing of organics is responsible for the great amount of weight loss observed in Figure 2.3c. When dried at 200 °C, MEEAA is still present on the BaTiO$_3$ nanoparticle surfaces. The decomposition of MEEAA mostly takes place during the subsequent sintering of the thin films. Based on TGA and FTIR data we can reasonably relate the premature cracking of the BaTiO$_3$ films during sintering to tensile stresses as a result of the removal of organics. Obviously, a drying temperature of 200 °C is not high enough to remove enough organics to ensure a sintering process without crack formation. On the other hand, for drying or calcination temperatures higher than 500 °C, most organics are removed and the weight loss is below 1 wt% up to a temperature of 800 °C, Figure 2.3c. At this point, due to the minor amount of organic residues cracking stresses are not to be expected anymore. As a proof-of-concept we deposited successfully a crack-free, 3 micrometer thick BaTiO$_3$ film in four consecutive spin coating-calcination steps at a temperature of 500 °C, as shown in the SEM cross-sectional image, Figure 2.3e. In general, several film deposition parameters have an influence on final film thickness, for example spinning speed and time, dispersion concentrations, number of spin coating-drying cycles etc. In this study, spinning speed and time are optimized and kept constant at a spinning rate of 1000 rpm of total 20 seconds of spinning time for all film depositions, since higher spinning speeds are known to disrupt film uniformity in case of low boiling point dispersion media, such as ethanol, the chosen medium for this study. Instead, the film thickness is easily tuned via the number of spin coating-drying cycles and/or via the concentrations of the dispersions in the range from 50 nm up to 700 nm per deposition (see Supporting Information, Figure S2.1). Atomic force microscopy (AFM) images of the films indicate that the surface roughness is typically in the range of 10 nm, but can be as low as 5 nm (see Supporting Information, Figure S2.2).
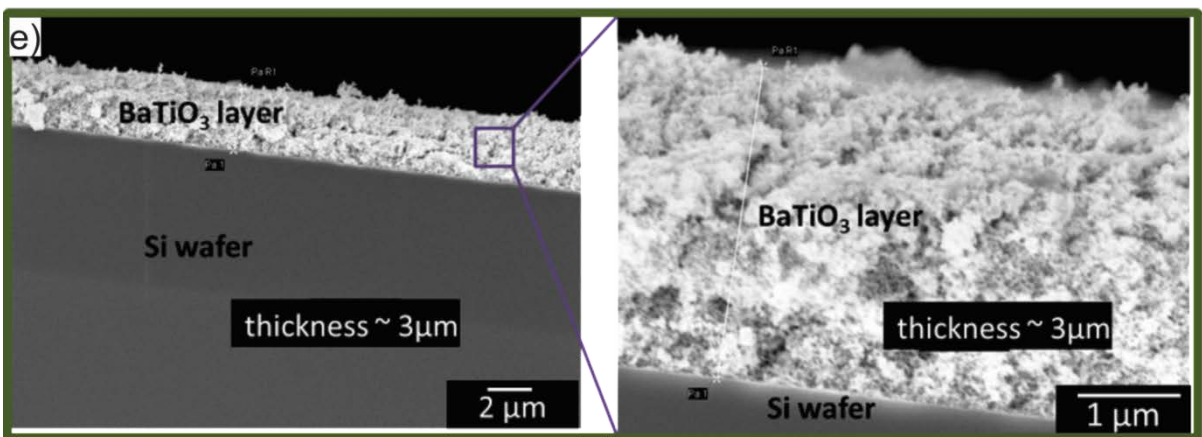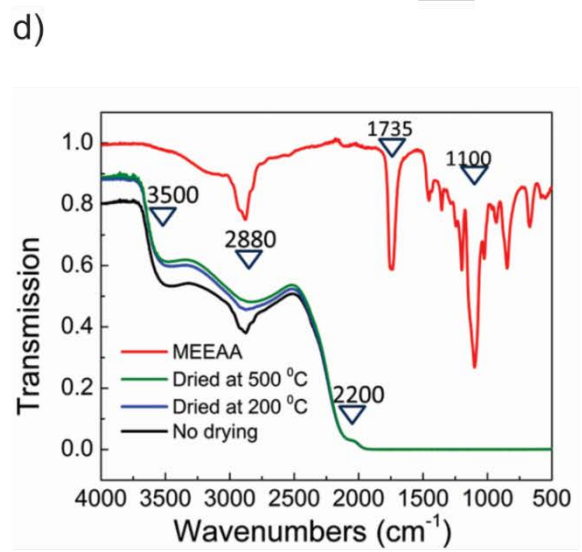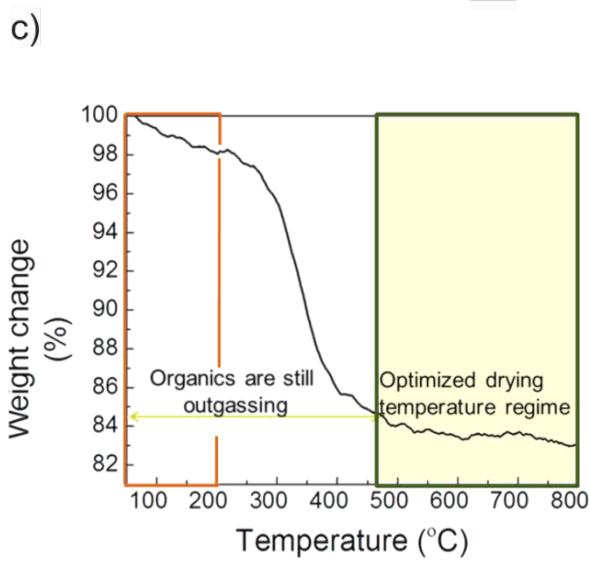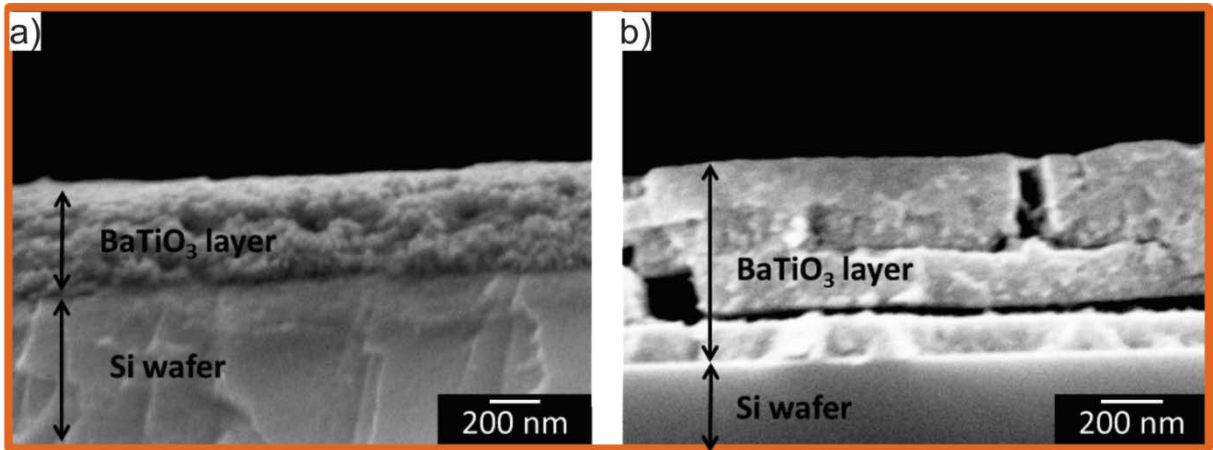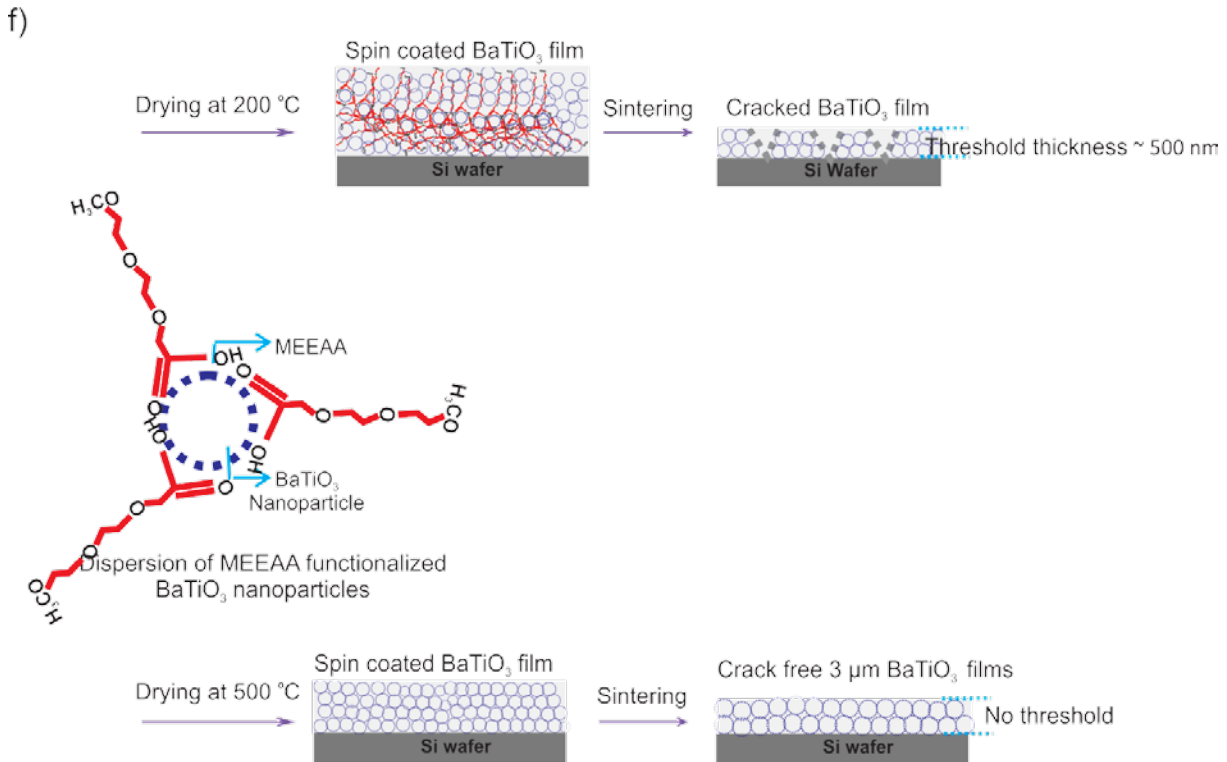
Figure 2.3 Cross-sectional SEM images of a) 450 nm and b) 600 nm thick film. c) TGA graph, d) FTIR spectra of the films dried at different temperatures, e) cross-sectional overview and magnified SEM images of a 3 μm thick film. f) Schematic drawings showing the effect of incomplete removal of the organics during drying on the microstructure of the films.

Optical band gap and optical properties

The optical properties of the heated BaTiO$_3$ nanoparticle thin films in the visible range are examined via their reflectance spectra and compared to as-synthesized nanoparticles, Figure 2.4a. The BaTiO$_3$ nanoparticles exhibit a maximum diffuse reflectance of 75 %, whereas the 250 nm thick BaTiO$_3$ films exhibit 23 % maximum diffuse reflectance. We calculate the band gaps for the BaTiO$_3$ nanoparticle powder and the films by Tauc plots of *(f(α)hν))^2* and Kubelka-Munk calculation for the absorption coefficients,[110] Figure 2.4b. Using this approach, the band gap of the as-synthesized nanoparticles is 3.8 eV and 3.5 eV for the films. Obviously, the BaTiO$_3$ nanoparticles have a significantly increased band gap compared to the bulk value of 3.2 eV.[111] The nanoparticle powder and the nanoparticle-based films show an increased band gap of +0.3-0.6 eV and are thus of a more electrically insulating nature.
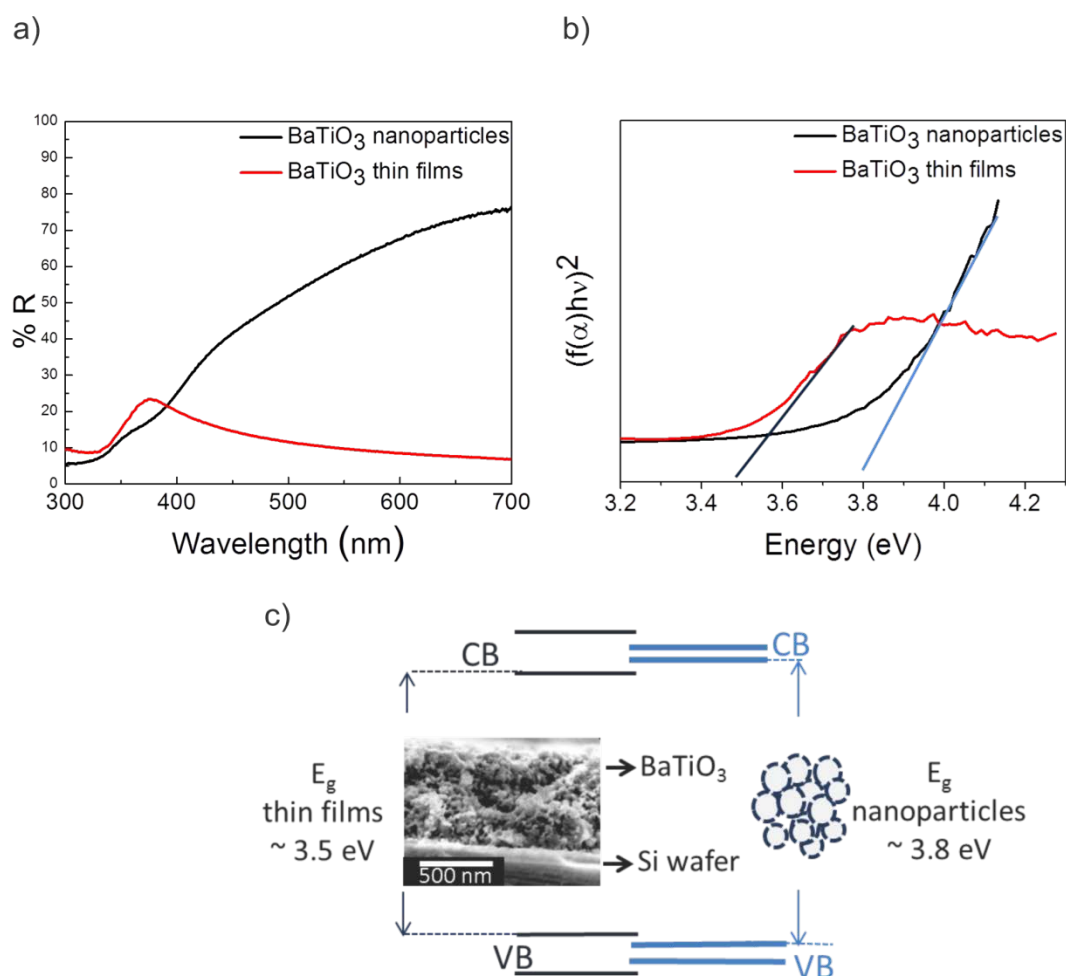
Figure 2.4 a) UV-*vis* reflectance spectra, b) corresponding Tauc plots of BaTiO$_3$ nanoparticles and nanoparticle-based films. c) Schematic drawing representing the band gaps E$_g$ of as-synthesized nanoparticles and sintered thin films.

Several effects may play a role in band gap widening in nanomaterials,[111, 112] however narrowing of conduction and valence band originating from the nanocrystalline nature of the films is believed to be the most relevant mechanism for the wider band gap of our system.[113] The large band gap also implicates that the sample is chemically pure, because foreign atoms would decrease the transparency range.[114]

The large band gaps E$_g$ of the BaTiO$_3$ thin films result in outstanding transparency in the visible range, exceeding 90 % transparency above 500 nm for films approx. 200 nm and 100 nm thick (Figure S2.3a). Such optical properties make both, the BaTiO$_3$ nanoparticles and the nanoparticle-based films promising candidates for future devices in the field of electrooptics[115] and integrated optics, as single phase as well as constituent in multiferroic composite materials.[116] A more detailed discussion of the optical characterization and porosity of BaTiO$_3$ films fabricated from dispersions with varying nanoparticle concentrations are given in the Supporting Information, Figure S2.3b and S2.3c. The refractive index of the films can be tuned in the range from 1.5-1.8 *via* altering the concentration of the initial colloidal dispersion, while maintaining the extinction coefficients low. Films with different porosities and thus different refractive indices can be deposited by our method. This flexibility facilitates further applications as Bragg-stacks, enables variation of the refractive index contrast by liquid impregnation of the pores and opens up possibilities for sensing.

Ferroelectric switching of nanoparticle-based films

We exemplify and confirm, as a proof-of-concept for the applicability, the local ferroelectric switching behavior of the BaTiO$_3$ films and the corresponding hysteresis loops via switching spectroscopy piezoresponse force microscopy (PFM), Figure 2.5. An approximate value for the longitudinal piezoelectric strain coefficient d$_{33}$, responsible for the longitudinal strains in case of vertically applied electric fields, of a maximum of 5 pm/V is measured for 200 nm thick BaTiO$_3$ nanoparticle films, Figure 2.5a. Despite the crack free thin film microstructure, d$_{33}$ values are limited to few picometers per volt in this grain size regime as reported previously in the literature for sol gel deposited nanocrystalline BaTiO$_3$ thin films of similar grain sizes[117] and our findings perfectly agree with the given particle size- piezoresponse arguments. An exact calculation of the piezoelectric coefficient d$_{33}$ from the piezoresponse data is difficult due to the inhomogeneous electric field between the PFM tip and the sample.[118] Additionally, the relatively high shear piezoelectric coefficient, d$_{15}$, for these materials especially in the case of nanocrystalline thin films[119] causes a significant piezoresponse in the lateral directions in case of a vertically applied electric field. The full phase shift in the piezoresponse proves that complete switching over 0-180° takes place along the *x*-axis upon change of the bias polarity, as seen from the response versus applied potential curve, Figure 2.5b.

a)

b)
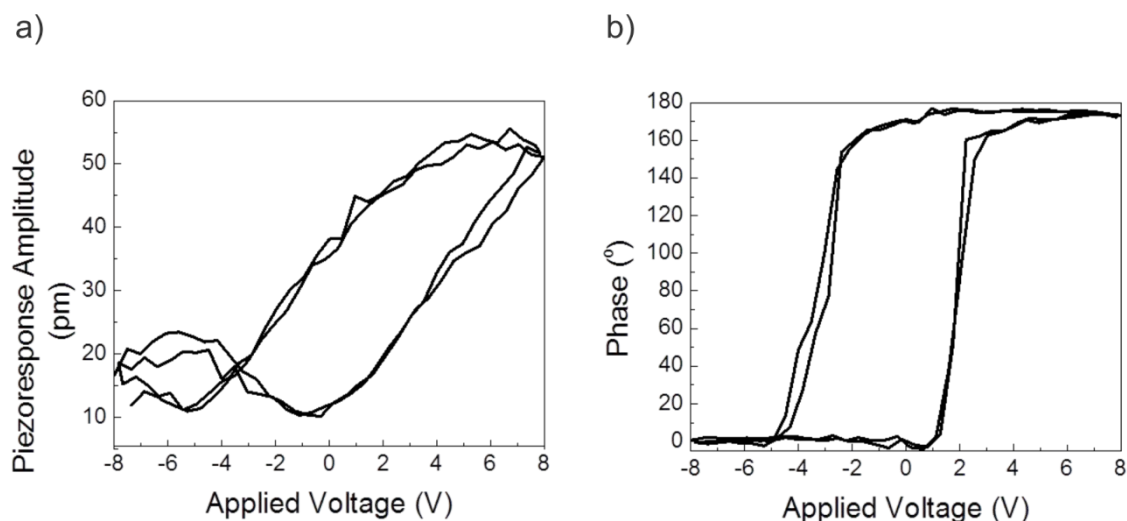
Figure 2.5 a) Amplitude and b) phase shifts of the piezoresponse local hysteresis loops of BaTiO$_3$ nanoparticle thin films

Conclusion
This work shows that a colloidal route based on preformed nanoparticles can successfully be applied to the preparation of BaTiO$_3$ films of a broad range of thicknesses from some tenths of nanometers up to a few micrometers. Unlike classic wet-chemical techniques, crystallization is already accomplished at deposition due to the nanocrystalline nature of the colloidal dispersions. Correlation between the dispersing medium ethanol, the dispersant MEEAA and the drying conditions is observed and engineering guidance on how to make crack-free films is provided. An increase in the electronic band gap in comparison to bulk indicates that the films are more insulating, and thus reach an outstanding transparency of more than 90 % in the visible range for several hundred nanometer thick films. Such improved characteristics enable a wider operation range for electro-optical devices. A first proof-of-concept for the ferroelectric nature of the nanoparticle-based films is evidenced by switching spectroscopy PFM measurements. The fact that nanoparticle-based films can now be produced over a wider range of thicknesses without cracking, but with high grain interconnectivity and desired ferroelectric and optic properties represents a promising

step towards the fabrication of multiferroics, ferroelectrica and applications thereof in random access memories by low-cost wet-chemistry approaches.

Experimental procedure
Materials

Dendritic metal pieces of barium (99.99 % purity), titanium (IV) isopropoxide (99.999 % purity) and 2-[2-(2-methoxyethoxy)ethoxy]acetic acid (technical grade) and hexane (> 95 % purity) are purchased from Aldrich fine chemicals and used without any further purification. Ethanol of 99.8 % purity was obtained from Fluka. Acetophenone (98 % purity) is obtained from Acros organics and degassed via 3 cycles of freeze-thaw solvent degassing before the synthesis. Fused silica, <100> oriented p-type Si wafers, and Pt/TiO$_2$/SiO$_2$/Si wafers (MTI Corp, USA) are used for film deposition.

Synthesis of Particles and Dispersions

The synthesis is a combination and adaptation of previously reported protocols.[95, 120] In a typical synthesis, 137 mg dendritic Ba is dissolved in 5 ml degassed acetophenone at 80 ^{o}C in an argon filled glove box, followed by dropwise addition of a molar equivalent of titanium isopropoxide. The mixture is transferred to a microwave vial, sealed and exposed to microwave irradiation for 30 minutes at a synthesis temperature of 220 ^{o}C using a CEM Discovery reactor. The nanoparticles are centrifuged off, washed twice with ethanol and finally sonicated for 45 minutes in 5 ml 0.3 M ethanolic MEEAA solution using Branson B3510 ultrasonic cleaner. After sonication, the nanoparticles are stirred overnight in this mixture to ensure sufficient binding of the stabilizing molecules to the nanoparticle surfaces. In the following step, an excessive amount of hexane (5:1 hexane to ethanol ratio in volume) is added and the mixture is centrifuged in order to separate the nanoparticles from excess stabilizing agent. Afterwards, the BaTiO$_3$ nanoparticles are re-dispersed in ethanol with a subsequent sonication step.

Synthesis of Films

BaTiO$_3$ nanoparticle thin films are fabricated using spin coating with intermediate drying at 200 ^{o}C or 500 ^{o}C at a maximum spinning speed of 1000 rpms in a total spinning period of 20 seconds using a Laurell WS650 spin coater. Typically, the concentrations of the nanoparticle dispersions are altered between 30 and 250 mg/ml to obtain thickness values per spin coating between approx. 50 and 750 nm. To deposit a 3 μm thick film, 4 spin coating cycles with 500 ^{o}C intermediate drying are carried out, followed by a final sintering step using nanoparticle dispersions of 250 mg/ml initial concentration. All film deposition processes prior to sintering are carried out in a laminar flow controlled, synthetic air filled glovebox. After all spin coating–drying cycles, only one sintering step for compaction at 700 ^{o}C for 2 hours in air with 4 hours of ramping (approx. 2.8 ^{o}/min ramping rate) is done in a Nabertherm L 3/11/B170 laboratory muffle furnace to conclude the film making process.

Characterization

SEM images are obtained from films deposited on Si wafers at an operation voltage of 3-5 kV using a LEO 1530 scanning electron microscope. Transmission electron microscopy (TEM) studies are performed on FEI Tecnai F30 FEG operated at 300 kV. Powder and

film XRD patterns are obtained using a Panalytical X'Pert Pro diffactometer with Cu Kα source in grazing incidence geometry between 20-85° using 50 seconds per step and step size of 0.01^o and 0.0065^o for thin films and powders respectively. To investigate the near order characteristics of the films and nanoparticles, a WITec CRM200 Confocal Raman Microscope with a green laser of 532 nm is employed. Thermogravimetric analysis is carried out on post synthesis functionalized powders and films dried at 200°C using Mettler Toledo TGA/SDTA851. Samples are heated from 50°C to 800°C at a heating rate of 5°C/min under air. FT-IR spectroscopy is performed on a Bruker Alpha FT-IR Spectrometer on undried, 200°C and 500°C dried thin film samples on glass substrates. UV-vis spectra are obtained by a JASCO V-770 spectrophotometer with an ILN-725 integrating spheres accessory with background subtraction and with respect to standard BaSO$_4$ powder. Topography images are obtained by intermittent contact mode AFM of Asylum Cypher^{TM} using AC160TS-R3 tips and root mean square surface roughness was calculated accordingly. The ferroelectric properties are investigated using DART-SSPFM mode of Asylum Cypher^{TM} using doped diamond PFM tips from NDMDT on films deposited on Pt/TiO$_2$/SiO$_2$/Si substrates with Pt bottom electrode being grounded during the measurements. Deflection in volts and thermal calibration of the tips are done prior to PFM measurements and the presented hysteresis curves are obtained in the remnant mode to minimize electromechanical tip-sample interactions with an ac reading voltage of 1V.

Acknowledgements

Supporting Information
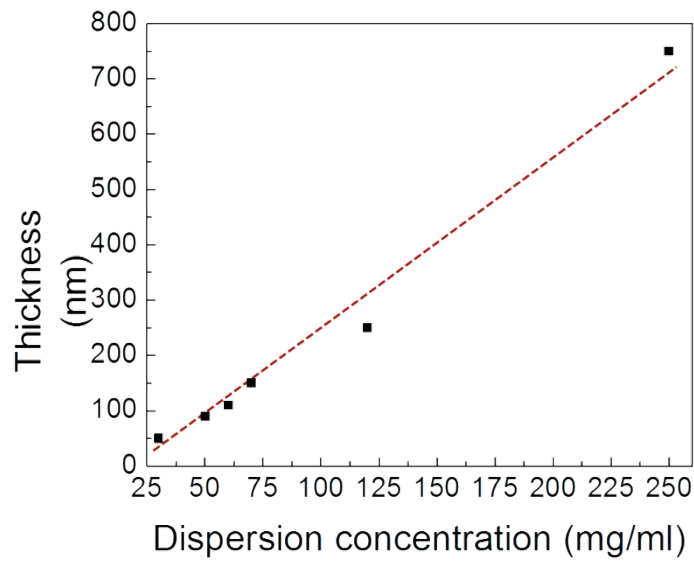
Figure S2.1 Thin film thickness (from cross-sectional SEM analysis) *vs.* concentrations of dispersions. The dashed line is a guide to the eye to show the linear dependence.
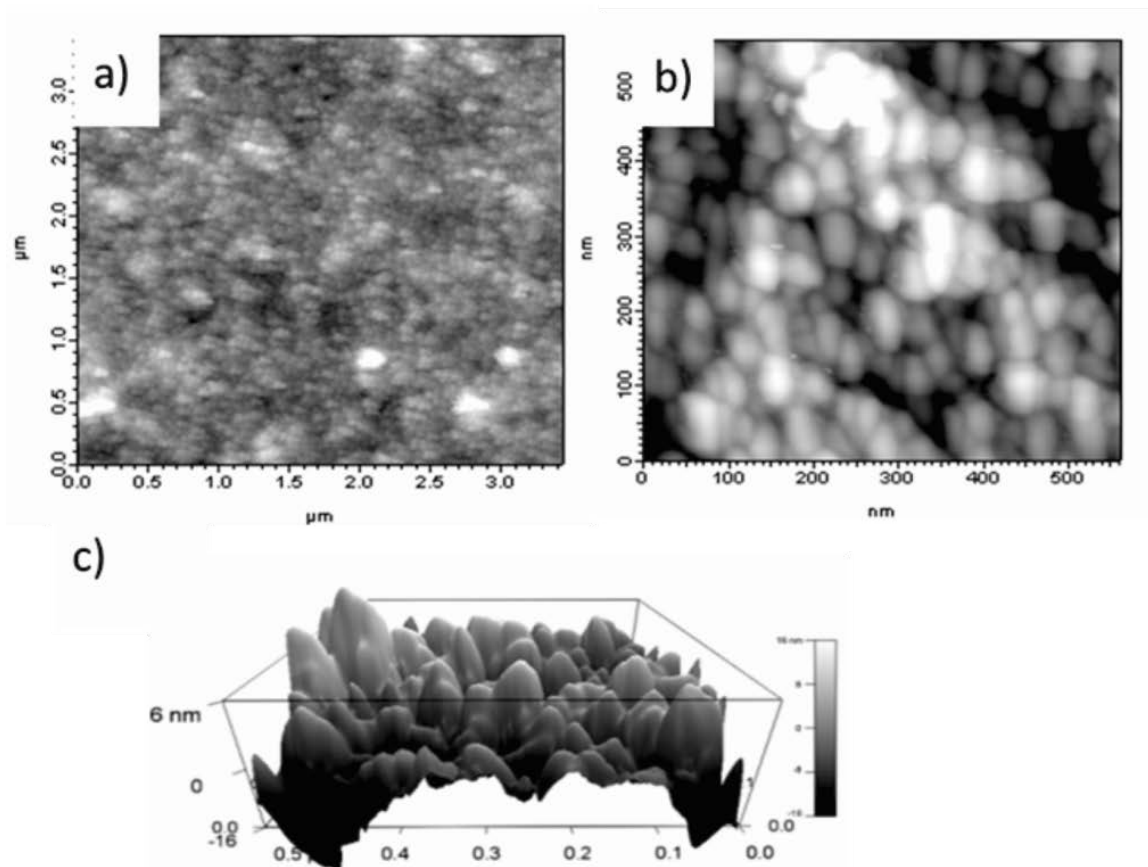
Figure S2.2 Height retrace of a) 5 μm × 5 μm and b) 500 nm × 500 nm scanned area of BaTiO$_3$ thin films of 3 μm thickness, c) 3-D height retrace image of (b).

Optical characteristics of BaTiO₃ nanoparticle films made from different concentrations of initial nanoparticle dispersions.

All the films exhibit more than 90% transparency above 500 nm range and therefore are of good optical quality (Figure S3a). The optical constants (refractive index n and absorption coefficient k) of the films are calculated from the Kramers-Kronig transformations of their reflectance spectra (Figure S4). The refractive index of the films at 632 nm is 1.8 for the films fabricated from 120 mg/ml dispersion concentration and 1.5 for the other set of films. The absorption coefficients of the films are set to 0 above 500 nm due to their high transparency (Figure S3b). From the refractive index data (Figure S3b), the density of the films is approximated using the Lorentz-Lorenz relation,[121] and estimated to be 76% (dispersion concentration of 120 mg/ml) and 63% (dispersion concentration of 60 mg/ml), respectively, at a sintering temperature of 700 °C. For comparison, a literature value of 2.4[122] for the refractive index of BaTiO₃ at 632 nm was taken. Based on these results, it is obvious that films of different porosity and refractive index can be manufactured by adjusting the initial concentration of the nanoparticle dispersions. Such fabrication flexibility has implications on distributed Bragg reflectors and gradient refractive index coatings. Moreover, the porosity of the films can easily be tuned, facilitating impregnation of liquids to further modify the refractive index.
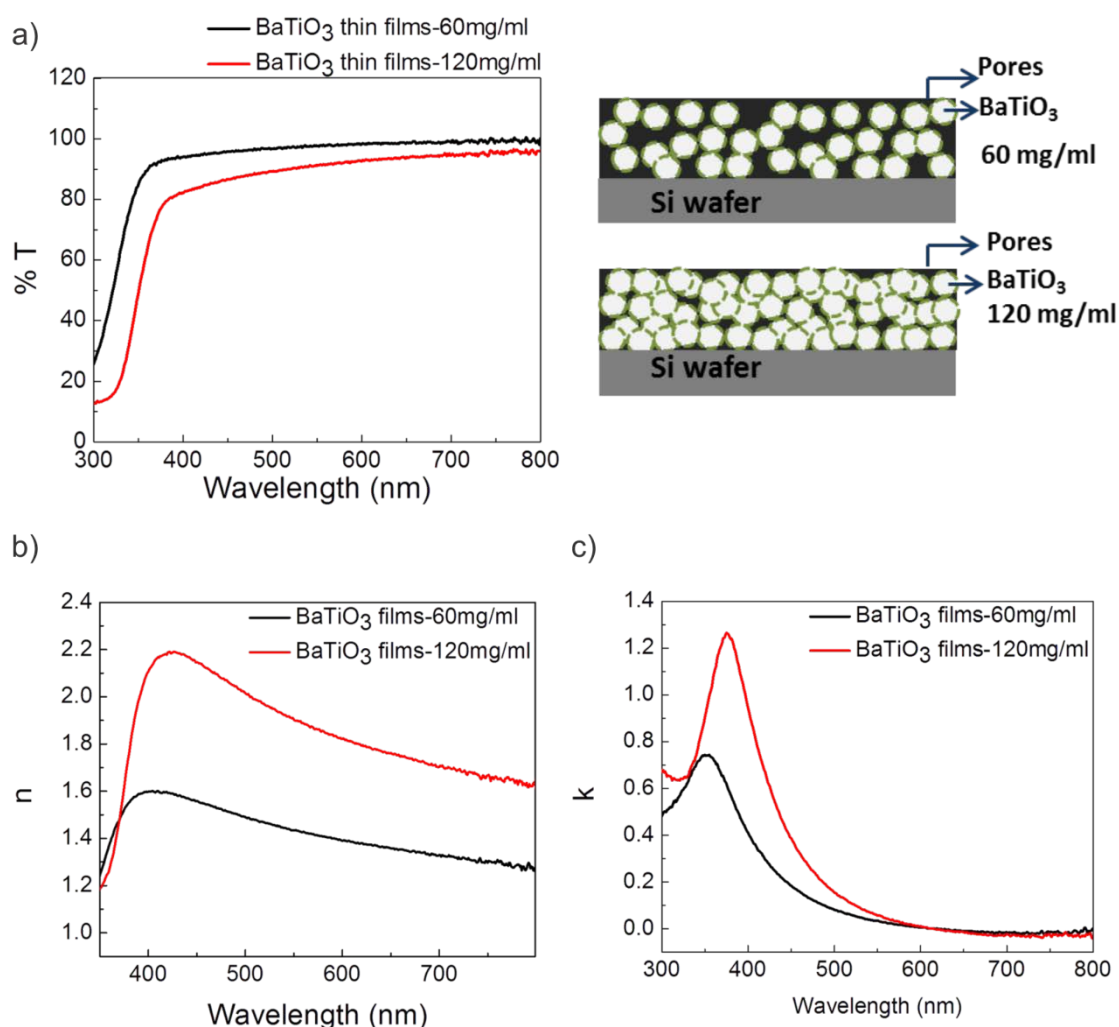
Figure S2.3 a) UV-*vis* spectra, b) refractive index (n) and c) extinction coefficient (k) of BaTiO₃ nanoparticle thin films of 120 mg/ml and 60 mg/ml dispersion concentrations.
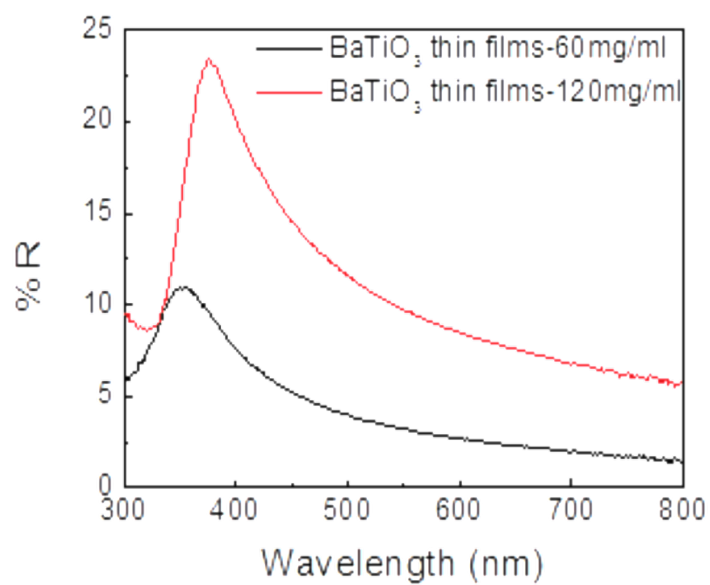
Figure S2.4 Reflectance spectra of BaTiO$_3$ thin films fabricated from initial nanoparticle dispersions of 60 and 120 mg/ml concentrations.

3. CoFe$_2$O$_4$-SiO$_2$ nanocomposite thin films for magnetic and magneto-optical applications

In this chapter, a further step will be taken into the developed nanoparticle based thin film deposition approach to synthesize nanocomposite thin films of carefully tuned optical and magneto-optical properties. Using co-dispersions of CoFe$_2$O$_4$ and SiO$_2$ nanoparticles, refractive indices, transparency range, and magneto-optical properties can be effectively modified in the final sintered films. It is shown that the deposited thin films can be readily implemented into existing magneto-optical technologies; owing to the high enough figures of merits and refractive indices, which are suitable for SiO$_2$ based optical systems. Moreover, the constrained sintering conditions create perpendicular magnetic anisotropy and spontaneous magnetization. The results shown here are taken from the publication with the title "CoFe$_2$O$_4$ and CoFe$_2$O$_4$-SiO$_2$ nanoparticle thin films with perpendicular magnetic anisotropy for magnetic and magneto-optical applications" by Derya Erdem, Nicholas S. Bingham, Florian J. Heiligtag, Nicolas Pilet, Peter Warnicke, Laura J. Heyderman, Markus Niederberger and accepted for publication by the journal of "Advanced Functional Materials".

Abstract

This paper presents an efficient colloidal approach to process CoFe$_2$O$_4$ and SiO$_2$ nanoparticles into thin films for magnetic and magneto-optical applications. Thin films of varying CoFe$_2$O$_4$-to-SiO$_2$ ratios (from 0 wt% to 90 wt%) were obtained by sequential spin coating-calcination cycles from the corresponding nanoparticle dispersions. Scanning electron microscopy (SEM) analysis revealed a crack free and nanoparticulate structure of the sintered films with thicknesses of 480-1200 nm. Results from the optical characterization indicated a direct band gap ranging from 2.6-3.9 eV depending on the SiO$_2$ content. Similarly, the refractive indices and absorption coefficients were tunable upon SiO$_2$ incorporation. In-plane measurements of the magnetic properties of the CoFe$_2$O$_4$ films revealed a superparamagnetic behavior with both Co^{2+} and Fe^{3+} contributing to the magnetism. Polar Kerr measurements showed the presence of a spontaneous magnetization in the CoFe$_2$O$_4$ and CoFe$_2$O$_4$-SiO$_2$ (with SiO$_2$ < 50 wt%) films, pointing to magnetic anisotropy perpendicular to the substrate. The origin of this effect is attributed to the constrained sintering conditions of the nanoparticulate film and the negative magnetostriction of CoFe$_2$O$_4$.

Introduction

Magnetic materials play a key role in many technological applications such as magnetic and magneto-optical recording, integrated optics or waveguides. Cobalt ferrite is an attractive material, because it offers a combination of semiconducting[123] and magnetic properties, including high coercivity, anisotropy and magnetostriction.[124] This results in a vast range of applications in magnetoelectrics,[125, 126] magnetic strain sensors,[127] resistive switching random access memories,[128] high density magnetic recording media[126, 129] and microelectromechanical systems.[63] In addition, it has a high Kerr rotation in the 400-800 nm range, which is accessible by the common lasers used in the optical industry.[130] Nanostructured CoFe$_2$O$_4$ thin films are of particular interest for data storage, due to potential increase in the stored bit density.[131] In addition, nanostructured CoFe$_2$O$_4$ based materials find use in magneto-optics due to suppressed laser - nanoparticle interactions and a congruent enhancement in the signal to noise ratio.[132] However, the high refractive index (2.5) and absorption in the visible and near IR-range limit the integration of CoFe$_2$O$_4$ films into optical

systems. Typically such systems rely on silica based materials with a refractive index of 1.5.[133] Thus, nanocomposite thin films composed of CoFe$_2$O$_4$ and SiO$_2$ would significantly widen the application field of this material. At the same time, down-scaling of the magnetic phase is limited, because the lack of coercivity in superparamagnetic particles hinders their utilization in recording applications. Nevertheless, it is possible to take advantage of magnetic anisotropy to induce coercivity on the nanoscale, thereby overcoming the superparamagnetic size limit.[131] Indeed, the presence of perpendicular magnetic anisotropy in thin films is desired for high density perpendicular magnetic[134] and magneto-optical recording. With very few exceptions that involved sol-gel approaches,[135, 136] such materials have typically been prepared via gas phase deposition methods, and the resulting perpendicular magnetic anisotropy relies on the epitaxy induced lattice strain coupling to the spins.[124, 137] Unfortunately, in these cases the associated deposition rates are low and the equipment costs for manufacture are high. Wet chemistry based deposition methods, on the other hand, are more cost effective and the deposition rate is higher.[138] Nevertheless, one has to keep in mind that a precise control over the crystallinity and phase purity[136] is extremely important in magnetic films, because they play a crucial role in determining the magnetic[139] and magneto-optical properties. From this point of view, using dispersions with preformed nanoparticles of defined composition and structure as starting materials to deposit thin films is a promising strategy.[140, 141]

Here we report the fabrication of cobalt ferrite based nanocomposite thin films by several spin coating-calcination cycles of the corresponding CoFe$_2$O$_4$-SiO$_2$ nanoparticle dispersions followed by sintering. We show that this colloidal deposition route represents an effective way to fabricate thin films with perpendicular magnetic anisotropy. The nanoparticulate nature is maintained and offers a high signal to noise ratio for magneto-optical recording. The functionality of the films is tested by in-plane magnetic and polar Kerr effect measurements. The obtained figures of merits (in terms of Kerr rotation to absorption coefficient ratio) for the CoFe$_2$O$_4$ and CoFe$_2$O$_4$-SiO$_2$ thin films lie in a range that makes them promising for industrial magneto-optical recording and waveguide applications.

Results & Discussion

CoFe$_2$O$_4$ nanoparticles are obtained via a previously reported microwave assisted non-aqueous sol-gel synthesis.[142] The nanoparticles are post-functionalized with 2-[2-(2-methoxyethoxy)ethoxy]acetic acid (MEEAA) to obtain highly concentrated and stable nanoparticle dispersions in ethanol.[143] The silica nanoparticles are synthesized via an adapted Stöber method,[144] which directly yields concentrated and stable SiO$_2$ dispersions due to negative surface charges. The synthesis and thin film fabrication process are depicted schematically in Figure 3.1. For the nanocomposite thin films, colloidal CoFe$_2$O$_4$-SiO$_2$ dispersions are prepared in the range of 30-90 wt% SiO$_2$ (weight ratios in terms of particle content only, see Table 3.3) via mixing of the respective dispersions in the desired amount. Subsequently, CoFe$_2$O$_4$ and CoFe$_2$O$_4$-SiO$_2$ thin films are obtained via repeated spin coating-calcination cycles of the corresponding co-dispersions and finally sintering in air.
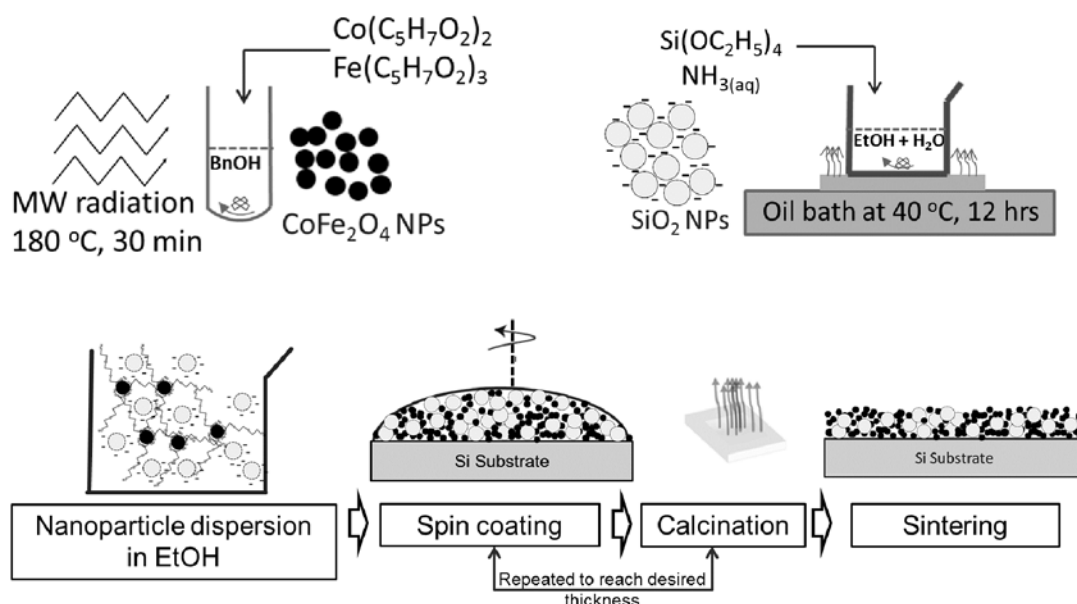
Figure 3.1 Illustration of the fabrication process for nanoparticle-based films. Nanoparticle (NP) synthesis: Use of microwaves (MW) and benzyl alcohol (BnOH) as solvent for CoFe$_2$O$_4$ and Stöber process in a mixture of ethanol (EtOH) and water for SiO$_2$. Film fabrication: Preparation of co-dispersion, followed by spin coating, calcination and sintering.

Structural characterization

Structural characterization of the CoFe$_2$O$_4$ nanoparticles and the sintered film of pure CoFe$_2$O$_4$ is performed by X-ray diffraction (XRD) and confocal Raman microscopy techniques. All reflections in the XRD pattern of both samples can be indexed to the cubic spinel phase, in agreement with the literature (Figure 3.2).[136] The crystal size, estimated from the Scherrer equation applied to the (311) reflection, is 5 nm for the nanoparticles and 19 nm for the sintered film.
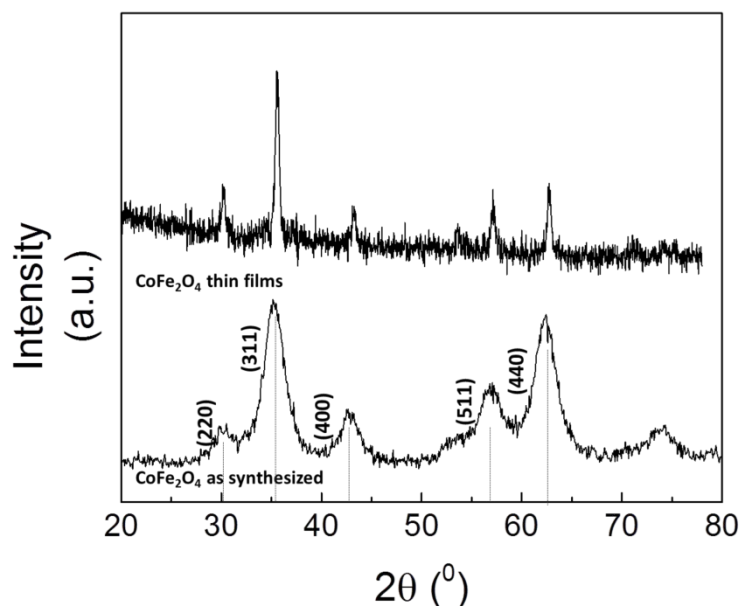
Figure 3.2 XRD patterns of the as synthesized CoFe$_2$O$_4$ nanoparticles and the sintered thin film.

XRD patterns of the nanocomposite thin films are displayed in Figure 3.3a. The XRD pattern of the composite film with 30 wt% SiO$_2$ is mainly dominated by the reflections from the CoFe$_2$O$_4$ phase, whereas for samples with a higher SiO$_2$ content the typical broad peak centered at 22 ° associated with an amorphous material starts to appear. With increasing SiO$_2$ content, also the CoFe$_2$O$_4$ reflections broaden. This observation points to a restricted crystal growth of the CoFe$_2$O$_4$ nanoparticles during sintering due to the space limiting effect of the silica framework and the restricted interparticle diffusion of the ions. However, the broad reflections make it difficult to completely exclude the formation of side phases such as maghemite (γ-Fe$_2$O$_3$). Thus, confocal Raman microscopy is employed in addition to XRD to confirm the chemical purity and to elucidate the near order characteristics of the single phase and nanocomposite thin films (Figure 3.3b). The Raman spectra exhibit four broad Raman modes at 330, 475, 610 and 695 cm^{-1}, all of which can be assigned to E$_g$, T$_{1g}$ and A$_{1g}$ vibrations belonging to the inverse cubic spinel structure.[145] The Raman spectra of the nanocomposite thin film samples are strongly dominated by CoFe$_2$O$_4$, which is reported in the literature for high CoFe$_2$O$_4$ concentrations,[146] and no chemical fingerprint from the SiO$_2$ phase is distinguishable up to 90 wt% SiO$_2$ (see Supporting Information, Figure S3.1). Even at 90 wt% SiO$_2$, only transverse optical (TO) modes due to asymmetric stretching vibrations of Si-O-Si could be observed. In any case, there is a low contribution from SiO$_2$ as a result of its vitreous nature and fluorescence.[147] The sharp Raman mode indicated with an asterisk is an artefact coming from the measurement setup and overlaps with the broad T$_{1g}$ vibration of the spinel ferrite. The absence of Raman modes at 300, 500 and 700 cm^{-1}, characteristic for γ-Fe$_2$O$_3$, confirms the chemical purity of the samples and indicates that the cubic inverse spinel structure of CoFe$_2$O$_4$ was maintained after sintering.[148]

a)

b)
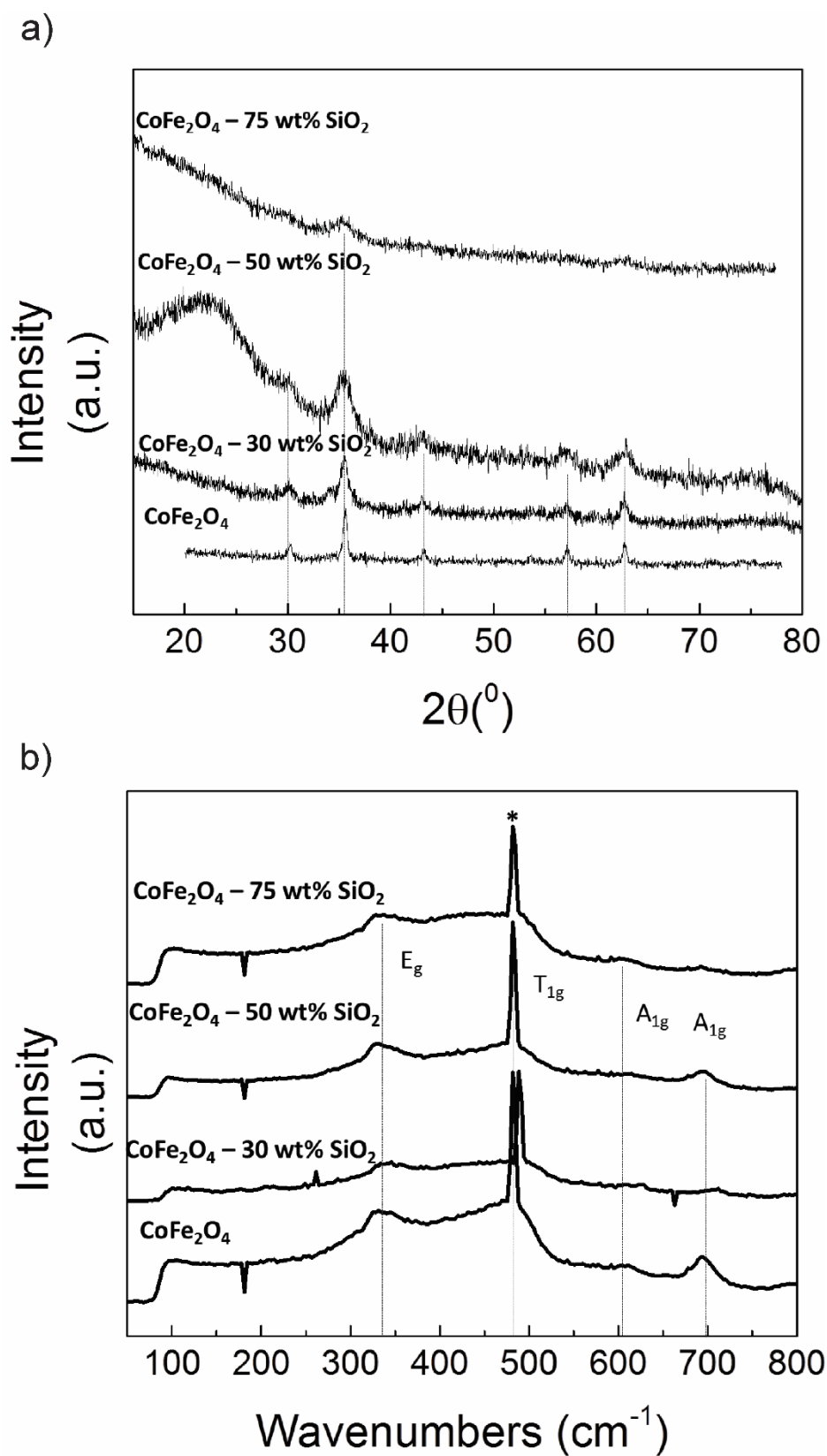
Figure 3.3 a) XRD patterns and b) Raman spectra of sintered CoFe$_2$O$_4$ and CoFe$_2$O$_4$-SiO$_2$ nanocomposite films with different SiO$_2$ concentrations. The dashed lines represent the Bragg reflections (a) and the Raman vibrations (b) of the inverted spinel CoFe$_2$O$_4$ phase.

Microstructural examinations of the thin film cross-sections

Scanning electron microscopy (SEM) examinations on thin film cross-sections reveal a crack free and porous structure in the CoFe$_2$O$_4$ as well as in the nanocomposite thin films (Figure 3.4a-e). For sintered CoFe$_2$O$_4$ thin films, thicknesses up to 1.2 μm can be reached (Figure 3.4b) via four successive spin coating-calcination cycles using dispersions with a concentration of approx. 120 mg/ml. By tuning the dispersion concentrations, the thickness per deposition cycle can be effectively controlled in the range of 100-400 nm, which is advantageous for possible embedding of these films in magnetic memory based devices or in microelectromechanical systems. For CoFe$_2$O$_4$-SiO$_2$ nanocomposite thin films, the thicknesses are between 480-600 nm as seen from cross-sectional SEM images in Figure 3.4c-e. They are obtained by one spin coating-calcination cycle using dispersions with 130 mg/ml CoFe$_2$O$_4$ and 50 mg/ml SiO$_2$ that are mixed in the appropriate ratios. AFM investigations showed that the roughness of the films is in the range of 10-30 nm, and can even be as low as only a few nm (Figure S3.2). The nanoparticulate structure of the films is maintained after sintering, facilitating the integration of these materials into magneto-optical systems with improved signal to noise ratio.
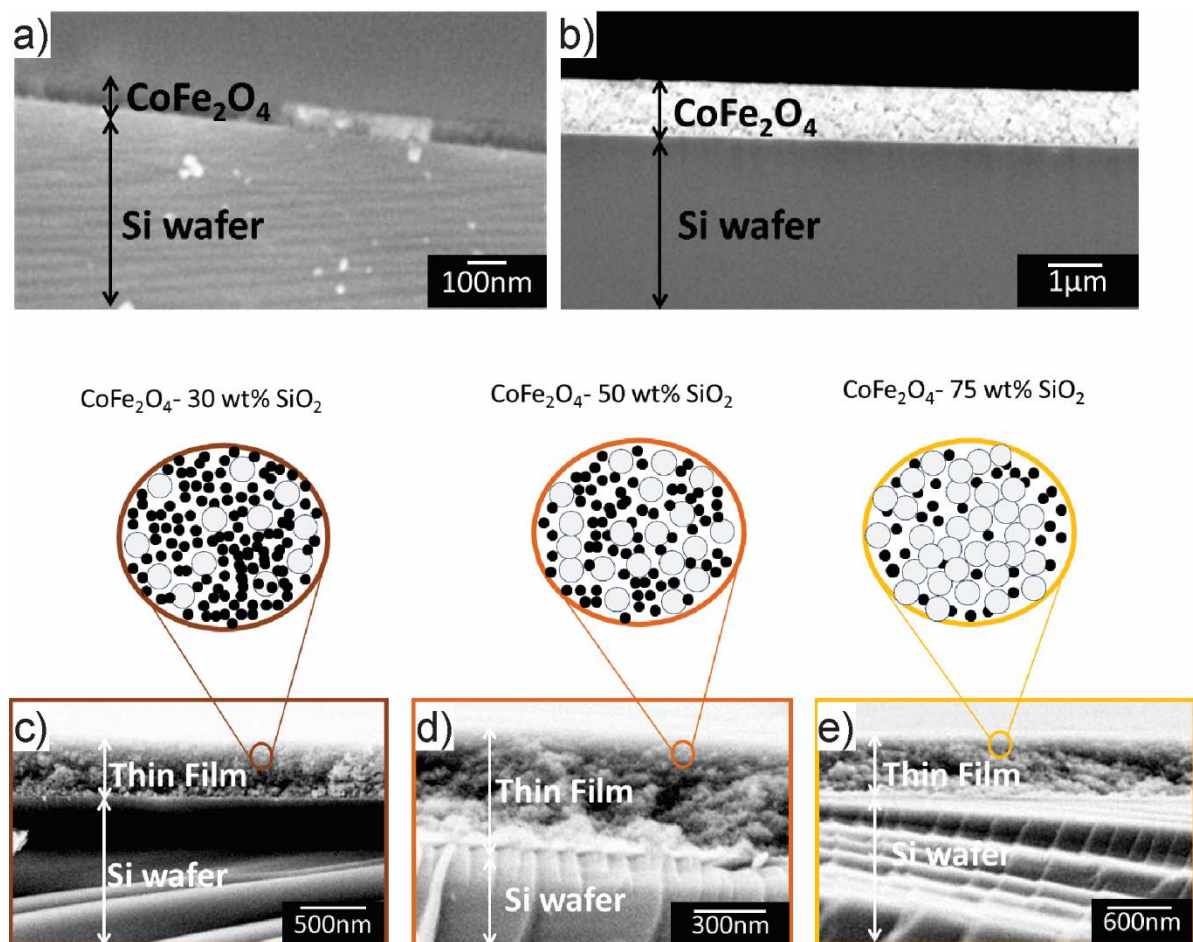
Figure 3.4 Cross-sectional SEM images of (a-b) CoFe$_2$O$_4$ and (c-e) CoFe$_2$O$_4$-SiO$_2$ nanocomposite thin films after sintering with thicknesses of a) 115 nm, b) 1.2 μm, c) 480 nm, d) 600 nm, and e) 680 nm. The compositions and structures of the CoFe$_2$O$_4$-SiO$_2$ films are schematically given above the images (c-e).

Optical properties

Optical characteristics of the different thin films are investigated by measuring their reflection and transmission spectra in the UV-*vis* range. Absorption spectra are obtained by subtracting the transmission from 100% (Figure 3.5a-b). Refractive indices are extracted from the reflectance spectra in the 300-500 nm range, corresponding to high and medium absorption regions[149] for samples up to 50 wt% SiO$_2$ content (absorption, A > 30 %). The equation $\alpha d = - \ln[(T/(1-R)]$ is used to calculate the absorption coefficient (α) of the samples.[150] Here, both transmittance (T) and diffuse reflectance spectra (R) are incorporated into the equation in order to account for the diffuse reflection losses from the sample surface associated with the nanoparticulate nature of the films with the thickness d. For UV-*vis* investigations, the same nanocomposite samples as shown in Figure 3.4c-e are used, having a thickness range of 480-600 nm. In the case of the CoFe$_2$O$_4$ thin films, a 100 nm thick sample is studied. Band gaps of the samples are calculated from the corresponding Tauc plots (Figure 3.5a-b). The absorption spectra of all samples exhibit low absorption (A < 30 %) in the range of ca. 600-800 nm. The absorption values obtained at 700 nm for the CoFe$_2$O$_4$-30 wt% SiO$_2$ and for the CoFe$_2$O$_4$-50 wt% SiO$_2$ nanocomposites are 17% and 6 %, respectively, while the CoFe$_2$O$_4$-75 wt% SiO$_2$ sample becomes fully transparent (0% absorption) at this wavelength (Figure 3.5b). For all three samples, a high absorption (A > 60 %) region is observed below 250 nm. The band gaps for direct and indirect transitions are calculated by extrapolation of the linear portions in the Tauc plots (see insets Figure 3.5a and 5b) and the direct band gap values are listed in Table 3.1.

Table 3.2 Direct and indirect bandgap values for CoFe$_2$O$_4$ and CoFe$_2$O$_4$-SiO$_2$ thin films

Sample	Direct Transition Bandgap (eV)	Indirect Transition Bandgap (eV)
CoFe$_2$O$_4$	2.6	1.4
CoFe$_2$O$_4$- 30 wt% SiO$_2$	3	1.3
CoFe$_2$O$_4$- 50 wt% SiO$_2$	3.1	1.6
CoFe$_2$O$_4$- 75 wt% SiO$_2$	3.9	3.05

The band gap values calculated for direct transitions lie in the UV-*vis* range, whereas the values for indirect transitions are in the near infrared (NIR) for up to 75 wt% SiO$_2$ content. In the latter case, one would expect a lower transmission in the sub-NIR wavelengths,

which is not the case for our system. Furthermore, the color of the CoFe$_2$O$_4$ sample is rather brown than black, in accordance with the band gap value in the UV-*vis* range,[151] since a band gap value in the NIR range would impose a black color. The direct bandgap of CoFe$_2$O$_4$ is 2.6 eV, which corresponds to the reported literature value for a direct bandgap transition.[151] For the nanocomposite samples, the band gap values are altered from 2.6 to 3.9 eV upon increase of the SiO$_2$ content from 30 to 70 wt%, implying a tunable transparency via SiO$_2$ addition (Table 3.1). Similarly, also a dependence of the absorption coefficients on the SiO$_2$ content is observed (Figure 3.6a). For the CoFe$_2$O$_4$ film, the maximum absorption coefficient is measured as $1.7 \cdot 10^5$ cm^{-1}, which is significantly lower than the absorption coefficient of epitaxially grown CoFe$_2$O$_4$ layers.[150] The reason for this difference can be attributed to diffuse scattering from the grain boundaries associated with the granularity of the films as well as the surface roughness in the range of 10 nm as a result of the spin coating process. With the addition of SiO$_2$, the absorption coefficients can be reduced drastically to a value of maximum $0.4 \cdot 10^5$ cm^{-1}. Minimum penetration depths are calculated from the maximum absorption coefficients (see Supporting Information, Table S3.1.), indicating that the absorption is measured from the top 67 nm in the case of pure CoFe$_2$O$_4$. With increasing amount of SiO$_2$, the layer thickness, from which the absorption is obtained, grows to 785 nm, in agreement with the bandgap and transparency measurements.

a)

b)
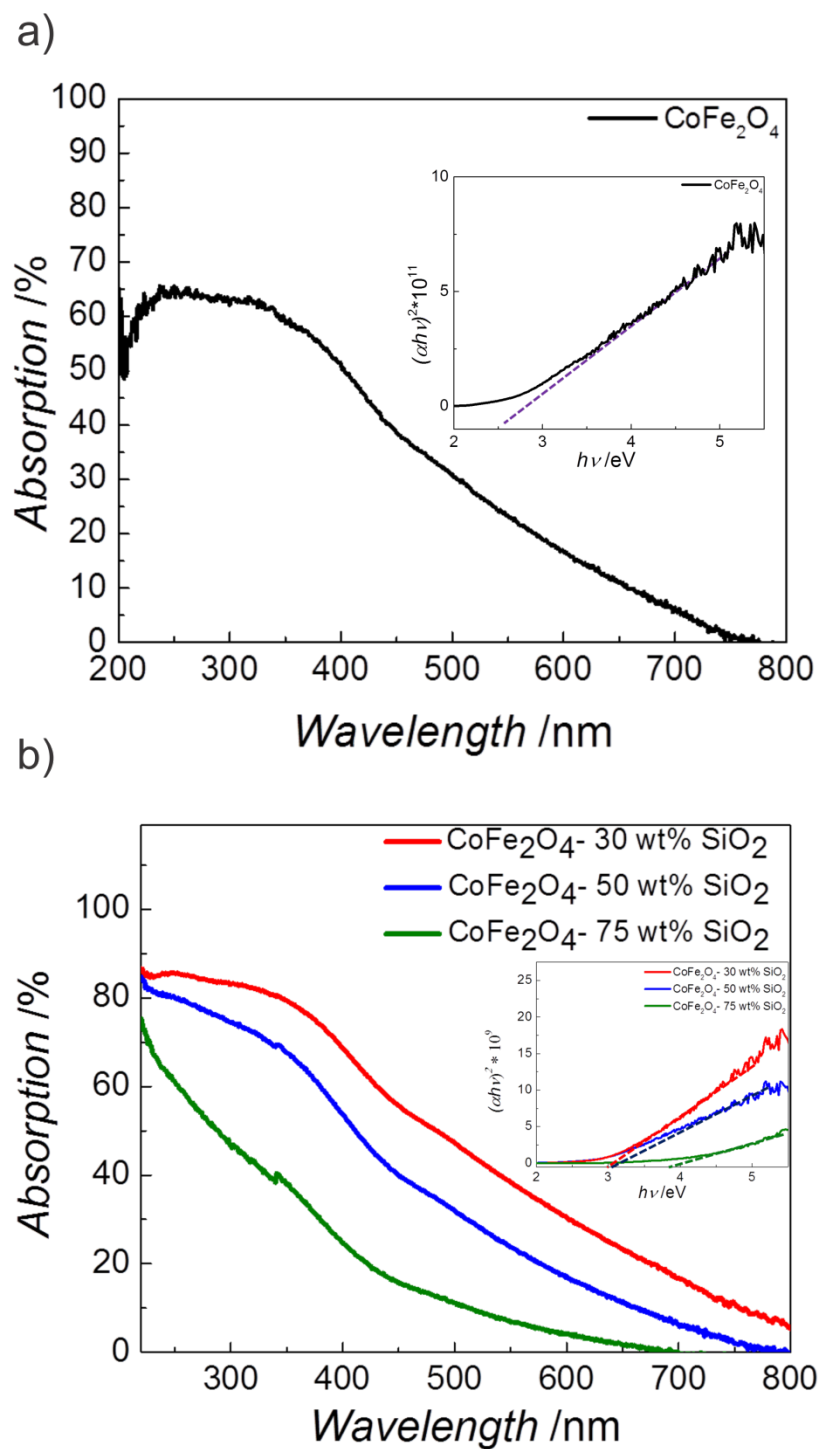
Figure 3.5 Absorption spectra and Tauc plots (insets) for the direct band gap transitions of a) CoFe$_2$O$_4$ and b) CoFe$_2$O$_4$-SiO$_2$ nanocomposite films.
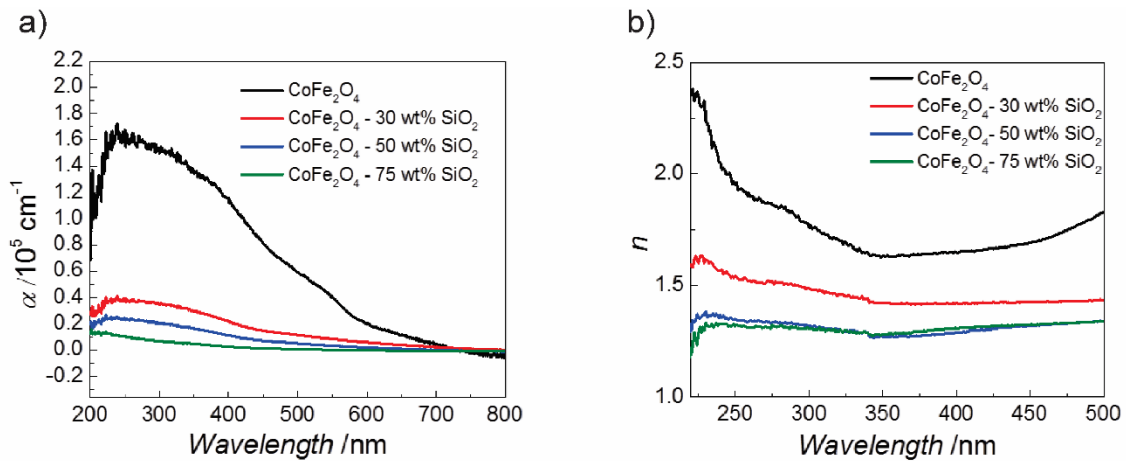
Figure 3.6 Absorption coefficient a) and refractive index spectra b) of CoFe$_2$O$_4$ and CoFe$_2$O$_4$-SiO$_2$ films.

The refractive index spectra of the single phase CoFe$_2$O$_4$ and the nanocomposites further reflect the effect of SiO$_2$ incorporation into the system (Figure 3.6b). The refractive index of the CoFe$_2$O$_4$ film has a maximum value of 2.3 at a wavelength of 235 nm, whereas this value shifts down to 1.6 for CoFe$_2$O$_4$-30 wt% SiO$_2$, which now is in the range to be suitable for integrated optics. Increase in the SiO$_2$ content to 50 wt% results in a refractive index of 1.3, and this value does not change significantly for a SiO$_2$ content of 75 wt%.

Magnetic characterization of the pure CoFe$_2$O$_4$ films

In-plane hysteresis curves and zero field cooled (ZFC) and field cooled (FC) curves are measured in order to investigate the macroscopic magnetic properties of the films. All magnetic measurements are performed on the 1.2 μm thick single phase CoFe$_2$O$_4$ sample. X-ray absorption spectroscopy (XAS) and X-ray magnetic circular dichroism (XMCD) measurements reveal the details of the cation distributions and elemental contributions to the magnetism. In-plane hysteresis measurements of magnetic properties indicate a superparamagnetic behavior in agreement with a sub 20 nm particle size (Figure 3.7a).[152] The measured magnetization at saturation, M$_s$, is 35 emu/g, which is in the reported range for nanoparticle CoFe$_2$O$_4$ films,[135] but lower than the bulk value of 80 emu/g.[153] Many factors contribute to a lowering in M$_s$ for nanocrystalline samples in comparison to the bulk, such as the difference in inversion parameters or the presence of a dead layer.[154] XAS and XMCD measurements give insights into the origins for the lower M$_s$, Figure 3.7b and Figure 3.7c. XAS taken at Co elemental edge results in three peaks at the L$_3$ edge at 778.8, 780 and 781.2 eV and in a broad peak centered at 795 eV at the L$_2$ edge, Figure 3.7b. The relative intensities of these peaks reveal the inversion parameter, which is defined as the fraction of divalent cations occupying the octahedral sites. It is known that both tetrahedral and octahedral Co^{2+} ions contribute to the intensity of the peaks at the 778.8 and 780 eV.[155] However, the intensity of the pre-edge peak at 778.8 eV is mainly caused by Co^{2+} ions at octahedral sites. Therefore, the ratio of the relative intensities of these peaks reflect the distribution of Co^{2+} ions to tetrahedral and octahedral sites.[155] A comparison of the relative peak heights in this study with the reported values shows that here we have an inversion parameter of around 70% (Figure S3.3).[156] It can be expected that the 30% of the octahedral sites, which are not occupied by the Co^{2+} ions, are filled with Fe^{+3} ions. This should increase the M$_s$ of the system, due to uncompensated antiferromagnetic coupling in the tetrahedral Fe^{3+} sites.[157] This hypothesis can be confirmed with the observation of a net XMCD signal at the Fe-L$_{3,2}$ edges as seen in Figure 3.7c, which demonstrates that Fe^{3+} ions

are also contributing to the magnetism. This is in contrast to the ideal picture of a fully inverted spinel structure, where magnetism is supposed to be only due to Co^{2+} ions.[158] As a result, the inversion parameter cannot explain the low M$_s$ of our system. From the ZFC curve (Figure 3.7d), a blocking temperature (T$_B$) of 240 K and a crossing temperature (T$_{cross}$) of 300 K, corresponding to the point where ZFC and FC curves coincide, are measured. The average particle size is extracted from T$_B$ via equation 8 and the magnetic anisotropy constant (K$_{eff}$) is empirically calculated from equation 9, while the maximum particle size is calculated inserting T$_{cross}$ into equation 8. According to this, the average particle size is found to be 6.2 nm and the size of the largest particles is 8 nm from T$_B$ and T$_{cross}$, respectively, indicating a narrow particle size distribution in the final CoFe$_2$O$_4$ films despite sintering.

$$K_{eff} \, V = 25 k_B \, T_B \text{[159]} \tag{8}$$

$$K_{eff} = 19.6 \cdot 10^6 \exp(-1.9 \cdot 10^{-5} \cdot T_B^2) \text{[160]} \tag{9}$$

While there are some discrepancies between the particle sizes calculated from the different methods, one has to keep in mind that the size values from XRD data refer to the crystal size, while the ZFC-FC measurements refer to the magnetic domain size. It is known in the literature that in the nanosized regime, magnetic dead layers are often formed on the surfaces of magnetic grains as a result of increased surface to volume ratios, which causes a reduction in M$_s$.[161] The presence of such a dead layer can originate from spin canting,[162] lack of crystallinity at the nanoparticle surface[161] or broken exchange coupling.[163] The thickness of the dead layer can be calculated via:

$$M = M_s(1-6t/d) \text{[164]} \tag{10}$$

where t denotes the dead layer thickness and d the particle size. A 0.6 nm dead layer exists, as illustrated in Figure 3.7e, giving rise to a reduced M$_s$. Considering the high crystallinity of our samples as deduced from XRD and Raman data, the presence of a dead layer presumably arises from the broken exchange coupling and spin canting.
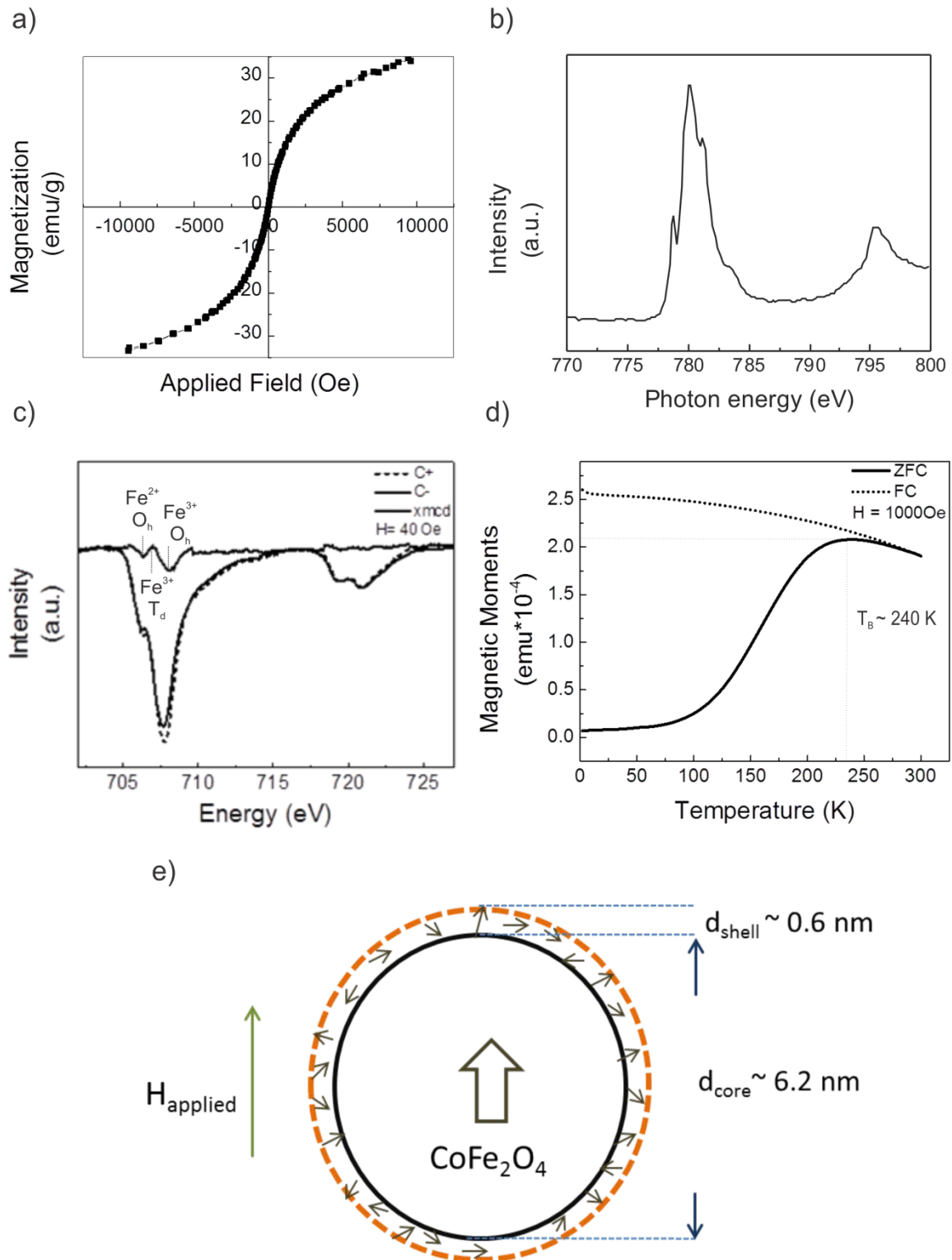
Figure 3.7 a) In-plane measurements of the magnetic properties, b) XAS at the Co edge, c) XAS and XMCD at the Fe edge, d) ZFC and FC curves (taken at 1000 Oe external field). The synchrotron measurements were performed on a sintered CoFe$_2$O$_4$ film with 200 nm thickness, while for the macroscopic magnetic measurements a 1.2 μm thick sample was used. e) Schematic drawing of a CoFe$_2$O$_4$ nanoparticle with its dead layer.

Magneto-optical properties of CoFe$_2$O$_4$ and CoFe$_2$O$_4$-SiO$_2$ films

Magneto-optical hysteresis curves are measured in order to obtain the polar Kerr rotations versus applied fields at a laser wavelength of 632 nm (Figure 3.8a). In contrast to the in-plane superparamagnetic properties, the single phase and the nanocomposite samples up to 50 wt% exhibit considerable hysteresis when the out-of-plane magnetic field is applied. As an example, longitudinal and polar Kerr rotation curves measured on CoFe$_2$O$_4$-30 wt% SiO$_2$ are given in Figure S3.4, which clearly demonstrate the existence of perpendicular magnetic anisotropy. There are two sources of anisotropy in magnetic systems: Magnetocrystalline and strain-induced anisotropy. Moreover, the stray fields associated with the boundaries of the magnetic structures can also result in a so-called "shape anisotropy". In our system, the proportion of boundaries result from the nanoparticle surfaces, which are nearly spherical and therefore isotropic as seen from SEM and AFM images. Thus, the formation of an easy axis for magnetization associated with the shape of the nanoparticle building blocks is unlikely to occur. Taking the randomly oriented nanoparticulate nature of our films into consideration, magnetocrystalline anisotropy is not expected either, which suggests strain-induced anisotropy to be the most plausible reason for the encountered considerable polar Kerr hysteresis loops perpendicular to the substrate.[152, 165] In-plane tensile stresses are known to be present under constrained sintering conditions associated with thin film geometries.[83] During sintering, shrinkage occurs in the films as a result of neck growth and compaction between the particles, and because the film is clamped to the substrate at the film-substrate interface, the substrate produces in-plane tensile stresses that counteract the isotropic shrinkage in the film associated with sintering,[83] as shown schematically in Figure 3.8b. Although these stresses are expected to relax after a certain film thickness, it was reported that they indeed can produce strain-induced magnetic anisotropy in porous magnetic thin film nanostructures of similar thicknesses.[152, 166] Therefore, we believe that in our system, strain-induced anisotropy as a result of the constrained sintering conditions is the most likely source of the observed perpendicular magnetic anisotropy. In-plane tensile stresses create an out of plane easy magnetization axis perpendicular to the substrate considering the negative magnetostriction of CoFe$_2$O$_4$.[152] The single phase CoFe$_2$O$_4$ and the CoFe$_2$O$_4$-30 wt% SiO$_2$ nanocomposite reach a maximum Kerr rotation of 7200 $^{\circ}$/cm and 6316 $^{\circ}$/cm, respectively, around 4000 Oe. The maximum Kerr rotation value for CoFe$_2$O$_4$-50 wt% SiO$_2$ drops to 2880 $^{\circ}$/cm, which is associated with the decrease in the content of the magnetic phase,[167] but still the material continues to exhibit a magneto-optical hysteresis loop. For 75 wt% SiO$_2$, the Kerr response decreases significantly, while the sample starts to display superparamagnetic characteristics, indicating a decrease in the interparticle magnetic interactions as a result of the dilution with SiO$_2$.
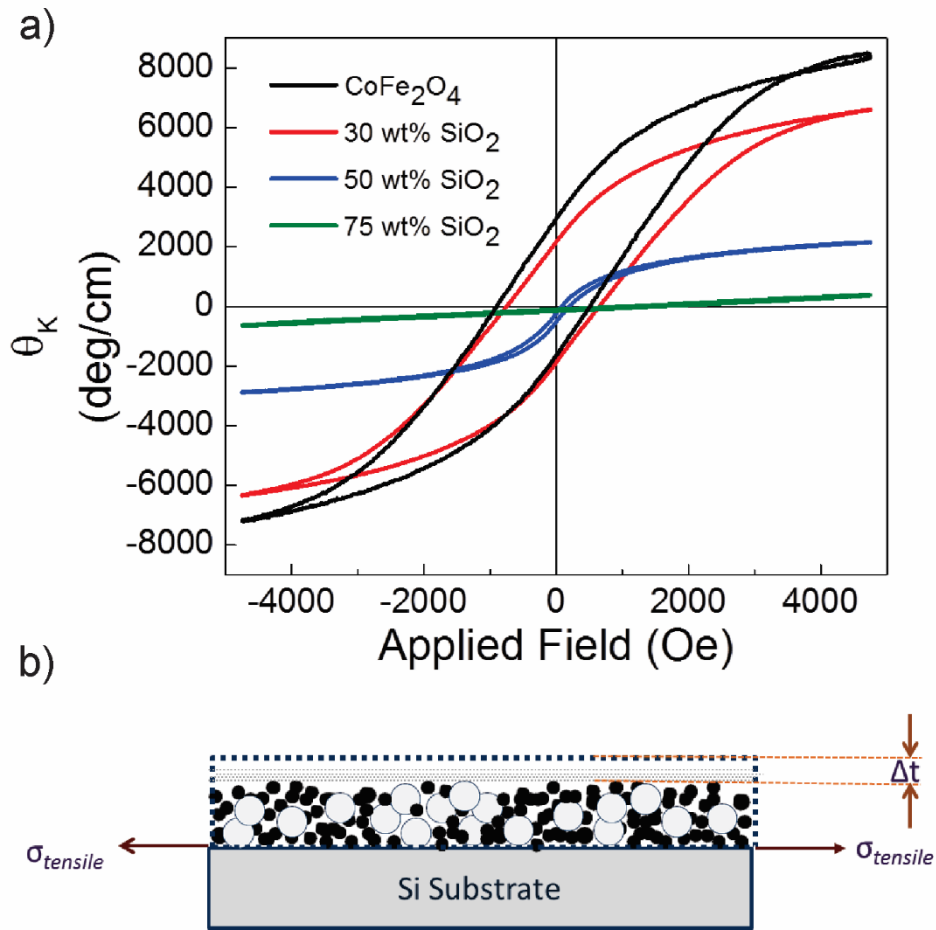
Figure 3.8 a) Polar Kerr loops of CoFe$_2$O$_4$ and CoFe$_2$O$_4$-SiO$_2$ nanocomposite thin films. b) Schematic drawings showing constrained sintering and associated in-plane tensile stresses and Δt represents the shrinkage along the thickness on sintering.

Table 3.3 Figure of merits for single phase & nanocomposite thin films

Sample	θ_K/α (deg)
CoFe$_2$O$_4$	0.46
CoFe$_2$O$_4$- 30 wt% SiO$_2$	1.25
CoFe$_2$O$_4$- 50 wt% SiO$_2$	1.93
CoFe$_2$O$_4$- 75 wt% SiO$_2$	Divergent

The presence of a spontaneous Kerr rotation up to 50 wt% SiO$_2$ enables the use of these materials for magneto-optical recording as well as for integrated magneto-optical devices without application of an external field. Figures of merit of the materials are calculated via θ_K/α, where θ_K is the Kerr rotation and α the absorption coefficient. The θ_K/α values for the single phase and nanocomposite samples (Table 3.2) indicate an increase with increasing SiO$_2$ content due to drastic decrease in absorption coefficients. For all cases, the figures of merit lie in the desired range for device applications,[168] whereas the most suitable system seems to be CoFe$_2$O$_4$-30 wt% SiO$_2$, considering its attractive magneto-optical properties and spontaneous Kerr response, suitable refractive index (1.5) and lower absorption coefficient.

Conclusion

In this study, the liquid phase deposition of thin films from preformed nanoparticles is presented as a powerful approach to design multifunctional nanocomposite films over a wide compositional range with carefully tailored properties. Based on the system of CoFe$_2$O$_4$-SiO$_2$, we demonstrate that nanocomposite thin films with systematically tuned optical properties and desired magnetic and magneto-optical properties can be produced in an efficient and cost effective way through spin coating of the corresponding nanoparticle dispersions. Owing to the defined nature of the preformed nanoparticles as building blocks, full control over structural parameters such as composition, crystallinity, and phase evolution can be maintained in the final films, which is essential to achieve the desired magnetic and magneto-optical functionalities. In addition, in-plane stresses arising from constrained sintering conditions induce perpendicular magnetic anisotropy. The refractive index, absorption coefficient and the transparency range of the nanocomposites can be effectively tuned by the SiO$_2$ content without losing the spontaneous magneto-optical Kerr rotation, enabling the future use of these materials for perpendicular magnetic and magneto-optical recording applications, as well as for magneto-optical waveguides for transverse waves in integrated optics.

Experimental Procedure
Materials

Cobalt and iron acetylacetonate (Co(C$_5$H$_7$O$_2$)$_2$, > 97 %, Fe(C$_5$H$_7$O$_2$)$_3$, > 99.8%), anhydrous benzyl alcohol (> 99.8%), tetraethoxysilane (Si(OC$_2$H$_5$)$_4$, > 98%), NH$_{3(aq)}$ (25%), acetone (> 99.5%), isopropanol (> 99.8%) and 2-[2-(2-methoxyethoxy)ethoxy]acetic acid (MEEAA, technical grade) are all purchased from Sigma-Aldrich and used without further purification. Absolute ethanol is obtained from Fluka. <100> oriented p-type Si wafers (Semiconductor Wafer Inc, Taiwan), fused SiO$_2$ (MTI Corp, USA) and fused quartz (UQG Optics, England) substrates are used for thin film deposition. The substrates are sonicated in acetone and isopropanol for 5 minutes each prior to film deposition.

Synthesis & dispersion of nanoparticles

For the synthesis of CoFe$_2$O$_4$ nanoparticles, a previously published protocol is adapted.[136] Co(C$_5$H$_7$O$_2$)$_2$ and Fe(C$_5$H$_7$O$_2$)$_3$ are used as precursors and anhydrous benzyl alcohol as solvent without further purification. All chemicals are stored under inert atmosphere. In a typical synthesis, 353 mg Fe(C$_5$H$_7$O$_2$)$_3$ and 120 mg of Co(C$_5$H$_7$O$_2$)$_2$ were mixed with 5 ml of benzyl alcohol in an argon filled glovebox and subjected to microwave radiation at 180 ^{o}C for 30 minutes in a 10 ml Teflon capped glass vessel using a CEM Discover microwave reactor operating at 2.45 GHz. The CoFe$_2$O$_4$ nanoparticles were centrifuged off from the reaction solution at 4000 rpm, and washed twice in ethanol via centrifugation.

Subsequently, the nanoparticles were sonicated in 5 ml of a 0.3 M MEEAA-ethanol mixture and stirred overnight to ensure enough binding of the stabilizing agent to the nanoparticle surface. Then, this mixture was centrifuged off in excess hexane (5:1 hexane to ethanol ratio) to remove excess stabilizer. Finally, the washed nanoparticles were resonicated in ethanol in a concentration range from 30-130 mg/ml. For the SiO$_2$ nanoparticle synthesis, the Stoeber synthesis was adapted according to a previously published protocol.[169] Typically, 50 ml of absolute ethanol, 1 ml millipore water, and 1 ml of aqueous ammonia solution (25 %) were mixed and heated to 40 ^{o}C using an oil bath. Afterwards, 3 ml of Si(OC$_2$H$_5$)$_4$ was dropwise added under continuous stirring. This step was followed by addition of 2 ml Si(OC$_2$H$_5$)$_4$ in 3 hours intervals. After a total synthesis time of 12 hours, the heating was stopped and the mixture was cooled to room temperature. The resultant nanoparticle dispersions were used without any further treatment. This procedure yielded highly concentrated (between 20-50 mg/ml) SiO$_2$ nanoparticles of approx. 20 nm size. To determine the concentrations of the dispersions, 100 µl of each dispersion was dropped into a vessel of known weight and placed into an oven at 60 ^{o}C overnight. The weight was re-measured after evaporation of the solvent. For the size determination of the SiO$_2$ nanoparticles, the dispersions were diluted in ethanol and analyzed by dynamic light scattering using a Malvern ZetaSizer performing a 173 $^\circ$ backscatter measurement with three repeated runs.

Thin film fabrication

The co-dispersions of CoFe$_2$O$_4$-SiO$_2$ are prepared by mixing the dispersions of the individual components to yield 30, 50, 75 and 90 wt% of SiO$_2$, as shown in Table 3.3. After mixing, the co-dispersions are sonicated for 10 min and magnetically stirred for another 3-5 minutes. Afterwards, both single phase CoFe$_2$O$_4$ and nanocomposite CoFe$_2$O$_4$-SiO$_2$ nanoparticle thin films are fabricated using cycles of spin coating-calcination at 500 ^{o}C on a hot plate heated to the calcination temperature at a rate of 25 ^{o}C/min. For the spin coating, a maximum spinning speed of 1000 rpms in a total spinning period of 20 seconds using a Laurell WS650 spin coaters is employed. All film deposition processes prior to sintering are carried out in a laminar flow controlled synthetic air filled glovebox. Sintering in air at 700 ^{o}C for 2 hours with 4 hours of ramping rate for compaction is done in a Nabertherm L 3/11/B170 laboratory muffle furnace to finalize the film fabrication process.

Characterization

SEM images of the thin films deposited on Si wafers are captured at an operation voltage of 3-5 kV using a LEO 1530 (Germany) scanning electron microscope. Powder XRD patterns are obtained from a Panalytical X'Pert Pro diffactometer with Cu Kα source and monochromator in focusing geometry. Thin film XRD patterns are obtained using thin film optics (Goebbels mirror on the incident side and parallel plate collimator on the diffracted side) in grazing incidence geometry. To investigate the near order characteristics on thin films and nanoparticles, WITec CRM200 Confocal Raman Microscope (WITec, Germany) with a green laser of 532 nm is employed. UV-*vis* spectra are recorded with a JASCO V-770 spectrophotometer with an integrating sphere accessory (ILN-725) with background and substrate correction. Magnetic properties are measured using a superconducting quantum interference design (SQUID) magnetometer MPMS 5S, from Quantum Design, and ZFC and FC curves are measured in an external field of 1000 Oe. Magneto-optical characteristics are investigated using NanoMOKE 2 in polar Kerr geometry and a laser wavelength of 632 nm. XAS and XMCD spectra of the samples are obtained using Photoemission Electron Microscope (PEEM) and Scanning Transmission X-ray Microscope

at the NanoXAS beamline, Swiss Light Source, Villigen, Switzerland. The spectra are taken with opposite X-ray photon helicities with 0.1 eV step size at an applied magnetic field of 40 Oe. *XMCD* is calculated by (C$^+$-C$^-$), where C$^+$ and C$^-$ are right and left circularly polarized X-rays.

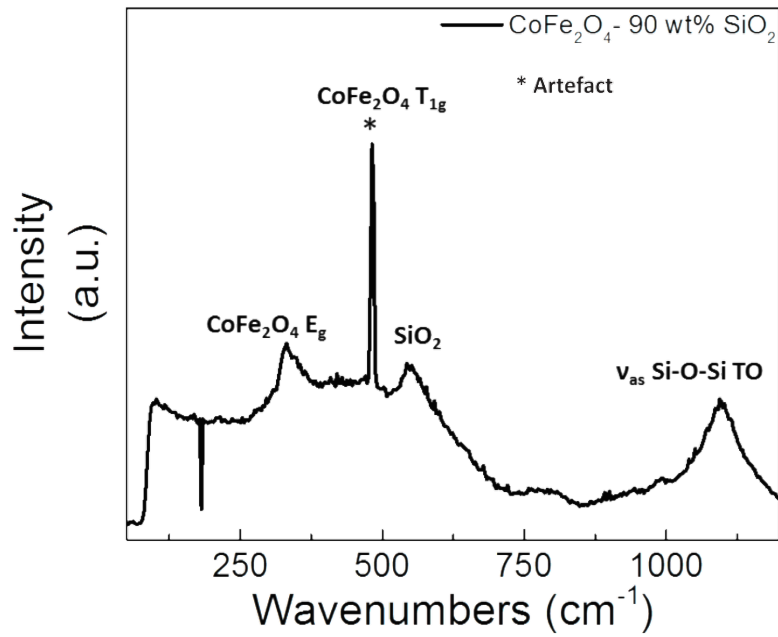**Table 4.3** Mixing ratio of CoFe$_2$O$_4$-SiO$_2$ dispersions

Samples	CoFe$_2$O$_4$ (130 mg/ml)	SiO$_2$ (50 mg/ml)
CoFe$_2$O$_4$-30wt%SiO$_2$	1 ml	1 ml
CoFe$_2$O$_4$-50wt%SiO$_2$	0.4 ml	1 ml
CoFe$_2$O$_4$-75wt%SiO$_2$	0.16 ml	1.2 ml
CoFe$_2$O$_4$-90wt%SiO$_2$	0.04 ml	1 ml

Acknowledgements

Supporting Information

Figure S3.1 Raman spectrum of the CoFe$_2$O$_4$-90 wt% SiO$_2$ film after sintering.
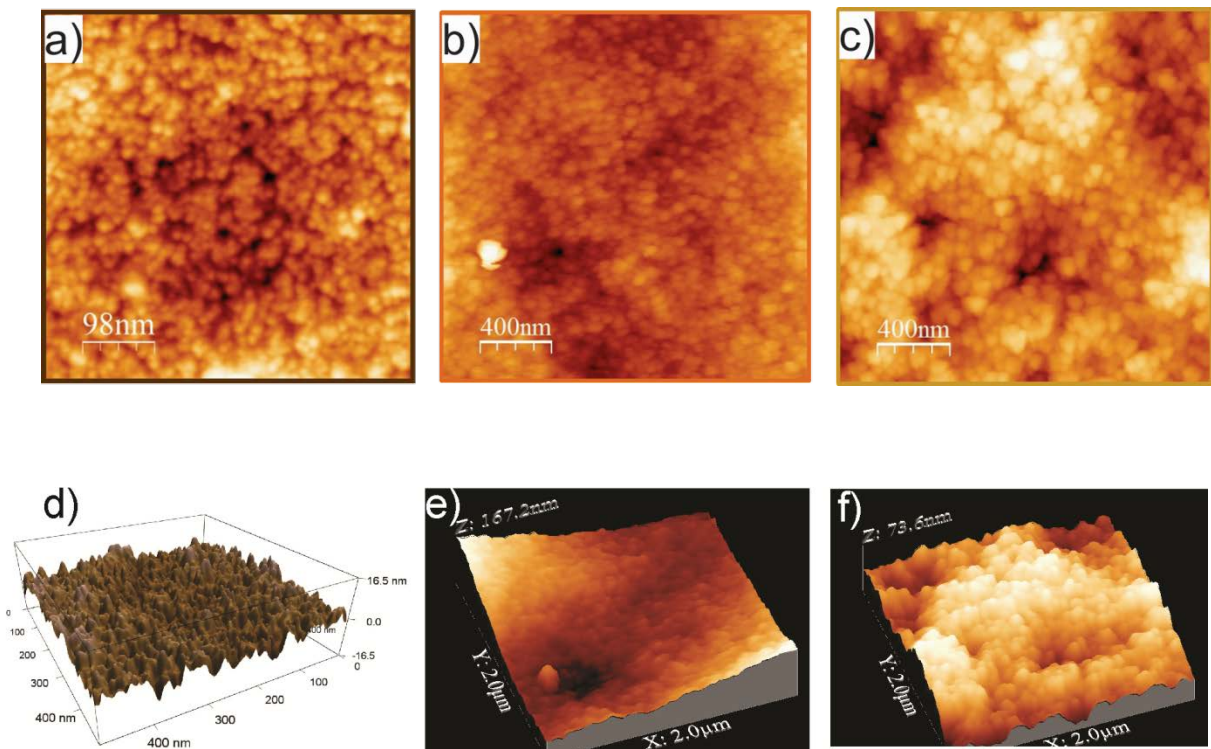
Figure S3.2 Height retrace topography images of the a) 1.2 μm thick CoFe$_2$O$_4$, b) 600 nm CoFe$_2$O$_4$-50 wt% SiO$_2$, and c) 680 nm CoFe$_2$O$_4$-75 wt% SiO$_2$ and 3-D views of d) 1.2 μm thick CoFe$_2$O$_4$, e) CoFe$_2$O$_4$-50 wt% SiO$_2$ f) 680 nm CoFe$_2$O$_4$-75 wt% SiO$_2$ thin film samples obtained by atomic force microscopy.

Table S3.1 Minimum penetration depths (δ_{min}) of the CoFe$_2$O$_4$ based nanocomposite film samples

Sample	δ_{min}
CoFe$_2$O$_4$	66 nm
CoFe$_2$O$_4$- 30 wt% SiO$_2$	250 nm
CoFe$_2$O$_4$- 50 wt% SiO$_2$	400 nm
CoFe$_2$O$_4$- 75 wt% SiO$_2$	785 nm
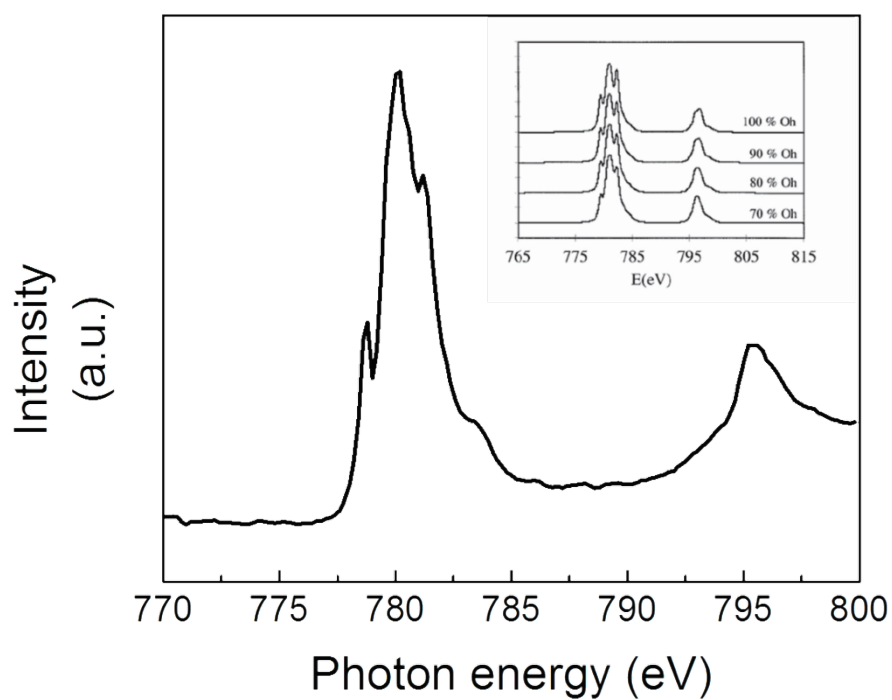
Figure S3.3 XAS at Co edge in comparison with spectra from literature[156] of cobalt ferrites with different inversion parameters.
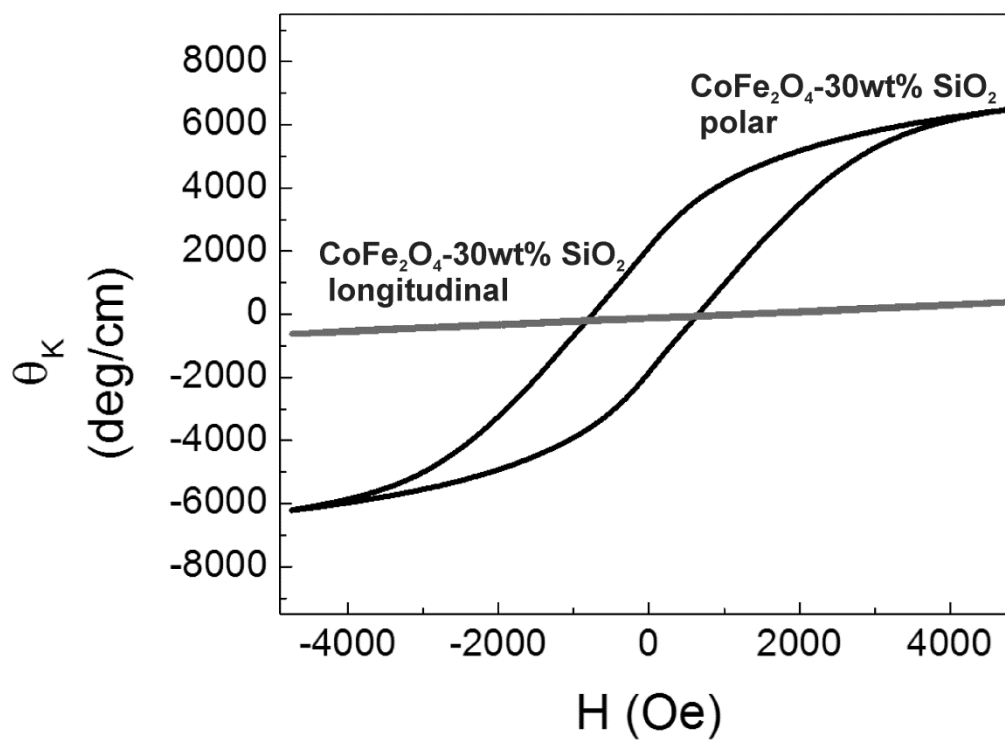
Figure S3.4 Longitudinal and polar Kerr rotation loops measured on CoFe$_2$O$_4$-30 wt% SiO$_2$ nanocomposite thin film sample indicating a clear perpendicular magnetic anisotropy.

4. BaTiO$_3$-CoFe$_2$O$_4$ magnetoelectric heterostructures for voltage control of magnetism

In this chapter, nanoparticle based thin film deposition approach will be used to create state-of-the-art complex heterostructures for emergence of otherwise non-existing functionalities, i.e. coupling between electric and magnetic degrees of freedom of thin film materials. The flexibility of the approach is demonstrated through genesis of nanocomposites of two different connectivity schemes, namely multilayered and co-dispersed composite geometries. The results shown here are taken from the manuscript "Nanoparticle-based magnetoelectric BaTiO$_3$-CoFe$_2$O$_4$ thin film heterostructures for voltage control of magnetism", from Derya Erdem, Nicholas S. Bingham, Florian J. Heiligtag, Nicolas Pilet, Peter Warnicke, Carlos A.F. Vaz, Yanuo Shi, Jennifer L.M. Rupp, Laura J. Heyderman, Markus Niederberger, which will be submitted to ACS Nano.

Abstract

Multiferroic composite materials combining ferroelectric and ferromagnetic order at room temperature have great potential in emerging applications such as four state memories, magnetoelectric sensors and microwave devices. In this paper, we report an effective and facile liquid phase deposition route to multiferroic composite thin films involving the spin-coating of nanoparticle dispersions of BaTiO$_3$, a well-known ferroelectric, and CoFe$_2$O$_4$, a highly magnetostrictive material. This approach offers great flexibility in terms of accessible film configurations (co-dispersed as well as layered films), thicknesses (from hundred nm to several µm) and compositional variety (5-50 wt% CoFe$_2$O$_4$ with respect to BaTiO$_3$) to address the different potential applications. A detailed structural characterization proves that BaTiO$_3$ and CoFe$_2$O$_4$ remain phase-separated with clear interfaces on the nanoscale after heat treatment, while electrical and magnetic studies indicate the simultaneous presence of both ferroelectric and ferromagnetic order. Furthermore, coupling between these orders within the films is demonstrated as voltage control of magnetism at ambient temperatures.

Introduction

The next generation memory devices impose new challenges to the existing materials' solutions for energy efficient, reliable, fast and sizeable transfer of data. Conventional memory applications such as magnetic random access memories (MRAM) employ ferromagnetic materials for data writing via switching of the magnetization states of the material. However, there are issues related to this technology such as high energy consumption, slow writing speeds and overheating due to high amounts of currents required to generate the magnetic fields.[170] Ferroelectric random access memory (FeRAM) devices offer faster writing speeds via switching of electrical polarization states of the material.[171] But in this case, slower reading rates linked to destructive read operations and size ability problems limit the further use of this technology.[172] In this respect, multiferroic materials exhibiting ferroelectric and ferromagnetic orders are suitable candidates for novel memory devices, because they offer a combination of advantages related to FeRAM and MRAM technologies enabling heterogeneous read-write operations.[173],[174] Particularly interesting for size miniaturization and lowered power consumption in these devices is the voltage control of magnetism.[175] In addition, application fields of such kind of multiferroics can be potentially extended to microwave devices, sensors, transducers, actuators and switches.[176, 177] Single phase multiferroic materials are scarce due to the physics restricting the presence of both ferroelectric and ferromagnetic order.[178] The few existing examples display only limited magnetoelectric coupling at low temperatures.[179] In comparison to single phase

multiferroics, composite materials exhibiting indirect magnetoelectric effect offer 3-5 order of magnitude greater coupling between electric and magnetic orders at ambient temperatures.[177] Such composites consist of a piezoelectric and a magnetostrictive constituent, and the coupling between different ferroic orders arise as a result of strain transfer at the phase boundaries.[71] Therefore, a high interfacial area between the two constituents is required to maximize the strain transfer. Nanocomposites composed of a mixture of these two components in various configuration schemes at the nanoscale are an attractive route towards room temperature multiferroics.[180] Several studies appeared in the literature reporting the preparation of composites via traditional solid state reactions,[181] electrospinning,[182] vacuum based deposition of composite thin films and sol-gel routes.[183] Thin film composite structures are particularly suitable and promising for device implementation.[184] Vacuum based deposition methods were found to produce multiferroic thin films of respectable magnetoelectric coupling, enabling the realization of complicated microstructures including epitaxy, texture, or columnar distribution of magnetic nanopillars in the ferroelectric matrix. However, there are problems related to crystallinity and stoichiometry of the phases as a result of the complex process, and the manufacturing costs associated with these methods are high.[79, 93, 185] Sol-gel routes to thin films transcend the gas phase deposition methods in terms of processing costs and deposition rates. Still, processing issues such as formation of side phases, difficulty in stoichiometry, film thickness control, or lack of crystallinity are associated with this technique.[186] Utilizing dispersions of preformed and well-defined nanoparticles to deposit multiferroic thin films would be able to circumvent many of these typical problems. Nevertheless, nanoparticle-based liquid phase deposition of multiferroic composites remained a challenge until now due to the difficulties linked to the implementation of this process for functional applications, such as cracks, roughness and failure in exhibiting the desired functionality.[86, 141] In fact, there are only few reports on colloidal deposition of functional thin films using SiO$_2$, TiO$_2$, SnO$_2$ and BaTiO$_3$ nanoparticles, which involve films of desired characteristics to be implemented into devices or already implemented into devices.[29, 31-34]

In this paper we show that owing to the predefined nature of nanoparticles, crack free multiferroic thin films in different composite geometries can be processed in an efficient and fast way over a wide range of thicknesses and compositions. Moreover, owing to full control over phase and stoichiometry, evolution of any interdiffusion or tertiary phases is avoided, which provides direct contact between the piezoelectric and magnetostrictive phase. As a proof of concept, we deposit two configurations of multiferroic nanocomposite thin films on various substrates: i) Alternating stacks of piezoelectric and magnetostrictive layers and ii) dispersion of one constituent into the matrix of the other. The ferroelectric constituent was chosen as BaTiO$_3$ due to its lead free composition and attractive piezoelectric properties,[187] and CoFe$_2$O$_4$ serves as the magnetic phase because of its high magnetostriction.[188] We show that the thin film composites can be deposited without the formation of cracks, delamination, or formation of any side phases between BaTiO$_3$ and CoFe$_2$O$_4$ using a nanoparticle-based liquid phase deposition approach. Electrical and magnetic measurements as well as element specific synchrotron studies performed on the co-dispersed nanocomposite samples gave evidence for a significant coupling between the electrical order of BaTiO$_3$ and the magnetic order of CoFe$_2$O$_4$ at ambient temperatures.

Results & Discussion
Structural Characterization

The BaTiO$_3$ and CoFe$_2$O$_4$ nanoparticles were synthesized using microwave-assisted nonaqueous sol-gel chemistry in acetophenone and in benzyl alcohol, respectively. The as-synthesized BaTiO$_3$ nanoparticles have a crystal size of approx. 13 nm, which is large enough to exhibit ferroelectric properties,[141] while the CoFe$_2$O$_4$ nanoparticles are 8 nm. Both types of nanoparticles were functionalized with 2-[2-(2-methoxyethoxy)ethoxy]acetic acid (MEEAA) and re-dispersed in ethanol.[109] For the composites with 0-3 configuration, co-dispersions of BaTiO$_3$ and CoFe$_2$O$_4$ were prepared by mixing the individual dispersions in the desired ratios, followed by deposition of thin films via spin coating and calcination cycles. For the multilayered composites of 2-2 connectivity, sequential stacks of BaTiO$_3$ and CoFe$_2$O$_4$ were prepared via spin coating of the individual nanoparticle dispersions with an intermediate calcination step at 500 °C. For the co-dispersed as well as for the multilayered composites, the film fabrication process is concluded by a final sintering step at 700 °C in air (for details see Experimental). Figure 4.1 displays the X-ray diffraction (XRD) patterns of the co-dispersed BaTiO$_3$-CoFe$_2$O$_4$ films of 400-500 nm thickness and with a CoFe$_2$O$_4$ content of 5-50 wt%. In the samples containing 5 and 10 wt% CoFe$_2$O$_4$, only reflections from the pseudo-cubic BaTiO$_3$ phase could be identified without any traces of crystalline by-products such as BaCO$_3$.[99] The tetragonality of the BaTiO3 phase, which is essential for the presence of ferroelectric order, could not be confirmed by XRD due to the peak broadening associated with sub-20 nm size of BaTiO$_3$.[101] In order to confirm the tetragonality, X-ray absorption spectra (XAS) at the Ti-edge were acquired (see Supporting Information Figure S4.1). XAS at the Ti edge in cubic crystal symmetry is known to exhibit only two absorption peaks, whereas the tetragonal symmetry displays four peaks corresponding to an additional splitting of the t$_{2g}$ and e$_g$ orbitals with a z-component due to off-centering of Ti^{4+} in the tetragonal symmetry (see Supporting Information, Figure S4.1).[23] The chemical fingerprints of the CoFe$_2$O$_4$ phase start to appear for the 25 and 50 wt% CoFe$_2$O$_4$ samples in the form of the most intense peak of the CoFe$_2$O$_4$ phase, namely the (311) reflection.[136] The full width at half maximum (FWHM) values of the most intense reflections for BaTiO$_3$ are listed in order to evaluate the effect of the relative ratios of both types of particles on the crystal sizes (see Supporting Information, Table S4.1). The FWHM values of BaTiO$_3$ nanocrystals increase with the CoFe$_2$O$_4$ content. This points out to a refinement on the grain size when the interfacial area between two phases increases. Considering the fact that all composites are produced starting from the same nanoparticle dispersions having the same average crystallite sizes, this observation can be explained on a restricted grain growth during sintering; since the available particle contacts of both phases decrease, restraining the grain growth.
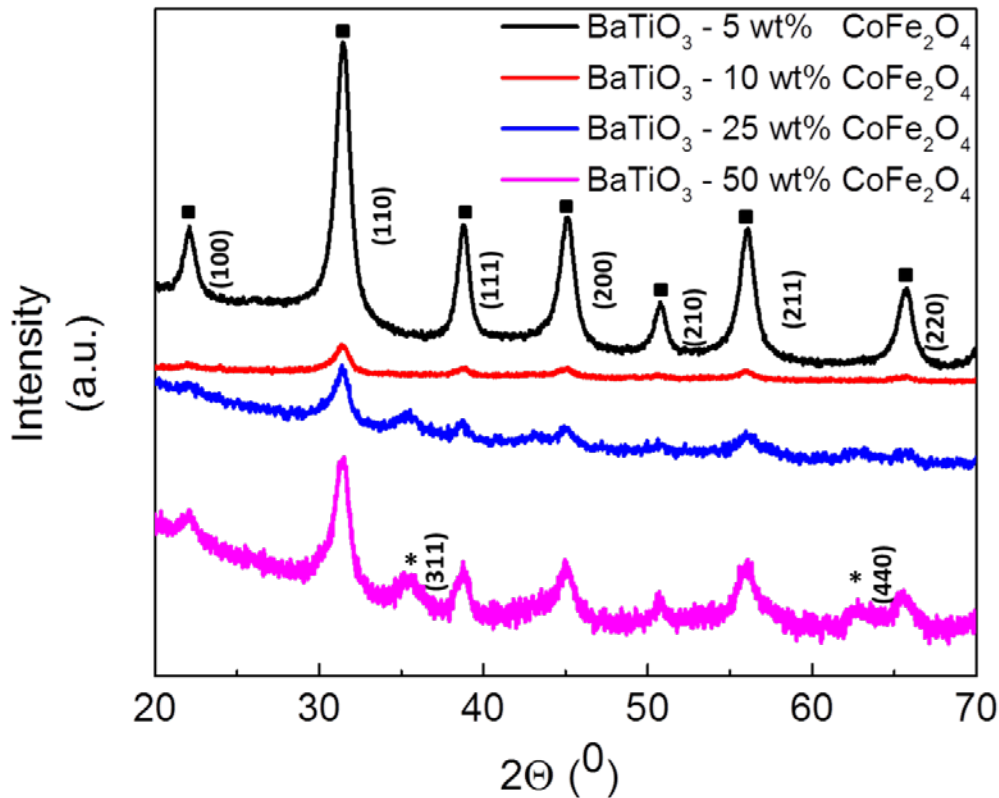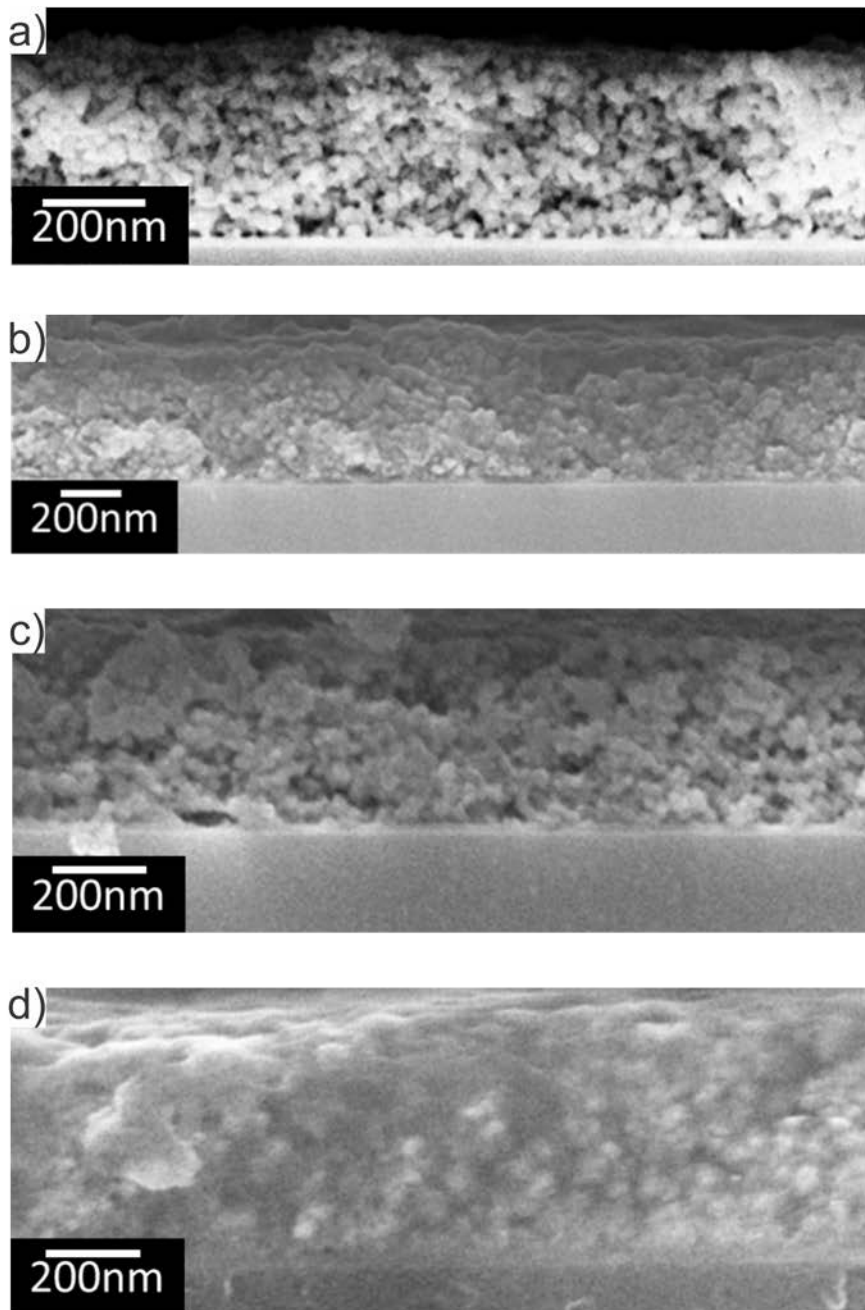
Figure 4.1 XRD patterns of BaTiO$_3$-CoFe$_2$O$_4$ co-dispersed composite thin films with thicknesses of 400-500 nm and 5-50 wt% CoFe$_2$O$_4$ content. The reflections marked with a filled square denote the BaTiO$_3$ phase and the reflections marked with an asterisk originate from the CoFe$_2$O$_4$ phase.

Microstructural Characterization

The microstructural characterizations on the co-dispersed and multilayered BaTiO$_3$-CoFe$_2$O$_4$ composites are carried out on thin film cross-sections, which are prepared by cleaving the substrate. The cross-sectional scanning electron microscopy (SEM) images of the co-dispersed composite thin films with 5-50 wt% CoFe$_2$O$_4$ are shown in Figure 4.2a-d. The samples are produced via one cycle of spin coating-500 $^{\circ}$C calcination using premixed nanoparticle dispersions of 100 mg/ml concentration, followed by one final 700 $^{\circ}$C sintering step in air. The thickness is in the range of 400-500 nm for all samples. Furthermore, SEM cross-sections revealed the formation of crack-free, well adhered thin films without large agglomerates. Focused ion beam (FIB) tomography is applied on the 5 and 50 wt% co-dispersed samples to gain insight to the residual porosity in the films after sintering. The analysis results on FIB-sections reveal between 30-50 % residual porosity in the final films (see Supporting Information, Figure S4.2.). Furthermore as-a-proof of concept, the nanoparticle dispersions are used to fabricate multilayered assemblies of BaTiO$_3$-CoFe$_2$O$_4$ thin films in a wide thickness range from 100 nm to 1.5 μm (see Supporting Information, Figure S4.3 a-b, and Figure 4.3e).

Scanning transmission electron microscopy (STEM) combined with energy dispersive X-ray (EDX) analysis is applied to reveal the degree of mixing of the BaTiO$_3$ and CoFe$_2$O$_4$

nanoparticles in the co-dispersed composites and to study the interfaces between the two types of nanoparticles at the end of the sintering process (Figure 4.3a-e).


Figure 4.2 Cross-sectional SEM images of BaTiO$_3$-CoFe$_2$O$_4$ co-dispersed samples containing a) 5 wt% b) 10 wt% c) 25 wt% d) 50 wt% CoFe$_2$O$_4$ displaying a crack-free and homogenous structure in the thin films after sintering.

In Figure 4.3a, an overview STEM image and in Figure 4.3b and 4.3.c, the chemical maps reflecting the distributions of Ti, Fe and Co taken on the overview image can be seen in the co-dispersed sample with 5 wt% CoFe$_2$O$_4$. As expected, the elemental distribution map is dominated by Ti due to its higher content in these films. Moreover, the elemental distribution maps of Co and Fe correspond spatially to each other, confirming the formation of CoFe$_2$O$_4$. Interplanar spacings of the nanoparticles are extracted from the Fast Fourier Transform (FFT) in the area, where Ti-Fe elemental distribution maps overlap (marked with a blue frame in Figure 4.3c), to correlate the composition to the crystallography at the nanoparticles'

interfaces (Figure 4.3d). In these images, (111) and (110) reflections of the BaTiO$_3$ phase can be identified in close proximity of (531) and (220) reflections of the CoFe$_2$O$_4$ phase, pointing to a random mixing (*i.e.*, without any preferential orientation or epitaxy) of the two phases on the individual nanoparticulate level. Formation of intermediate phases such as Ba(Fe$_{10}$Ti$_2$)O$_{19}$ are reported to form as a result of interdiffusion between the two phases.[189] In our system, the sintering temperature is chosen to avoid such interdiffusion, and the HRTEM analysis confirms the absence of any intermediate phases at the BaTiO$_3$-CoFe$_2$O$_4$ interfaces. The absence of such an interphase is essential for an efficient strain transfer through the interface and thereby coupling between the magnetic and electric degrees-of-freedom. In addition, HRTEM images taken on the co-dispersed samples with 50 wt% CoFe$_2$O$_4$ do not reveal the evolution of any tertiary phase, which means that direct interfacial contacts can be maintained between the piezoelectric and magnetostrictive phases also for increased BaTiO$_3$-CoFe$_2$O$_4$ interphase boundaries. (see Supporting Information, Figure S4.4).

In Figure 4.3e, high angle annular dark field (HAADF) STEM images of a 100 nm thick BaTiO$_3$-CoFe$_2$O$_4$ bilayer is shown in order to investigate the interface between the two types of building blocks in the multilayered composite geometry. In HAADF STEM mode, contrast occurs as a result of atomic number differences, because heavier elements scatter electrons more thus appearing brighter. In Figure 4.3e, two distinct and sharp contrasts can be distinguished, corresponding to BaTiO$_3$ and CoFe$_2$O$_4$ layers, respectively, indicating that the interface between the BaTiO$_3$ and CoFe$_2$O$_4$ layers is sharply defined and the structure remains fully phase separated after sintering.
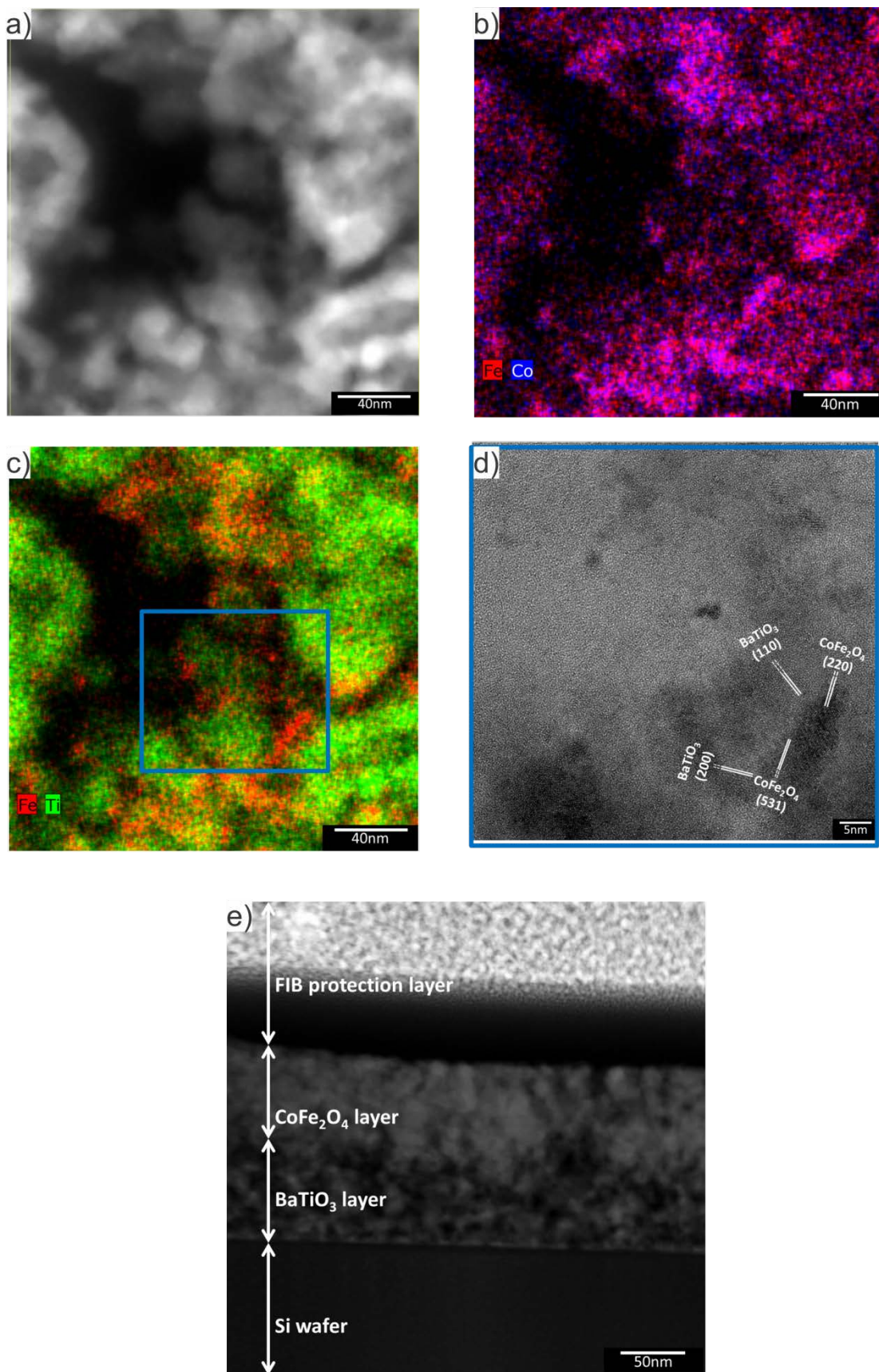
Figure 4.3 a) STEM overview image of the EDX mapped area, b) Fe-Co and c) Fe-Ti elemental maps on the area shown in a). d) Magnified HRTEM image of the area marked with

a blue box in c), revealing the d-spacings of the particles as deduced from their FFT patterns e) STEM image of an approx. 100 nm thick BaTiO$_3$-CoFe$_2$O$_4$ bilayered stack.

Optical & Electrical Characterization

Optical characteristics of the co-dispersed nanocomposite samples are discussed via their absorption coefficients and band gaps, which are derived from the measured reflection and transmission spectra. The absorption coefficients, α, are calculated via αd= ln(1-T/R), where d denotes sample thickness, T transmission and R diffuse reflection,[190] Figure 4.4a. In a next step, the calculated α values are inserted into Tauc plots in order to determine the band gaps, Figure 4.4b. Maximum absorption coefficients of 41000, 45000 and 72500 cm^{-1} are measured for 5, 10 and 50 wt% CoFe$_2$O$_4$ contents, implying an enhancement in optical absorption with increasing CoFe$_2$O$_4$ content. Similarly, band gap values decrease systematically as a result of increasing CoFe$_2$O$_4$ content in the composites (Table 4.1) for both direct and indirect transitions, with a congruent decrease in the transparency range. We believe that the nature of the transitions is rather indirect, considering the dark colors and high absorption of the samples in the visible range, which is also in agreement with the findings in a similar system in the literature.[191] Such a dependence of band gap values on magnetostrictive phase content is attributed to a possible cation interdiffusion during sintering, lattice parameter change, or particle size, previously.[191] However assigning one of these factors as an exact root cause is difficult and requires more research in this direction. Nevertheless, the correlation between the indirect band gap energies and CoFe$_2$O$_4$ content indicates that the absorption edge of the samples can be tuned effectively by CoFe$_2$O$_4$ incorporation, rendering these materials interesting for photocatalytic and solar-cell applications in addition to magnetoelectric systems.

**Table 4.1** Indirect and direct band gap energies of the co-dispersed composites

| Sample	Band gap energy (eV)	
	Indirect	Direct
BaTiO$_3$-5 wt% CoFe$_2$O$_4$	3.87	3.2
BaTiO$_3$-10 wt% CoFe$_2$O$_4$	3.73	3.1
BaTiO$_3$-50 wt% CoFe$_2$O$_4$	3.67	2.72
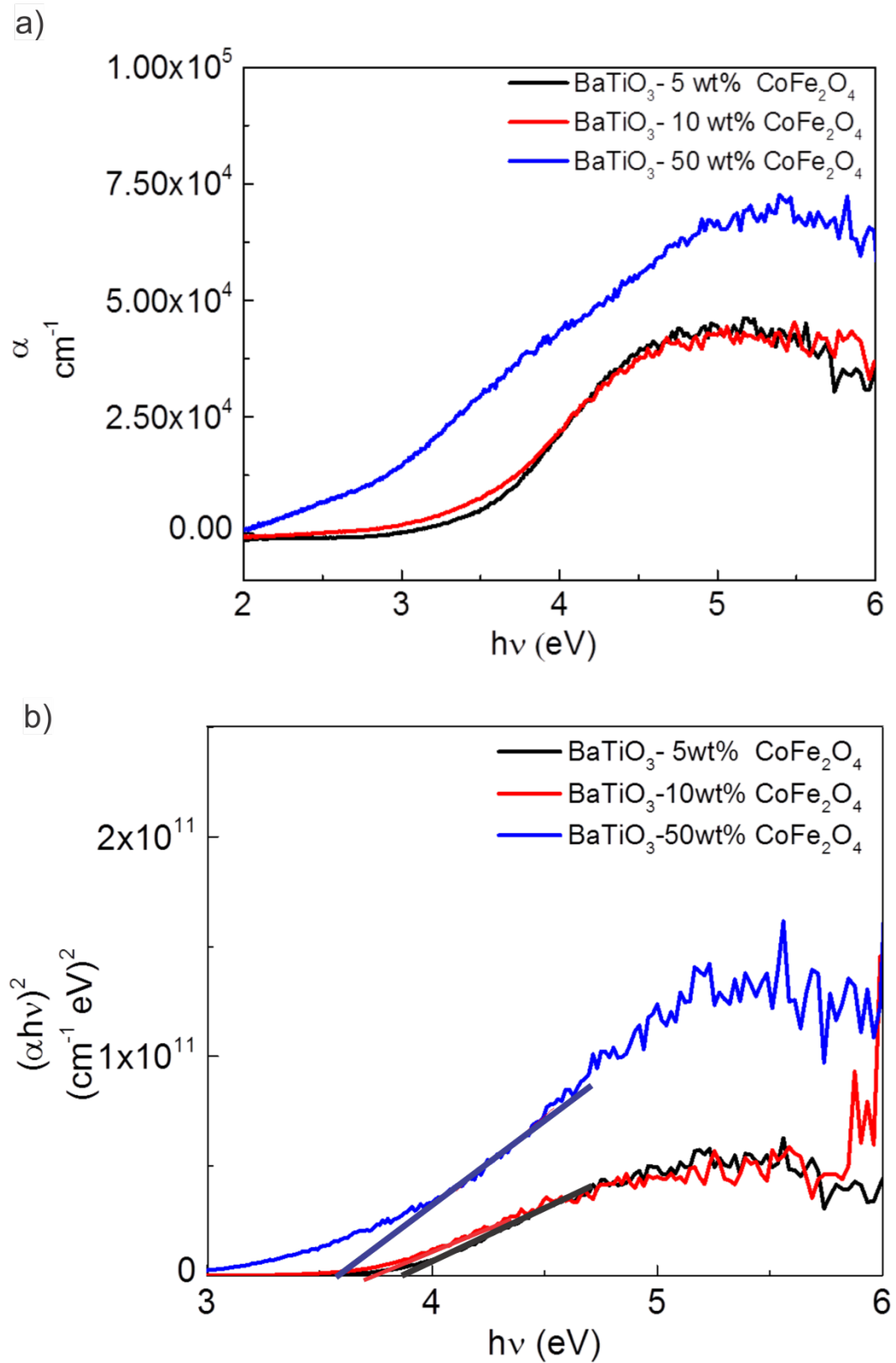
Figure 4.4 a) Absorption coefficients and b) Tauc plots for indirect transitions of the co-dispersed composites with 5, 10 and 50 wt% CoFe$_2$O$_4$.

The electrical characterizations of the co-dispersed thin film composite samples are carried out by using piezoresponse force microscopy (PFM) and electrochemical impedance spectroscopy (EIS) on the thin films of approx. 800 nm thickness, which are produced by two cycles of spin coating-500 $^{\circ}$C calcination using premixed nanoparticle dispersions of 100 mg/ml concentration on Pt covered Si substrate followed by one final 700 $^{\circ}$C sintering step in air.

For PFM measurements, doped diamond PFM tip is used as top electrode, while for EIS measurements, circular Pt top electrodes of 0.1mm diameter and 100 nm thickness are sputter deposited on the samples using shadow mask. Switching spectroscopy PFM measurements on the BaTiO$_3$-5 wt% CoFe$_2$O$_4$ film show that the sample exhibits well-saturated hysteresis loops with ferroelectric domain nucleation voltages reaching towards 1.8 V for positive bias and 2.6 V for negative bias (Figure 4.5a-b). Similarly, the amplitude of the piezoresponse under positive bias is larger than the amplitude of the piezoresponse under negative bias. This asymmetry in the switching behavior is attributed to the asymmetry of the electrical contacts used during the measurements.[192] Furthermore, longitudinal shear piezoelectric coefficients are calculated from the measured amplitude and phase responses of the piezoelectric deflections. The longitudinal shear piezoelectric coefficient (d$_{33}$) is a measure of the amount of longitudinal stress in case of a vertically applied electric field. Thus, high values of d$_{33}$ are desired for an efficient strain-mediated magnetoelectric coupling. In our case, a maximum of longitudinal shear piezoelectric coefficient (d$_{33}$) of 18 pm/V is measured for the BaTiO$_3$-5 wt% CoFe$_2$O$_4$ sample, which lies in the range of previously reported d$_{33}$ values for nanocrystalline BaTiO$_3$ in the literature.[193] As the concentration of CoFe$_2$O$_4$ is increased to 7 wt%, a dramatic decrease in d$_{33}$ is observed, which reaches a maximum value of only 5 pm/V. In addition, the hysteresis loops become narrower and less defined (Figure 4.5c and 4.5d). This observation can be explained by the conductive character of CoFe$_2$O$_4$, which increases the leakage current in the composites, thereby decreasing the amount of electrically created charges in the ferroelectric phase. These results suggest that the optimum CoFe$_2$O$_4$ content is around 5 wt% for a sufficient dual presence of electric and magnetic orders. The phase piezoresponse image taken on the electrically poled areas with $\pm$ 10 V external electrical potentials prove the fully reversible and unambigious ferroelectric nature of the sample, Figure 4.6a and 4.6b. The topography of the same region is shown in Figure 4.6c.
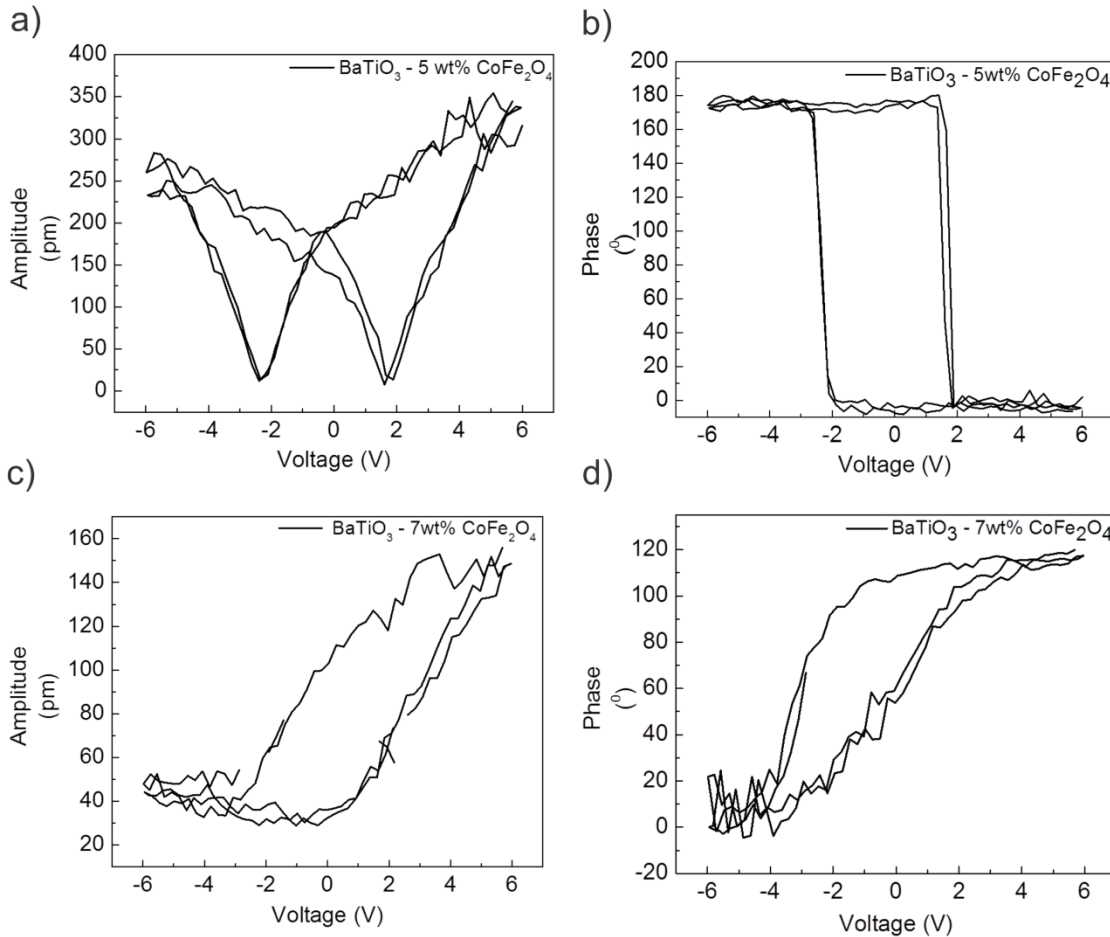
Figure 4.5 Amplitude and phase values of the switching spectroscopy PFM measurements on a-b) BaTiO$_3$-5 wt% CoFe$_2$O$_4$, c-d) BaTiO$_3$-7 wt% CoFe$_2$O$_4$ co-dispersed thin film nanocomposite samples.
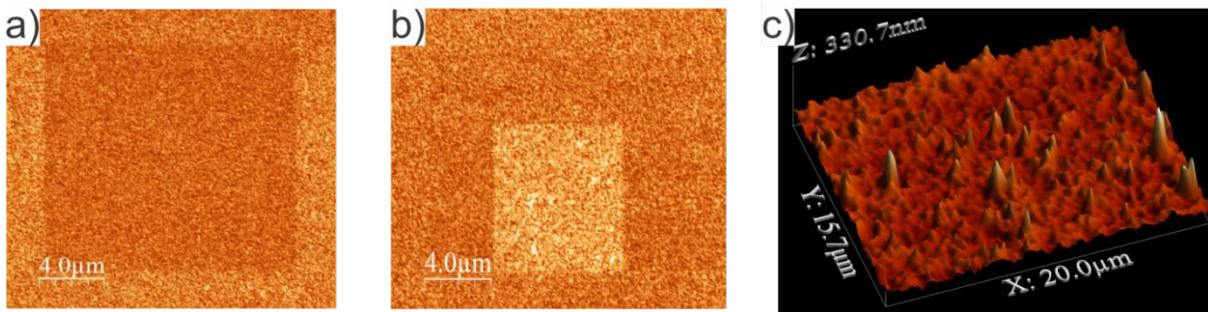
Figure 4.6 a) Piezoresponse phase image of the sample poled using +10 V obtained at the off contact resonance of the PFM tip, where darker contrast represents the poled region. b) Phase image of the same area, where a smaller square region (of lighter contrast in the image) has been poled using -10 V in the previously poled region of a BaTiO$_3$-5 wt% CoFe$_2$O$_4$ sample c) 3-D height retrace image of the same region obtained at the contact resonance of the PFM tip, revealing topography.

EIS measurements shed more light on the electrical characteristics of co-dispersed composites with 5-50 wt% CoFe$_2$O$_4$ on a wide frequency range (between 10 Hz-1 MHz), Figure 4.7a-d. The impedance spectra of the samples with 10-50 wt% CoFe$_2$O$_4$ exhibit two depressed semicircles, corresponding to different relaxation processes in high and low frequency ranges. The high frequency semicircle is assigned to the bulk properties of the composite, whereas the low frequency semicircle appears as a result of the interfaces (grain boundaries, interphase boundaries etc.). The electrical circuit analogues of the impedance spectra can be fitted using two constant phase elements (CPE) with parallel parasitic resistances connected in series, representing high and low frequency relaxation distributions (Figure 4.7b-d, insets). However, the impedance spectrum of the 5 wt% CoFe$_2$O$_4$ sample displays a single depressed semicircle, indicating a homogenous electrical microstructure over the measured frequency range. Therefore, the EIS of this composite can be modeled with a single CPE (Figure 4.7a, inset). Obviously, in the 10 wt% sample the percolation threshold of the CoFe$_2$O$_4$ phase is exceeded and additional relaxation processes at lower frequencies associated with the grain and interphase boundaries come into play. The fit and error values obtained from the equivalent electrical circuits are shown in Table 4.2. Here, only the fitting results of the high frequency CPE (in 500 Hz-100 kHz range) are shown, where the data consistency is high according to the Kramers-Kronig analysis. The C and n values of the CPE denote the equivalent capacitance and the constant phase element exponent, which is related to the distribution of relaxation times and deviation from ideal capacitor behavior (n =1 for ideal capacitor). A decrease in n can be seen upon increase in the CoFe$_2$O$_4$ content, which points out to a larger deviation from ideal capacitor. This phenomenon is a consequence of the inhomogeneous microstructure and related complex electrical relaxation behavior of the material above the CoFe$_2$O$_4$ percolation threshold, in agreement with the previous findings in the literature.[194] Similarly, the parasitic resistance, R, of the CPE decreases in parallel to the increase in the CoFe$_2$O$_4$ content, due to the lower resistance of CoFe$_2$O$_4$ as compared to BaTiO$_3$. The leaky network formed above the CoFe$_2$O$_4$ percolation threshold restricts the polarizability of the composites, in agreement with the switching spectroscopy PFM observations that d$_{33}$ lowers with increase in CoFe$_2$O$_4$ content. The low frequency CPEs forming above the percolation threshold have capacitance values in 100-700 pF range, which is lower than the typically observed low frequency capacitance values lying in the nF range (see Table S4.2 in Supporting Information).[195] This is a common indication of residual porosity and incomplete necking in the sintered ceramics, in agreement with 30 - 50 % porosity found in the FIB-tomography images (see Supporting Information, Figure S4.2).[195] The dielectric permittivity is derived using parallel plate capacitor relationships in order to investigate the frequency dependent polarization behavior of the composites. Both the permittivity and loss tangents are characterized by a rapid decrease in the 500 Hz-10 kHz range and remain unchanged with increasing frequencies for all the composite samples (Figure 4.7e and 4.7f). At lower frequencies, a Maxwell-Wagner polarization mechanism is active and causes a large dielectric permittivity as a consequence of the effective interaction between the samples and the alternating electrical field, while higher frequencies are too fast for the samples for a polarization change matching the alternating field, resulting in a rapid decrease in permittivity and thus in loss tangents. The relatively high loss tangents (max. 2) are an implication of the porous structure. At this point, it is necessary to mention that the impedance characteristics do not correlate linearly with the composition, because the permittivity and the loss tangents depend on many factors such as grain size or porosity in addition to composition and microstructure.
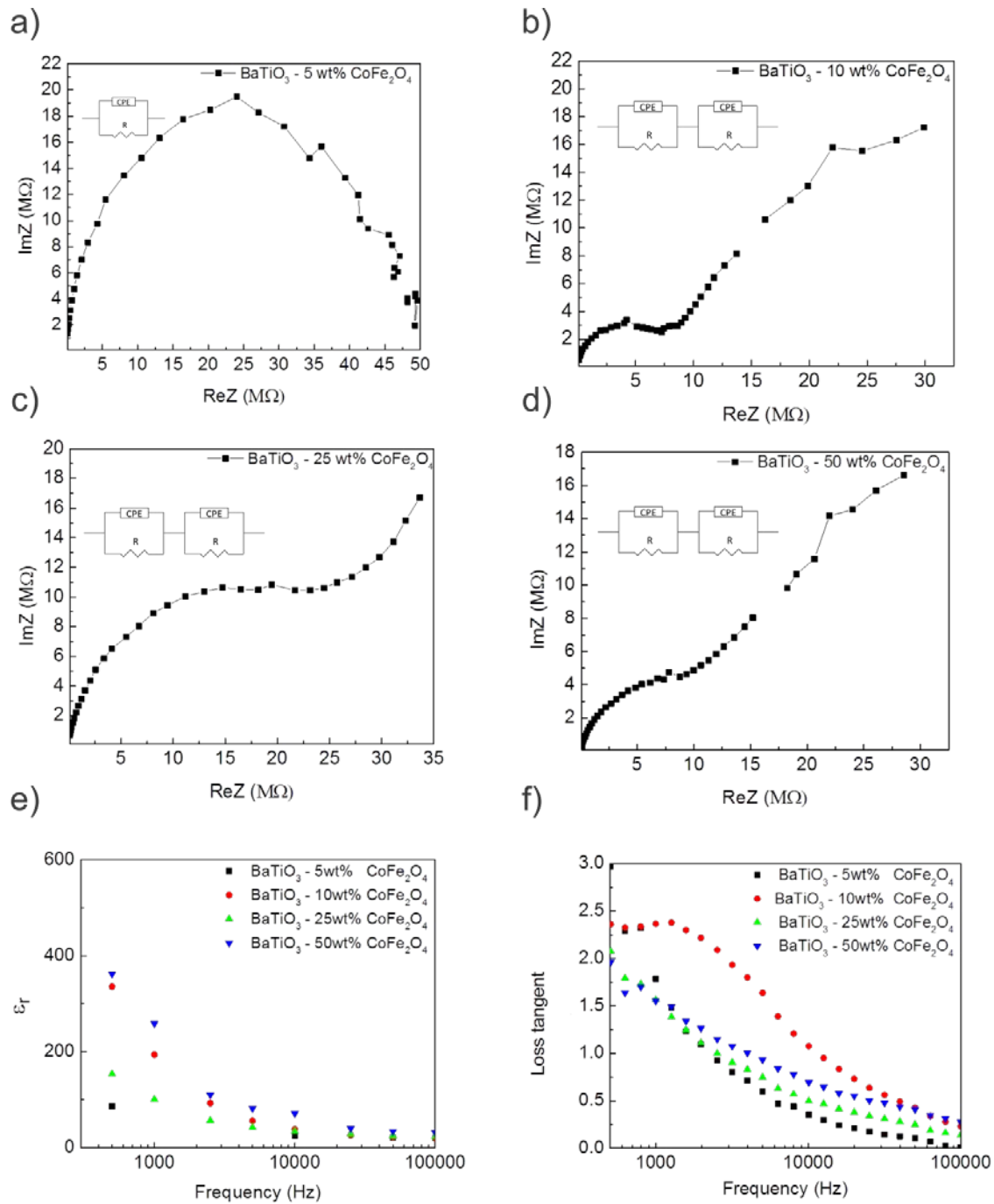
Figure 4.7 EIS measurements of the co-dispersed composite films (ca. 800 nm thick) with the composition a) BaTiO$_3$-5 wt% CoFe$_2$O$_4$, b) BaTiO$_3$-10 wt% CoFe$_2$O$_4$, c) BaTiO$_3$-25 wt% CoFe$_2$O$_4$, d) BaTiO$_3$-50 wt% CoFe$_2$O$_4$ e) dielectric permittivity and f) dielectric loss tangents of the same BaTiO$_3$- 5-50 wt% CoFe$_2$O$_4$ co-dispersed thin film nanocomposites.

BaTiO$_3$-5 wt% CoFe$_2$O$_4$	3.01 pF (1.6%)	0.95 (0.86%)	40.7 MΩ (2.13%)
BaTiO$_3$-10 wt% CoFe$_2$O$_4$	17.1 pF (1.7%)	0.82 (1.5%)	10.3 MΩ (2.26%)
BaTiO$_3$-25 wt% CoFe$_2$O$_4$	16 pF (1.3%)	0.83 (0.95%)	30 MΩ (2.4%)
BaTiO$_3$-50 wt% CoFe$_2$O$_4$	65.8 pF (1.01%)	0.77 (0.94 %)	11.5 MΩ (2.3%)

Table 4.2 Fit results of the high frequency CPE of co-dispersed composites

Magnetic & Magnetoelectric Properties

The room temperature magnetic properties of the co-dispersed composites are characterized by out-of-plane hysteresis measurements on 200 nm thick films, Figure 4.8a-c. In these hysteresis loops, the magnetic moments of the samples are normalized with respect to the magnetic moments of the BaTiO$_3$ - 50 wt% CoFe$_2$O$_4$ sample measured at saturation. The out-of-plane hysteresis loops of all samples display superparamagnetic characteristics with slight coercivities. The coercivity of the samples in the compositional range 10-50 wt% CoFe$_2$O$_4$ vary between 15-50 Oe, while the sample with 5 wt% CoFe$_2$O$_4$ possesses a coercivity of 125 Oe (Figure 4.8a-b). At lower concentrations, the CoFe$_2$O$_4$ particles are more isolated, leading to a decrease in long range magnetic dipolar interactions. However, samples containing CoFe$_2$O$_4$ above the percolation threshold (corresponding to samples with 10 wt% CoFe$_2$O$_4$ and more), the CoFe$_2$O$_4$ nanoparticles are in close contact with each other, therefore having a higher dipolar interactions with a parallel softening in the coercivities. A similar dependence of the coercivities on the magnetic ferrite content has been reported previously in the BaTiO$_3$-NiFe$_2$O$_4$ system.[196] As expected, the induced magnetization in the samples increases with increasing CoFe$_2$O$_4$ content. Hysteresis measurements carried out at 10 K show an increase in the magnetic coercivity from 8 kOe to 20 kOe with increasing CoFe$_2$O$_4$ content (Figure 4.8c). At a temperature of 10 K, the exchange interactions increase and dominate the dipolar interactions, giving rise to an increase in magnetic coercivity with increasing CoFe$_2$O$_4$ content in contrast to the room temperature measurements.
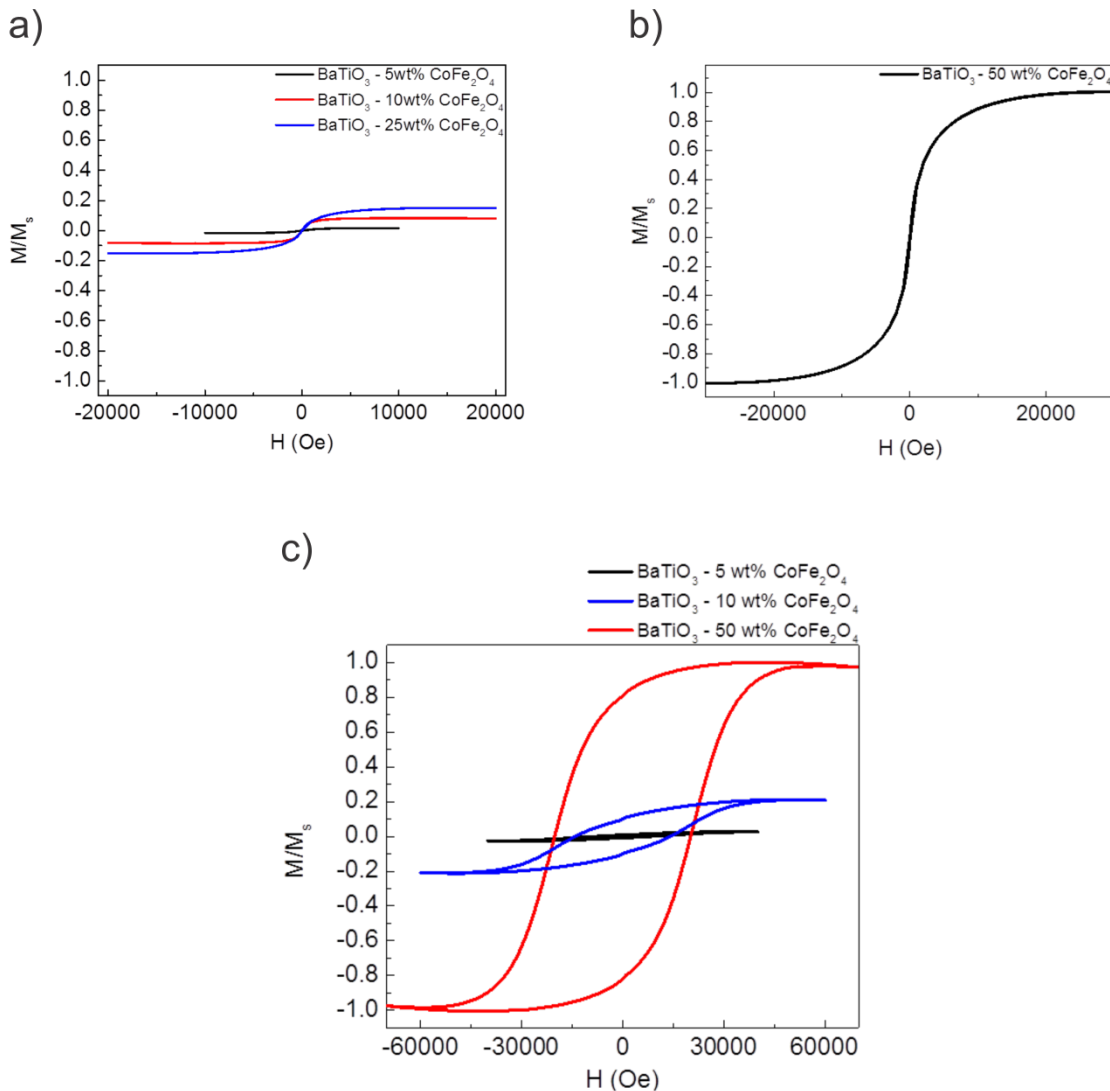
Figure 4.8 Out-of-plane SQUID hysteresis measurements on 200 nm thick co-dispersed composite films: a) BaTiO$_3$-5-25 wt% CoFe$_2$O$_4$ and b) BaTiO$_3$-50 wt% CoFe$_2$O$_4$ measured at room temperature, c) hysteresis measurements on BaTiO$_3$- 5-50 wt% CoFe$_2$O$_4$ samples measured at 10 K.

Zero field (ZFC) and field (FC) cooling curves are measured to further investigate the superparamagnetic characteristics (Figure 4.9). The monotonous increase in magnetization with decreasing temperatures as seen in the FC curves of all samples indicates that the magnetic properties are predominantly superparamagnetic. All samples display blocking temperatures, T_B, in the range of 150 - 275 K in their ZFC, corresponding to a magnetic particle size between approx. 4-8 nm, which is below the superparamagnetic size limit.[197] The presence of slight coercivities observed in the room temperature hysteresis curves, in contrast to the superparamagnetic ZFC-FC measurements, can be explained by the presence of a limited number of particles, which grew to sizes above the superparamagnetic size limit as a result of sintering.
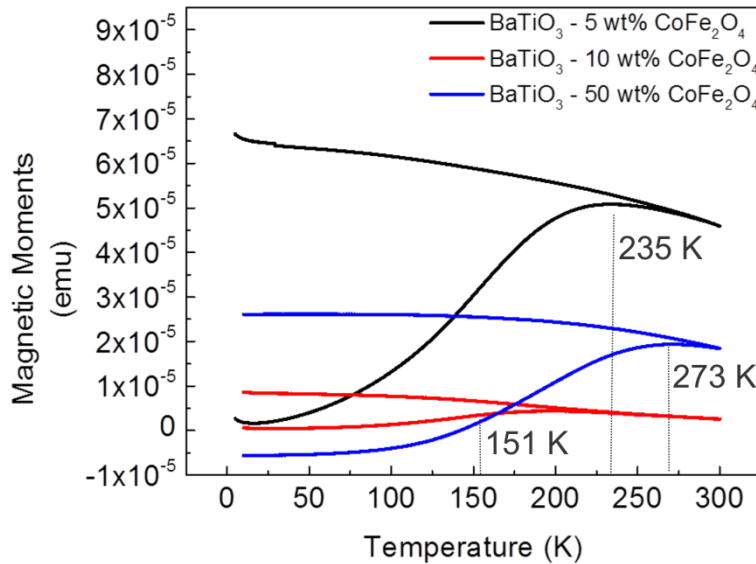
Figure 4.9 ZFC and FC cooling curves of the $BaTiO_3$- 5-50 wt% $CoFe_2O_4$ co-dispersed composite thin films obtained using 1000 Oe of external magnetic field. The thin vertical grey lines denote the maximum measured magnetization, corresponding to blocking temperature.

Element specific magnetic characteristics of the samples are investigated by X-ray magnetic circular dichroism (XMCD) measurements at the Fe edge of the $BaTiO_3$-$CoFe_2O_4$ co-dispersed thin film composites with 5, 25 and 50 wt% $CoFe_2O_4$ using an out-of-plane external magnetic field of 40 Oe (Figure 4.10 a-d) under ambient conditions, *i.e.*, without any external cooling. All the samples are approx. 200 nm thick. In all the XMCD spectra, 3 distinctive features are visible at the L_3 edge, assignable to Fe^{2+} at octahedral sites and to Fe^{3+} at tetrahedral and octahedral sites. Additionally, the sign of the XMCD signal from the octahedral sites is opposite to the one from the tetrahedral sites. This reveals the ferrimagnetic nature of the cobalt ferrite, consisting of two magnetic sublattices, which are antiferromagnetically coupled to each other. The magnetic origin of the observed XMCD signal is confirmed by changing the direction of the external magnetic field, upon which the signal switched parallel to the magnetic field (Figure 4.10c and 4.10d).

In a next step, the XMCD measurements are repeated following the application of an electrical field of +40 V for electrical poling of the $BaTiO_3$-5wt% $CoFe_2O_4$ sample to investigate also the magnetoelectric coupling effect (Figure 4.11a-d). In-plane electric fields are applied using two top electrodes with 0.1 mm separation obtained by the deposition of 20 nm thick Cr stripes on the sintered thin films. The electric poling would not be efficient for the other co-dispersed composite thin film samples richer in $CoFe_2O_4$ due to the enhanced leaky behavior above the $CoFe_2O_4$ percolation limit. In Figure 4.11a-b, XMCD measurements carried out after applying a 40 V DC electric voltage pulse are shown for out-of-plane magnetization. The peak integrals of the tetrahedral Fe^{3+} peaks are normalized to the X-ray absorption peak at the L_3 in order to have a quantitative comparison of the out-of-plane XMCD signal. For magnetic fields applied in both directions, the XMCD signal strength at the Fe^{3+} site corresponds to approx. 3.4 % of the total L_3 X-ray absorption peak. When the same XMCD measurements are repeated after poling, a signal decrease takes place, up to 25% in case of (-) magnetic field direction, while no XMCD signal in the (+) magnetic field direction can be obtained (Table 4.3). In case of in-plane XMCD signals (Figure 4.11c and 4.11d), the electrical poling causes a switching in the magnetization direction of the sample, when compared to the XMCD signal, which is obtained using magnetic fields only. This

finding points to the fact that in-plane electric pulses generate a 180° reorientation in the magnetization of the sample in presence of an external magnetic field. Obviously, in-plane electrical poling creates an in-plane easy magnetic axis together with a hard magnetic axis in the out-of-plane direction. Accordingly, there is a strong magnetoelectric coupling between the BaTiO$_3$ and CoFe$_2$O$_4$ phases in the dilute co-dispersed thin film composite samples, enabling electric control of the magnetic order in these composites under ambient temperatures.
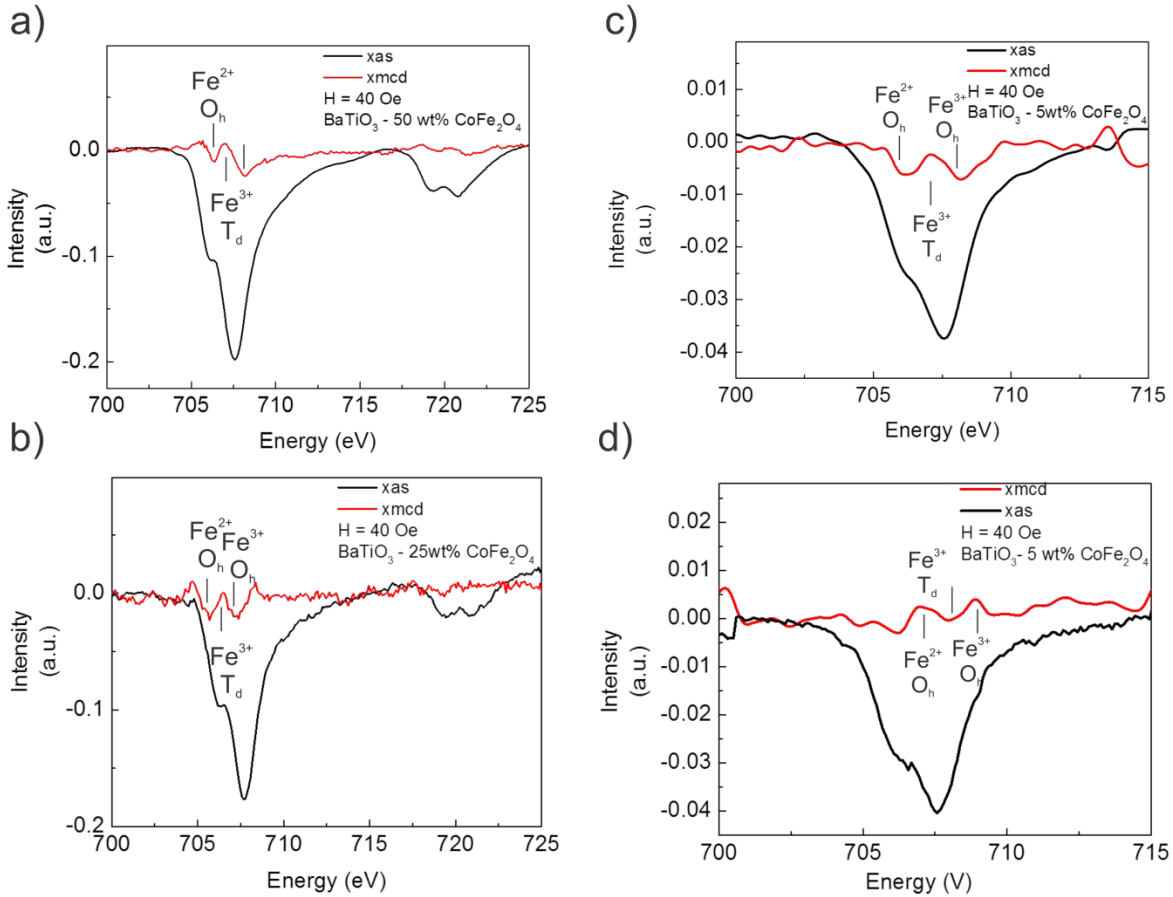
Figure 4.10 Fe L$_3$ and L$_2$ XMCD and XAS spectra of a) BaTiO$_3$-50 wt% CoFe$_2$O$_4$, b) BaTiO$_3$-25 wt% CoFe$_2$O$_4$. c) Fe L$_3$ edge XMCD and XAS of BaTiO$_3$-5 wt% CoFe$_2$O$_4$. d) Fe L$_3$ edge XMCD and XAS of BaTiO$_3$-5 wt% CoFe$_2$O$_4$ recorded with an external magnetic field in the opposite direction to prove the magnetic origin of the observed XMCD signal. All samples are in the co-dispersed thin film composite configuration with an approx. thickness of 200 nm. The strength of the external magnetic field is 40 Oe.
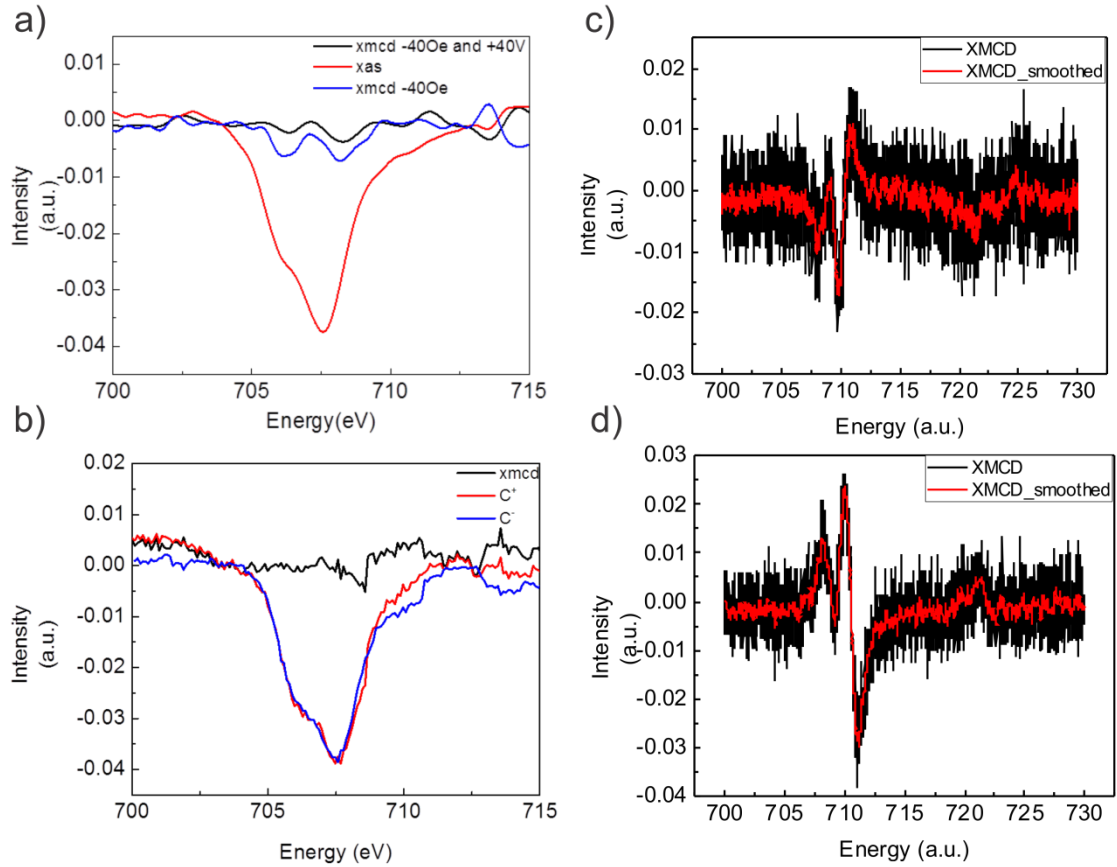
Figure 4.11 a) Fe L$_3$ edge XMCD spectra of BaTiO$_3$-5 wt% CoFe$_2$O$_4$ co-dispersed composite thin film after application of an electrical pulse of 40 V for poling (black line). For comparison, the XMCD of the same sample obtained after applying only magnetic fields is also shown. b) Fe L$_3$ edge XMCD acquired under an external magnetic field of 40 Oe after application of an electrical pulse of 40 V c) L$_3$ and L$_2$ edge XMCD spectra of BaTiO$_3$-5 wt% CoFe$_2$O$_4$ co-dispersed composite thin film taken under 1000 Oe in-plane external magnetic field d) The same measurement repeated after 40V DC electrical poling, exhibiting magnetization reversal.

Table 4.3 Integral L$_3$ edge XAS and XMCD (at Fe^{3+} T$_d$ position) peak intensity values and peak positions in electron volts (eV)

	XMCD	XAS	XMCD/XAS (%)
+40 Oe	0.00428 (707.87 eV)	0.129 (707.57)	3.3
-40 Oe	0.00503 (708.07 eV)	0.147 (707.57)	3.4
-40 Oe +40V	0.0032 (706.98 eV)	0.125 (707.58)	2.56
+40 Oe +40V	N/A	0.139 (707.48)	N/A

Conclusion

Starting from nanoparticle dispersions, we use a wet-chemical deposition method to fabricate BaTiO$_3$-CoFe$_2$O$_4$ nanocomposite thin films with different configurations, such as co-dispersed and multilayered composite geometries and over a wide range of compositions and thicknesses for room temperature magnetoelectric coupling. For the co-dispersed connectivity scheme, mixing of the two components at nanoparticle level is proven by HRTEM, providing enlarged interfacial area for coupling. We found that there is an optimum BaTiO$_3$-CoFe$_2$O$_4$ ratio with the limiting concentration on the magnetic constituent, due to increased leakage and ferroelectric poling problems. The dilute composite with 5 wt% CoFe$_2$O$_4$ content exhibits fully switchable ferroelectric characteristics with a d$_{33}$ of max. 25 pm/V and a magnetic coercivity around 125 Oe, displaying ferroelectric and superparamagnetic orders at room temperature. XMCD measurements at the Fe edge prove that the coupling between the electrical and magnetic degrees of freedom manifests itself as a creation of easy magnetization axis in the in-plane direction with a congruent decrease in magnetization in the out-of-plane direction upon in-plane electrical poling. Hence, this method can be potentially used in future applications for room temperature electric control of magnetism, magnetic field sensors and actuators, energy harvesting, novel memory elements, and microwave devices.

Experimental
Materials

Dendritic metal pieces of barium (99.99 % purity), titanium (IV) isopropoxide (99.999 % purity), cobalt and iron acetylacetonate [Co(C$_5$H$_7$O$_2$)$_2$, > 97 %, Fe(C$_5$H$_7$O$_2$)$_3$, > 99.8%], anhydrous benzyl alcohol (> 99.8%), acetone (> 99.5%), isopropanol (> 99.8%), 2-[2-(2-methoxyethoxy)ethoxy]acetic acid (technical grade) and hexane (> 95 % purity) are purchased from Sigma-Aldrich and used without any further purification. Ethanol of 99.8 % purity is obtained from Fluka. Acetophenone (98 % purity) is obtained from Acros organics and degassed via 3 cycles of freeze-thaw degassing before the synthesis. Fused silica, <100> oriented p-type Si wafers, and Pt/TiO$_2$/SiO$_2$/Si wafers are obtained from MTI Corp, USA and used for film deposition. The substrates are sonicated in acetone and isopropanol for 5 minutes each prior to film deposition. For the XMCD and XAS measurements carried out under the transmission X-ray microscope, 5×5 mm Si frames containing 1.5×1.5 mm wide and 200 nm thick Si$_x$N$_y$ membranes are used (Norcada Inc., Canada).

Synthesis and Dispersion of Nanoparticles

For the synthesis of BaTiO$_3$ nanoparticles, previously published protocols are combined and adapted.[120, 198] In a typical synthesis, 137 mg dendritic Ba is dissolved in 5 ml degassed acetophenone at 80 $^\circ$C in an Argon filled glove box, followed by dropwise addition of a molar equivalent of titanium isopropoxide. The mixture is transferred to a microwave vial, sealed and exposed to microwave irradiation for 30 minutes at a synthesis temperature of 220 $^\circ$C using a CEM Discovery reactor operating at 2.45 GHz. For CoFe$_2$O$_4$ synthesis, 353 mg Fe(C$_5$H$_7$O$_2$)$_3$ and 120 mg of Co(C$_5$H$_7$O$_2$)$_2$ are mixed with 5 ml of benzyl alcohol in an argon filled glovebox and subjected to microwave radiation at 180 $^\circ$C for 30 minutes in a 10 ml Teflon capped glass vessel according to a previously published procedure.[136] The BaTiO$_3$ and CoFe$_2$O$_4$ nanoparticles are centrifuged off at 4000 rpm, washed twice with ethanol and finally sonicated for 45 minutes in 5 ml 0.3 M ethanolic MEEAA solution using a Branson B3510 ultrasonic cleaner. After sonication, the nanoparticles are further stirred overnight in this mixture to ensure sufficient binding of the stabilizing molecules to the nanoparticle surfaces. In the next step, an excessive amount of hexane (5:1 hexane to ethanol ratio in volume) is added and the mixture is centrifuged to separate the nanoparticles from excess stabilizing agent. Afterwards, the BaTiO$_3$ and CoFe$_2$O$_4$ nanoparticles are re-dispersed in

ethanol with a subsequent sonication step. To obtain the thin film composite samples with different compositions, co-dispersions of BaTiO$_3$ and CoFe$_2$O$_4$ are mixed in the desired ratios as presented in Table 4.4. After mixing, the co-dispersions are sonicated for 10 min and magnetically stirred for another 3-5 minutes.

Table 4.4 Mixing ratios of the nanoparticle dispersions for co-dispersed composites in the range of 5-50 wt% CoFe$_2$O$_4$

Samples	BaTiO$_3$ (100 mg/ml)	CoFe$_2$O$_4$ (100 mg/ml)
BaTiO$_3$-5 wt% CoFe$_2$O$_4$	1 ml	0.05 ml
BaTiO$_3$-10 wt% CoFe$_2$O$_4$	1.5 ml	0.15 ml
BaTiO$_3$-25 wt% CoFe$_2$O$_4$	1 ml	0.33 ml
BaTiO$_3$-50 wt% CoFe$_2$O$_4$	1 ml	1 ml

Thin Film Deposition

Both the co-dispersed and the multilayered composites are deposited using cycles of spin coating and calcination at 500 $^{\circ}$C on a hot plate heated to the calcination temperature at a rate of 25 $^{\circ}$C/min. The calcination is applied after the deposition of each layer by spin coating. The spin coating-calcination cycles are repeated either to tune thickness for co-dispersed composites in 50 nm -2 μm range or to prepare the sequential stacks of BaTiO$_3$ – CoFe$_2$O$_4$ multilayers. For the spin coating, a maximum spinning speed of 1000 rpms for a total period of 20 seconds using a Laurell WS650 spin coater is employed. All film deposition processes prior to sintering are carried out in a laminar flow controlled synthetic air filled glovebox. Sintering in air at 700 $^{\circ}$C for 2 hours with 4 hours of ramping rate for compaction is performed in a Nabertherm L 3/11/B170 laboratory muffle furnace to finalize the film fabrication process.

Characterization

XRD patterns are obtained using thin film optics (Goebbels mirror on the incident side and parallel plate collimator on the diffracted side) in grazing incidence geometry from a Panalytical X'Pert Pro diffractometer with Cu Kα source. SEM images of the thin films deposited on Si wafers are captured at an operation voltage of 3-5 kV using a LEO 1530 (Germany) scanning electron microscope. TEM images are obtained using FEI Talos F200X in the high angle annular scanning transmission electron microscopy mode. UV-*vis* spectra are recorded with a JASCO V-770 spectrophotometer with an integrating spheres accessory (ILN-725) with background and substrate correction. AFM topography images are acquired by an intermittent contact mode AFM from Asylum Cypher^{TM} using AC160TS-R3 tips. The ferroelectric properties are investigated using the DART-SSPFM mode of Asylum Cypher^{TM} using doped diamond PFM tips from NDMDT on films deposited on Pt/TiO$_2$/SiO$_2$/Si substrates with Pt bottom electrode being grounded during the measurements. Deflection in volts and thermal calibration of the tips are done prior to PFM measurements and the presented hysteresis curves are obtained in the remnant mode to minimize electromechanical tip-sample interactions with AC reading voltage between 0.5 - 1V. Electrochemical impedance spectroscopy measurements are carried out using Gamry electrochemical measurement system in 10 Hz-1 MHz frequency range with 50 mV of applied AC potential in cross-plane measurement geometry via top and bottom electrodes on films deposited on Pt/TiO$_2$/SiO$_2$/Si wafers with Pt as the bottom electrode. As top electrode, 200 nm thick circular Pt dots of 0.1 mm diameter are sputtered on the films using a shadow mask.

Magnetic properties are measured using a superconducting quantum interference device (SQUID) magnetometer MPMS from Quantum Design, and ZFC and FC curves are measured in an external field of 1000 Oe. XAS and XMCD spectra of the samples are recorded using a photoemission electron microscope (PEEM) and a scanning transmission X-ray microscope at the NanoXAS beamline, Swiss Light Source, Villigen, Switzerland. The spectra are taken with opposite X-ray photon helicities with 0.1 eV step size at an applied magnetic field of 40 Oe. XMCD was calculated by (C^+-C^-), where C^+ and C^- are right and left circularly polarized X-rays. For converse magnetoelectric effect measurements, the thin films are poled using in-plane electrical fields of 40 V prior to XMCD measurements. 20 nm thick Cr stripes of 0.1 μm width and 1 mm length are deposited onto the thin films deposited on Si$_x$N$_y$ membranes using a shadow mask for in-plane electrical poling. The PEEM measurements are repeated twice to reproduce the results.

Supporting Information
The tetragonality of the BaTiO$_3$ phase has been confirmed by XAS taken at the Ti edge (Figure S4.1). In the cubic crystal symmetry, only two discrete peaks at L$_3$ and L$_2$ are expected, because the t$_{2g}$ and e$_g$ splitting will be absent due to higher symmetry. In contrast, in the tetragonal crystal field, L$_3$ and L$_2$ edges will be splitted into two discrete energy levels, which will result in the formation of 4 distinct absoption peaks.
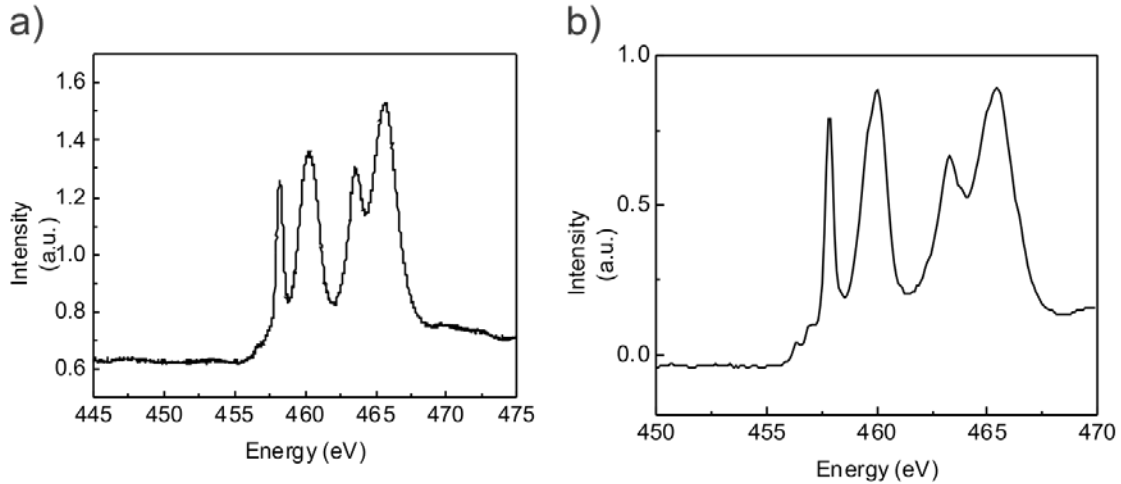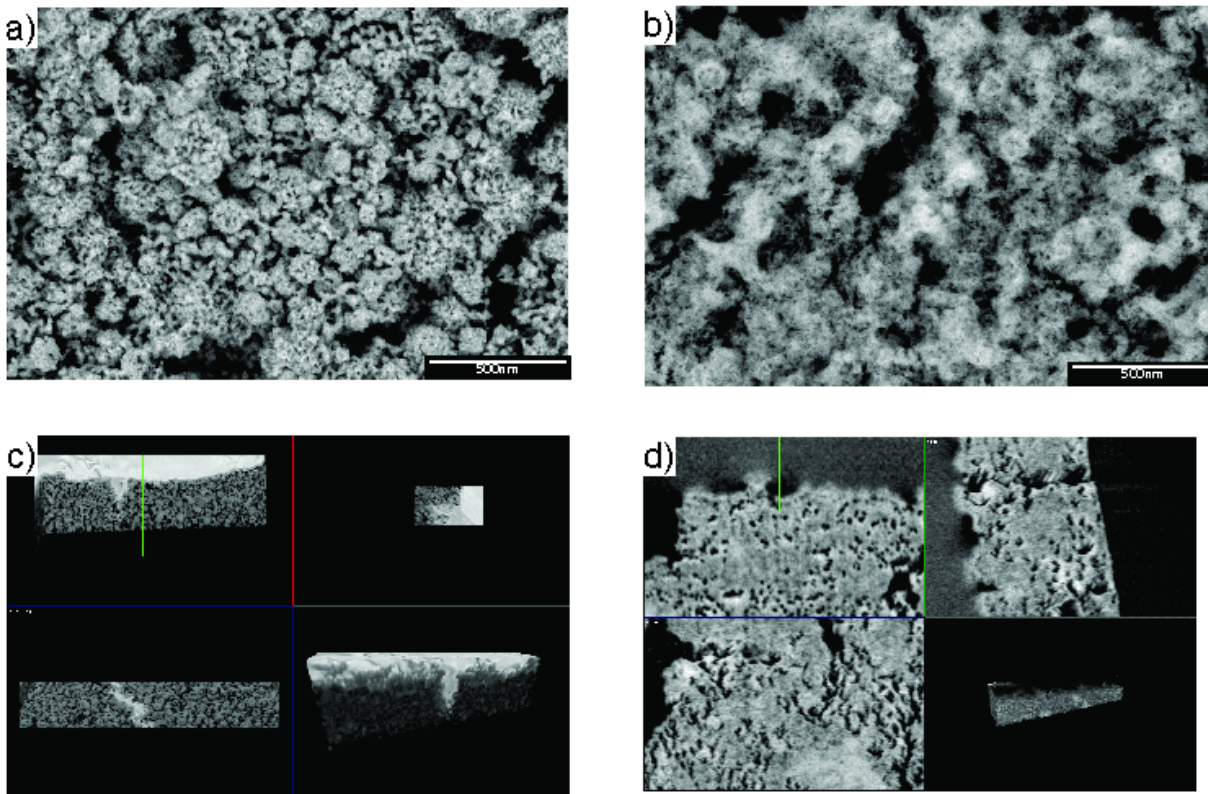
Figure S4.1 XAS taken at the Ti edge of a) BaTiO$_3$-5 wt% CoFe$_2$O$_4$ and b) BaTiO$_3$-50 wt% CoFe$_2$O$_4$ co-dispersed nanocomposite thin films.

Table S4.1 X-ray peak broadening of BaTiO$_3$ (110) reflections versus CoFe$_2$O$_4$ content of the co-dispersed composites.

Sample	FWHM (^{o})
BaTiO$_3$-5 wt% CoFe$_2$O$_4$	0.797
BaTiO$_3$-10 wt% CoFe$_2$O$_4$	0.968
BaTiO$_3$-25 wt% CoFe$_2$O$_4$	1.012
BaTiO$_3$-50 wt% CoFe$_2$O$_4$	1.011

For the porosity analysis of the sections obtained by FIB-tomography, each image was thresholded to assign different pixels to the pores and to the nanoparticle network. Subsequently, the area percentages of the pores are obtained using the "Analyze Particles" tool of the software ImageJ. The analysis resulted in 40 % porosity for BaTiO$_3$-5 wt% CoFe$_2$O$_4$ and 30 % porosity for BaTiO$_3$-50 wt% CoFe$_2$O$_4$ in the sintered co-dispersed nanocomposite thin film samples. The difference in density can be attributed to the broader particle size distribution in the case of the BaTiO$_3$-50 wt% CoFe$_2$O$_4$ sample, which presumably leads to a more efficient packing and enhanced sintering.

Figure S4.2 High resolution top view SEM images of the a) BaTiO$_3$-5 wt% CoFe$_2$O$_4$ and b) BaTiO$_3$-50 wt% CoFe$_2$O$_4$ co-dispersed nanocomposite thin films. FIB tomography orthogonal view of the sections in c) BaTiO$_3$-5 wt% CoFe$_2$O$_4$ and d) BaTiO$_3$-50 wt% CoFe$_2$O$_4$ co-dispersed nanocomposite thin films after sintering.
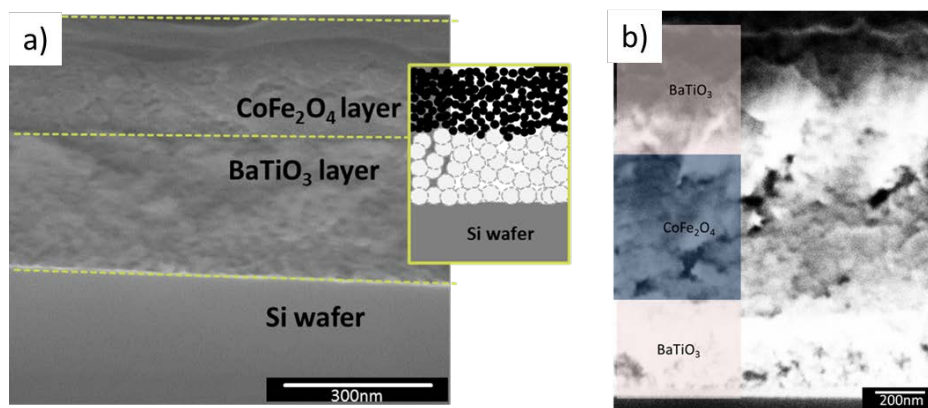
Figure S4.3 Cross-sectional SEM images of a multilayered composite film consisting of a) BaTiO$_3$-CoFe$_2$O$_4$ layers of 450 nm thickness, b) BaTiO$_3$-CoFe$_2$O$_4$-BaTiO$_3$ layers of 1.2 μm thickness.

Table S4.2 Low frequency CPE fit results for the 10-50 wt% CoFe$_2$O$_4$ co-dispersed composite films

Sample	C	n	R
BaTiO$_3$-10 wt% CoFe$_2$O$_4$	679 pF (2.32%)	0.73 (2.52%)	53 MΩ (14%)
BaTiO$_3$-25 wt% CoFe$_2$O$_4$	185 pF (1.26%)	0.63 (0.83%)	600 MΩ (48 %)
BaTiO$_3$-50 wt% CoFe$_2$O$_4$	440 pF (0.56 %)	0.5 (0.66 %)	165 MΩ (5%)
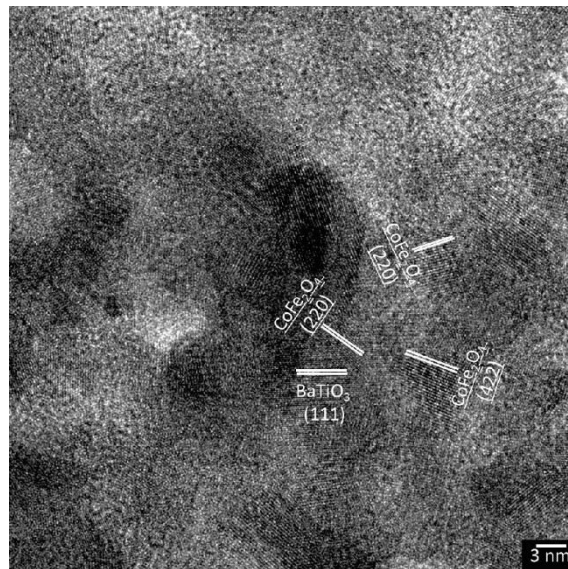
Figure S4.4 HRTEM image of the BaTiO$_3$-50 wt% CoFe$_2$O$_4$ co-dispersed nanocomposite thin film sample after sintering.

5.Conclusion

In this work, nanoparticle based liquid phase deposition is presented as a versatile, efficient and low-cost approach for colloidal assembly of functional thin films. The process involved synthesis of nanoparticles with desired properties and their post-synthesis surface-functionalization into highly concentrated dispersions. These dispersions are subsequently utilized in a carefully optimized spin coating-drying process followed by a single sintering step to obtain the functional thin films.

The approach is firstly demonstrated on $BaTiO_3$ thin films on a wide thickness range to address different device applications with different thickness requirements using a single deposition approach. It is understood that outgassing of organics during sintering limited the thickness of colloidal thin films to sub-micrometer ranges due to cracking. Through elimination of organics already at the drying stage, evolution of outgassing-induced tensile stresses is avoided. As a proof of concept, crack-free ferroelectrically switchable $BaTiO_3$ thin films in tens of nanometer to several micrometer thicknesses are deposited.

In the next step, the developed colloidal assembly approach is used to deposit $CoFe_2O_4$-SiO_2 thin films on a wide thickness as well as composition range, changing between 0-90 wt% SiO_2 content for magneto-optical applications. $CoFe_2O_4$ is chosen because of its attractive magneto-optical properties and via incorporation of SiO_2 nanoparticles, optical properties can be carefully tuned for integration of these materials into optical and magneto-optical systems. Furthermore, in-plane tensile stresses associated with constrained sintering conditions generated perpendicular magnetic anisotropy.

Deposition of state of the art artificial multiferroic $BaTiO_3$ - $CoFe_2O_4$ thin films is carried out in two different composites. The coexistence of ferroelectric and ferromagnetic orders in the final thin films is shown. Moreover, the coupling between the electrical and magnetic orders of the material is demonstrated as voltage control of magnetism via synchrotron based element specific magnetic measurements. These results point out to a potential use of these materials in future miniaturized memory elements, as well as microwave devices, sensors, and transducers.

The main problems encountered in nanoparticle based liquid phase deposition of thin films in the literature are absence of the desired functionalities in the final films and the limited integration possibilities of these materials into future devices. Among the root causes are cracking, evolution of undesired phases, lack of functionality in the as-synthesized nanoparticles, roughness, and residual porosity. In this work, the as-synthesized nanoparticles are of controlled phase and size and therefore bear the targeted functionalities. Colloidal assembly of thin films relying on these predefined building blocks results in emergence of targeted properties in the final films. Furthermore, a generalized thin film deposition procedure is engineered carefully to yield crack free films, and different thin film architectures of various functionalities can be fabricated using the same procedure. In order to further extend the potential application fields of these materials, residual porosity in the final films should be minimized. For this purpose, more advanced sintering techniques and/or different sintering atmospheres can be utilized to develop an optimized sintering recipe for the highest final density in the thin films. Another possible future direction would be to investigate the constrained sintering conditions, in order to harvest the linked stresses for other exciting applications, such as strain enhanced-solid oxide fuel cells.

In a nutshell, flexible and efficient liquid phase thin film deposition technique is developed in the framework of this thesis and exemplified on a variety of systems with different structural and functional requirements. Moreover, an insight to the fundamental processing issues is also

provided. Using the approach developed here as a basis, road to many other fascinating thin film materials can be paved – there is plenty of room to explore!

Bibliography

[1]   R. W. Schwartz, T. Schneller, R. Waser, C. R. Chimie 2004, 7, 433.

[2]   E. Berger, W. Geffcken, *German Patent*, 736 411, May 1939.

[3]   H. Schroeder, Opt. Acta 1962, 9, 249-254.

[4]   T. Schneller, S. B. Majumder, R. Waser, in *Ceramics Science and Technology*, Wiley-VCH Verlag GmbH & Co. KGaA, 2008, 443.

[5]   C. Kittel, Rev. Mod. Phys. 1949, 21, 541.

[6]   D. L. Leslie-Pelecky, R. D. Rieke, Chem. Mater. 1996, 8, 1770.

[7]   N. A. Spaldin, N. A. Spaldin, *Ferromagnetic domain, Magnetic Materials*, Cambridge University Press, 2010.

[8]   N. A. Spaldin, N. A. Spaldin, *Anisotropy*, *Magnetic Materials*, Cambridge University Press, 2010.

[9]   R. P. Cowburn, J. Appl. Phys. 2003, 93, 9310.

[10]   R. M. Bozorth, J. G. Walker, Phys. Rev. 1952, 88, 1209.

[11]   O. Caltun, G. S. N. Rao, K. H. Rao, B. Parvatheeswara Rao, I. Dumitru, C. O. Kim, C. Kim, J. Magn. Magn. Mater. 2007, 316, e618.

[12]   A. Grunwald, A. G. Olabi, Sensor Actuat. A- Phys. 2008, 144, 161.

[13]   K. Rabe, P. Ghosez, in *Physics of Ferroelectrics*, Vol. 105, Springer Berlin Heidelberg, 2007, 117.

[14]   E. Soergel, J. Phys. D: Appl. Phys. 2011, 44.

[15]   F. Wang, Y.-W. Mai, D. Wang, R. Ding, W. Shi, Sensor. Actuat. A: Phys. 2015, 233, 195.

[16]   M. Lines, Glass, A., *Principles and applications of ferroelectrics and related materials,* Oxford University Press, 2010, 102.

[17]   N. A. Pertsev, J. Rodríguez Contreras, V. G. Kukhar, B. Hermanns, H. Kohlstedt, R. Waser, Appl. Phys. Lett. 2003, 83, 3356; A. K. Tagantsev, Integr. Ferroelectr. 1997, 16, 237.

[18]   T. Nan, Z. Zhou, M. Liu, X. Yang, Y. Gao, B. A. Assaf, H. Lin, S. Velu, X. Wang, H. Luo, J. Chen, S. Akhtar, E. Hu, R. Rajiv, K. Krishnan, S. Sreedhar, D. Heiman, B. M. Howe, G. J. Brown, N. X. Sun, Sci. Rep. 2014, 4, 3688.

[19]   G. Lawes, G. Srinivasan, J. Phys. D: Appl. Phys. 2011, 44, 243001.

[20]   J. M. Rondinelli, M. Stengel, N. A. Spaldin, Nat. Nanotechnol. 2008, 3, 46.

[21]   Z. Zhou, B. M. Howe, M. Liu, T. Nan, X. Chen, K. Mahalingam, N. X. Sun, G. J. Brown, Sci. Rep. 2015, 5, 7740.

[22]   T. Wu, C. M. Chang, T. K. Chung, G. Carman, IEEE Trans. Magn. 2009, 45, 4333.

[23]   C. Schmitz-Antoniak, D. Schmitz, P. Borisov, F. M. F. de Groot, S. Stienen, A. Warland, B. Krumme, R. Feyerherm, E. Dudzik, W. Kleemann, H. Wende, Nat. Commun. 2013, 4, 2051.

[24]   J. L. Hockel, A. Bur, T. Wu, K. P. Wetzlar, G. P. Carman, Appl. Phys. Lett. 2012, 100, 022401; C. A. F. Vaz, J. Phys. Condens. Matter 2012, 24, 333201.

[25]   T. Wu, A. Bur, K. Wong, P. Zhao, C. S. Lynch, P. K. Amiri, K. L. Wang, G. P. Carman, Appl. Phys. Lett. 2011, 98.

[26]   T. Zhao, A. Scholl, F. Zavaliche, H. Zheng, M. Barry, A. Doran, K. Lee, M. P. Cruz, R. Ramesh, Appl. Phys. Lett. 2007, 90, 123104.

[27]   F. Zavaliche, T. Zhao, H. Zheng, F. Straub, M. P. Cruz, P. L. Yang, D. Hao, R. Ramesh, Nano Lett. 2007, 7, 1586.

[28]   R. V. Chopdekar, V. K. Malik, A. Fraile Rodríguez, L. Le Guyader, Y. Takamura, A. Scholl, D. Stender, C. W. Schneider, C. Bernhard, F. Nolting, L. J. Heyderman, Phys. Rev. B 2012, 86, 014408.

[29]   H. K. D. Kim, L. T. Schelhas, S. Keller, J. L. Hockel, S. H. Tolbert, G. P. Carman, Nano Lett. 2013, 13, 884.

[30]   M. Buzzi, R. V. Chopdekar, J. L. Hockel, A. Bur, T. Wu, N. Pilet, P. Warnicke, G. P. Carman, L. J. Heyderman, F. Nolting, Phys. Rev. Lett. 2013, 111, 027204.

[31]   S.-W. Yang, R.-C. Peng, T. Jiang, Y.-K. Liu, L. Feng, J.-J. Wang, L.-Q. Chen, X.-G. Li, C.-W. Nan, Adv. Mater. 2014, 26, 7091.

[32]   N. A. Spaldin, N. A. Spaldin, *Magneto-optics and magneto-optic recording, Magnetic Materials*, Cambridge University Press, 2010.

[33]   G. v. d. Laan, JPCS 2013, 430, 012127.

[34]   W. R. Mason, in *A Practical Guide to Magnetic Circular Dichroism Spectroscopy*, John Wiley & Sons, Inc., 2006, 1.

[35]   E. Beaurepaire, H. Bulou, F. Scheurer, Springer, Berlin/Heidelberg 2010, 149.

[36]   A. Cavallin, F. D. Natterer, S. Ouazi, G. Moulas, A. Lehnert, S. Rusponi, and H. Brune, Phys. Rev. B, 2014, 90, 14427

[37]   P. Ferraro, S. Grilli, P. De Natale, *Ferroelectric crystrals for photonic applications,* Springer, Berlin/Heidelberg 2013, 205.

[38]   V. V. Shvartsman, A. L. Kholkin, in *Multifunctional Polycrystalline Ferroelectric Materials*, Vol. 140, Springer Netherlands, 2011, 409.

[39]   S. Jesse, A. P. Baddorf, S. V. Kalinin, Appl. Phys. Lett. 2006, 88, 062908.

[40]   C. J. Brinker, in *Chemical Solution Deposition of Functional Oxide Thin Films*, (Eds: T. Schneller, R. Waser, M. Kosec, D. Payne), Springer Vienna, 2013, 233.

[41]   T. Rehg, B. Higgins, AIChE Journal 1992, 38, 489.

[42]   D. P. Birnie Iii, J. Mater. Res. 2001, 16, 1145.

[43]   D. Birnie, III, in *Chemical Solution Deposition of Functional Oxide Thin Films*, (Eds: T. Schneller, R. Waser, M. Kosec, D. Payne), Springer Vienna, 2013, 263.

[44]   M. Brubaker, in *Chemical Solution Deposition of Functional Oxide Thin Films*, (Eds: T. Schneller, R. Waser, M. Kosec, D. Payne), Springer Vienna, 2013, 275.

[45]   F. J. Heiligtag, M. Niederberger, Mater. Today 2013, 16, 262.

[46]   in *Metal Oxide Nanoparticles in Organic Solvents*, Springer London, 2009, 53.

[47]   M. Niederberger, Acc. Chem. Res. 2007, 40, 793.

[48]   G. Garnweitner, M. Niederberger, J. Mater. Chem. 2008, 18, 1171; G. Garnweitner, M. Niederberger, J. Amer. Ceram. Soc. 2006, 89, 1801.

[49]   I. Bilecka, M. Niederberger, Nanoscale 2010, 2, 1358.

[50]   M. Niederberger, in *Microwaves in Nanoparticle Synthesis*, Wiley-VCH Verlag GmbH & Co. KGaA, 2013, 185.

[51]   Q. J. Cai, Y. Gan, M. B. Chan-Park, H. B. Yang, Z. S. Lu, C. M. Li, J. Guo, Z. L. Dong, Chem. Mater. 2009, 21, 3153.

[52]   R. W. Schwartz, T. Schneller, R. Waser, C. R. Chim 2004, 7, 433.

[53]   H. B. Sharma, Ferroelectrics 2013, 453, 113.

[54]   H. C. S. Andrade, L. Seara, W. Fadgen, N. S. Mohallem, J. Sol-Gel Sci. Technol. 2012, 64, 543; C. Yu-Chi, X. Ren-Yang, W. Yeong-Her, IEEE Trans. Electron Devices 2014, 61, 4090.

[55]   B. MaliČ, H. Suzuki, J. Ceram. Soc. Jpn. 2014, 122, 1.

[56]   R. Ashiri, A. Nemati, M. Sasani Ghamsari, Ceram. Int. 2014, 40, 8613.

[57]   P. Ferreira, R. Z. Hou, A. Wu, M.-G. Willinger, P. M. Vilarinho, J. Mosa, C. Laberty-Robert, C. Boissière, D. Grosso, C. Sanchez, Langmuir 2012, 28, 2944.

[58]   N. Suzuki, X. Jiang, R. R. Salunkhe, M. Osada, Y. Yamauchi Chem. Eur. J. 2014, 20, 11283.

[59]   T. M. Stawski, W. J. C. Vijselaar, O. F. Göbel, S. A. Veldhuis, B. F. Smith, D. H. A. Blank, J. E. ten Elshof, Thin Solid Films 2012, 520, 4394; Z. G. Hong Zhu, Wein-Duo Yang, Wein-Feng Chang, Adv. Mater. Res. 2012, 581-582, 514.

[60]   S. Glinšek, B. Malič, M. Kosec, in *Chemical Solution Deposition of Functional Oxide Thin Films*, (Eds: T. Schneller, R. Waser, M. Kosec, D. Payne), Springer Vienna, 2013, 431.

[61]   H.-c. He, M.-h. Ying, J.-p. Zhou, C.-W. Nan, J. Electroceram. 2008, 21, 686; N. D. S. Mohallem, L. M. Seara, M. A. Novak, E. H. C. P. Sinnecker, Braz. J. Phys. 2006, 36, 1078; A. Ghasemi, J. Alloy. Compd. 2015, 645, 467.

[62]   N. C. Pramanik, T. Fujii, M. Nakanishi, J. Takada, J. Mater. Chem. 2004, 14, 3328.

[63]   W. Chen, W. Zhu, J. Am. Ceram. Soc. 2011, 94, 1096.

[64]   J.-G. Lee, J. Y. Park, Y.-J. Oh, C. S. Kim, J. Appl. Phys. 1998, 84, 2801; M. Sedlář, V. Matějec, T. Grygar, J. Kadlecová, Ceram. Int. 2000, 26, 507.

[65]   D. G. L. W. Rao, H. C. Yan, Adv. Mater. Res. 2013, 744, 315; A. Akbar, S. Riaz, R. Ashraf, S. Naseem, J. Sol Gel Sci. Technol. 2015, 74, 320.

[66]   K. J. Kim, M. H. Kim, C. S. Kim, J. Mag. 2014, 19, 111; L. Wang, H. Dong, J. Li, J. Hua, S. Xu, M. Feng, H. Li, Ceram. Int. 2014, 40, 10323; S. Seifikar, T. Rawdanowicz, W. Straka, C. Quintero, N. Bassiri-Gharb, J. Schwartz, J. Magn. Magn. Mater. 2014, 361, 255.

[67]   M. Mustaqima, M. Y. Lee, D. H. Kim, B. W. Lee, C. Liu, J. Mag. 2014, 19, 227; S. Seifikar, B. Calandro, G. Rasic, E. Deeb, J. Yang, N. Bassiri-Gharb, J. Schwartz, J. Am. Ceram. Soc. 2013, 96, 3050.

[68]   P. Navuduri, I. M. Abdel-Motaleb, Y. Z. Yoo, O. Chmaissem, "Characterization of large area PLD grown combinatorial compositions of barium strontium titanium oxides", presented at *ICSICT-2006: 2006 8th Int. Conf. on Solid-State and Integrated Circuit Technology, Proc.*, 2007.

[69]   E. F. Alberta, W. S. Hackenberger, "Cryogenic ceramic multilayer capacitors for power electronics", presented at *AIP Conf. Proc.*, 2006; M. J. Pan, C. Randall, IEEE Electr. Insul. M. 2010, 26, 44.

[70]   X. Chen, C. H. Jia, Y. H. Chen, G. Yang, W. F. Zhang, J. Phys. D Appl. Phys. 2014, 47, 36.

[71]   R. V. Chopdekar, V. K. Malik, A. Fraile Rodríguez, L. Le Guyader, Y. Takamura, A. Scholl, D. Stender, C. W. Schneider, C. Bernhard, F. Nolting, L. J. Heyderman, Phys. Rev. B 2012, 86, 014408.

[72]   R. Grigalaitis, M. M. Vijatović Petrović, J. D. Bobić, A. Dzunuzovic, R. Sobiestianskas, A. Brilingas, B. D. Stojanović, J. Banys, Ceram. Int. 2014, 40, 6165; H. Zhang, X. H. Wang, Z. B. Shen, Y. N. Hao, Adv. Mat. Res. 2014, 833, 8.

[73]   Z. Liu, P. T. Lin, B. W. Wessels, J. Opt. A-Pure Appl. Op. 2008, 10, 015302; Z. Liu, P. T. Lin, B. W. Wessels, F. Yi, S. T. Ho, Appl. Phys. Lett. 2007, 90, 201104.

[74]   N. Spaldin, in *Introduction to the theory of Ferroelectrics*, 2011, 195.

[75]   X. Y. Wang, Y. L. Wang, R. J. Yang, Appl. Phys. Lett. 2009, 95.

[76]   M. Ahmadi, N. Phonthammachai, T. H. Shuan, T. J. White, N. Mathews, S. G. Mhaisalkar, Org. Electron. 2010, 11, 1660; W. Ousi-Benomar, S. S. Xue, R. A. Lessard, A. Singh, Z. L. Wu, P. K. Kuo, J. Mater. Res. 1994, 9, 970; T. Dechakupt, S. Ko, S.-G. Lu, C. Randall, S. Trolier-McKinstry, J Mater Sci 2011, 46, 136.

[77]   E. G. Bakhoum, M. H. M. Cheng, J. Microelectromech. Syst 2010, 19, 443; N. Dai, G. J. Hu, X. K. Hong, J. L. Shang, "Fabrication and optical properties of ferroelectric microcavities fabricated by chemical solution deposition", 2008; R. Dorey, in *Ceramic Thick Films for MEMS and Microdevices*, (Ed: R. Dorey), William Andrew Publishing, Oxford 2012, 35.

[78]   J. He, J. C. Jiang, J. Liu, G. Collins, C. L. Chen, B. Lin, V. Giurgiutiu, R. Y. Guo, A. Bhalla, E. I. Meletis, J. Nanosci. Nanotechno. 2010, 10, 6245; A. Ianculescu, B. Despax, V. Bley, T. Lebey, R. Gavrilă, N. Drăgan, J. Eur. Ceram. Soc. 2007, 27, 1129; T. Osumi, M.

Nishide, H. Funakubo, H. Shima, K. Nishida, T. Yamamoto, Integr. Ferroelectr. 2012, 133, 42.

[79]   C. H. Jung, S. I. Woo, Y. S. Kim, K. S. No, Thin Solid Films 2011, 519, 3291.

[80]   P. S. Patil, Mater. Chem. Phys. 1999, 59, 185.

[81]   J. L. M. Rupp, B. Scherrer, N. Schäuble, L. J. Gauckler, Adv. Funct. Mater. 2010, 20, 2807.

[82]   B. Scherrer, S. Heiroth, R. Hafner, J. Martynczuk, A. Bieberle-Hütter, J. L. M. Rupp, L. J. Gauckler, Adv. Funct. Mater. 2011, 21, 3967.

[83]   M. Kosec, D. Kuscer, J. Holc, in *Multifunctional Polycrystalline Ferroelectric Materials*, Vol. 140, Springer Netherlands, 2011, 39.

[84]   J. Ba, J. Polleux, M. Antonietti, M. Niederberger, Adv. Mater. 2005, 17, 2509; J. M. Szeifert, J. M. Feckl, D. Fattakhova-Rohlfing, Y. Liu, V. Kalousek, J. Rathousky, T. Bein, J. Am. Chem. Soc. 2010, 132, 12605; K. Fominykh, J. M. Feckl, J. Sicklinger, M. Döblinger, S. Böcklein, J. Ziegler, L. Peter, J. Rathousky, E.-W. Scheidt, T. Bein, D. Fattakhova-Rohlfing, Adv. Funct. Mater. 2014, 24, 3123; A. Aboulaich, O. Lorret, B. Boury, P. H. Mutin, Chem. Mater. 2009, 21, 2577.

[85]   C. Grote, T. A. Cheema, G. Garnweitner, Langmuir 2012, 28, 14395.

[86]   J. H. Prosser, T. Brugarolas, S. Lee, A. J. Nolte, D. Lee, Nano Lett. 2012, 12, 5287.

[87]   K. T. Cook, K. E. Tettey, R. M. Bunch, D. Lee, A. J. Nolte, ACS Appl. Mater. Interfaces 2012, 4, 6426.

[88]   C. S. Thompson, R. A. Fleming, M. Zou, Sol. Energ. Mat. Sol. Cells 2013, 115, 108.

[89]   S. Colodrero, M. Ocaña, H. Míguez, Langmuir 2008, 24, 4430; M. E. Calvo, S. Colodrero, T. C. Rojas, J. A. Anta, M. Ocaña, H. Míguez, Adv. Funct. Mater. 2008, 18, 2708.

[90]   D. P. Puzzo, L. D. Bonifacio, J. Oreopoulos, C. M. Yip, I. Manners, G. A. Ozin, J. Mater. Chem. 2009, 19, 3500.

[91]   L. Luo, D. Bozyigit, V. Wood, M. Niederberger, Chem. Mater. 2013, 25, 4901.

[92]   R. Ashiri, A. Nemati, M. Sasani Ghamsari, Ceramics International 2014, 40, 8613; Y. Chang, R. Xue, Y. Wang, IEEE Trans. Electron Devices 2014, 61, 4090.

[93]   P. Ferreira, R. Z. Hou, A. Wu, M.-G. Willinger, P. M. Vilarinho, J. Mosa, C. Laberty-Robert, C. Boissière, D. Grosso, C. Sanchez, Langmuir 2011, 28, 2944.

[94]   R. Ayouchi, F. Martín, J. R. Ramos-Barrado, D. Leinen, Surf. Interface Anal. 2000, 30, 565.

[95]   M. Niederberger, G. Garnweitner, "Nonaqueous synthesis of barium titanate nanocrystals in acetophenone as oxygen supplying agent", presented at *Mater. Res. Soc. Symp. Proc.*, 2005.

[96]   M. Niederberger, G. Garnweitner, N. Pinna, M. Antonietti, J. Am. Chem. Soc. 2004, 126, 9120.

[97]   K. Page, T. Proffen, M. Niederberger, R. Seshadri, Chem. Mater. 2010, 22, 4386.

[98]   D. Taroata, W. Fischer, T. A. Cheema, G. Garnweitner, G. Schmid, IEEE Trans. Dielectr. Electr. Insul. 2012, 19, 298.

[99]   A. Bele, M. Cazacu, G. Stiubianu, S. Vlad, R. Soc. Chem. Adv. 2014, 4, 58522.

[100]   S. H. Jhung, J.-H. Lee, J. W. Yoon, Y. K. Hwang, J.-S. Hwang, S.-E. Park, J.-S. Chang, Mater. Lett. 2004, 58, 3161.

[101]   M. Yashima, T. Hoshina, D. Ishimura, S. Kobayashi, W. Nakamura, T. Tsurumi, S. Wada, J. Appl. Phys. 2005, 98.

[102]   E. Zolotoyabko, J. L. M. Rupp, L. J. Gauckler, Scripta Mater. 2012, 66, 190.

[103]   M. B. Smith, K. Page, T. Siegrist, P. L. Redmond, E. C. Walter, R. Seshadri, L. E. Brus, M. L. Steigerwald, J. Am. Chem. Soc. 2008, 130, 6955.

[104]   H. Z. Guo, Z. H. Chen, B. L. Cheng, H. B. Lu, L. F. Liu, Y. L. Zhou, J. Eur. Ceram. Soc. 2005, 25, 2347.

[105]   K. Tsuzuku, M. Couzi, J Mater Sci 2012, 47, 4481.

[106] M. Ejaz, V. S. Puli, R. Elupula, S. Adireddy, B. C. Riggs, D. B. Chrisey, S. M. Grayson, J. Polym. Sci., Part A: Polym. Chem. 2014.

[107] R. Ashiri, Metall. Mater. Trans. A 2012, 43, 4414.

[108] D. Olmos, E. V. Martin, J. Gonzalez-Benito, Phys. Chem. Chem. Phys 2014, 16, 24339.

[109] T. A. Cheema, G. Garnweitner, CrystEngComm 2014, 16, 3366.

[110] D. K. Takci, E. Senadim Tuzemen, K. Kara, S. Yilmaz, R. Esen, O. Baglayan, J. Mater. Sci. - Mater. Electron. 2014, 25, 2078.

[111] Y. Garbovskiy, A. Glushchenko, Appl. Optics 2013, 52, E34.

[112] S. Ramakanth, K. C. James Raju, J. Appl. Phys. 2014, 115, 173507.

[113] J. S. Zhu, X. M. Lu, W. Jiang, W. Tian, M. Zhu, M. S. Zhang, X. B. Chen, X. Liu, Y. N. Wang, J. Appl. Phys. 1997, 81, 1392.

[114] Y. Garbovskiy, A. Glushchenko, Appl. Optics 2013, 52, E34.

[115] W. H. P. Pernice, X. Chi, F. J. Walker, H. X. Tang, IEEE Photon. Technol. Lett. 2014, 26, 1344.

[116] S. Roy, S. B. Majumder, J. Appl. Phys. , 2012, 112, 043520.

[117] K. Tanaka, K. Suzuki, D. Fu, K. Nishizawa, T. Miki, K. Kato, Jpn. J. Appl. Phys. 1 2004, 43, 6525.

[118] T. Jungk, Á. Hoffmann, E. Soergel, in *Ferroelectric Crystals for Photonic Applications*, Vol. 91 (Eds: P. Ferraro, S. Grilli, P. De Natale), Springer Berlin Heidelberg, 2014, 205.

[119] P. Ferreira, R. Z. Hou, A. Wu, M. G. Willinger, P. M. Vilarinho, J. Mosa, C. Laberty-Robert, C. Boissière, D. Grosso, C. Sanchez, Langmuir 2012, 28, 2944.

[120] I. Bilecka, I. Djerdj, M. Niederberger, Chem. Commun. 2008, 886.

[121] D. Mergel, Thin Solid Films 2001, 397, 216.

[122] H. B. Sharma, Int. J. Mod. Phys. B 2007, 21, 1837.

[123] A. A. Bagade, V. V. Ganbavle, K. Y. Rajpure, J. Mater. Eng. Perform. 2014, 23, 2787.

[124] H. Yanagihara, Y. Utsumi, T. Niizeki, J. Inoue, E. Kita, J. Appl. Phys. 2014, 115, 17A719.

[125] J. G. Barbosa, M. R. Pereira, C. Moura, J. A. Mendes, B. G. Almeida, Ferroelectrics 2011, 421, 66.

[126] C. Shu, H. Qiao, "Tuning magnetic properties of magnetic recording media cobalt ferrite nano-particles by co-precipitation method", presented at *Symp. Photonics Optoelectronics, 2009 IEEE*, 2009.

[127] O. F. Caltun, G. S. N. Rao, K. H. Rao, B. Parvatheeswara Rao, C. G. Kim, C. O. Kim, I. Dumitru, N. Lupu, H. Chiriac, Sensor Lett. 2007, 5, 45.

[128] W. Hu, L. Zou, R. Chen, W. Xie, X. Chen, N. Qin, S. Li, G. Yang, D. Bao, Appl. Phys. Lett. 2014, 104, 143502.

[129] N. Hiratsuka, M. Nozawa, K. Kakizaki, J. Magn. Magn. Mater. 1997, 176, 31.

[130] W. Rao, Y. B. Wang, Y. A. Wang, J. X. Gao, W. L. Zhou, J. Yu, in *Adv. Mat. Res.*, Vol. 750-752, 2013, 1024.

[131] A. Lisfi, C. M. Williams, L. T. Nguyen, J. C. Lodder, A. Coleman, H. Corcoran, A. Johnson, P. Chang, A. Kumar, W. Morgan, Phys. Rev. B 2007, 76, 054405.

[132] L. Stichauer, G. Gavoille, Z. Simsa, J. Appl. Phys. 1996, 79, 3645.

[133] F. Choueikani, F. Royer, D. Jamon, A. Siblini, J. J. Rousseau, S. Neveu, J. Charara, Appl. Phys. Lett. 2009, 94, 051113.

[134] T. Osaka, T. Asahi, J. Kawaji, T. Yokoshima, Electrochim. Acta 2005, 50, 4576.

[135] X. W. Wang, Y. Q. Zhang, H. Meng, Z. J. Wang, Z. D. Zhang, J. Alloy Compd. 2011, 509, 7803.

[136] I. Bilecka, M. Kubli, E. Amstad, M. Niederberger, J. Sol-Gel Sci. Technol. 2011, 57, 313.

[137] T. Niizeki, Y. Utsumi, R. Aoyama, H. Yanagihara, J. I. Inoue, Y. Yamasaki, H. Nakao, K. Koike, E. Kita, Appl. Phys. Lett. 2013, 103, 162407; C. Y. Tsai, H. R. Chen, F. C. Chang, W. C. Tsai, H. M. Cheng, Y. H. Chu, C. H. Lai, W. F. Hsieh, Appl. Phys. Lett. 2013, 102, 132905.

[138] S. D. Sathaye, K. R. Patil, S. D. Kulkarni, P. P. Bakre, S. D. Pradhan, B. D. Sarwade, S. N. Shintre, J. Mater. Sci. 2003, 38, 29.

[139] Y. Kitamoto, S. Kantake, F. Shirasaki, M. Abe, M. Naoe, J. Appl. Phys. 1999, 85, 4708.

[140] R. H. Gonçalves, B. H. R. Lima, E. R. Leite, J. Am. Chem. Soc. 2011, 133, 6012.

[141] D. Erdem, Y. Shi, F. J. Heiligtag, A. C. Kandemir, E. Tervoort, J. L. M. Rupp, M. Niederberger, J. Mater. Chem. C 2015, 3, 9833.

[142] M. Kubli, L. Luo, I. Bilecka, M. Niederberger, Chimia 2010, 64, 170.

[143] D. Taroata, W. Fischer, T. A. Cheema, G. Garnweitner, G. Schmid, IEEE Trans. Dielect. Elect. Insulation 2012, 19, 298.

[144] F. J. Heiligtag, N. Kränzlin, M. J. Süess, M. Niederberger, J. Sol-Gel Sci. Technol. 2014, 70, 300.

[145] P. R. Graves, C. Johnston, J. J. Campaniello, Mater. Res. Bull. 1988, 23, 1651; M. A. G. Soler, T. F. O. Melo, S. W. da Silva, E. C. D. Lima, A. C. M. Pimenta, V. K. Garg, A. C. Oliveira, P. C. Morais, J. Magn. Magn. Mater. 2004, 272–276, Part 3, 2357.

[146] R. C. Pedroza, S. W. da Silva, M. A. G. Soler, P. P. C. Sartoratto, D. R. Rezende, P. C. Morais, J. Magn. Magn. Mater. 2005, 289, 139.

[147] A. Bertoluzza, C. Fagnano, M. A. Morelli, M. Guglielmi, G. Scarinci, N. Maliavski, J. Raman Spec. 1988, 19, 297.

[148] D. L. A. de Faria, S. Venâncio Silva, M. T. de Oliveira, J. Raman Spectrosc. 1997, 28, 873.

[149] S. Roy, S. B. Majumder, Journal of Applied Physics 2012, 112.

[150] R. C. Rai, S. Wilser, M. Guminiak, B. Cai, M. L. Nakarmi, Appl. Phys. A: Mater. Sci. Process. 2012, 106, 207.

[151] B. S. Holinsworth, D. Mazumdar, H. Sims, Q. C. Sun, M. K. Yurtisigi, S. K. Sarker, A. Gupta, W. H. Butler, J. L. Musfeldt, Appl. Phys. Lett. 2013, 103, 082406.

[152] T. E. Quickel, V. H. Le, T. Brezesinski, S. H. Tolbert, Nano Lett. 2010, 10, 2982.

[153] P. Jeppson, R. Sailer, E. Jarabek, J. Sandstrom, B. Anderson, M. Bremer, D. G. Grier, D. L. Schulz, A. N. Caruso, S. A. Payne, P. Eames, M. Tondra, H. He, D. B. Chrisey, J. Appl. Phys. 2006, 100, 114324.

[154] D. Peddis, C. Cannas, A. Musinu, G. Piccaluga, Chem. Eur. J. 2009, 15, 7822.

[155] J. A. Moyer, C. A. F. Vaz, D. P. Kumah, D. A. Arena, V. E. Henrich, Phys. Rev. B 2012, 86, 174404.

[156] J. F. Hochepied, P. Sainctavit, M. P. Pileni, J. Magn. Magn. Mater. 2001, 231, 315.

[157] B. S. Holinsworth, D. Mazumdar, H. Sims, Q.-C. Sun, M. K. Yurtisigi, S. K. Sarker, A. Gupta, W. H. Butler, J. L. Musfeldt, Appl. Phys. Lett. 2013, 103, 082406.

[158] N. A. Spaldin, N. A. Spaldin, *Ferrimagnetism, Magnetic Materials*, Cambridge University Press, 2010.

[159] C. Pereira, A. M. Pereira, C. Fernandes, M. Rocha, R. Mendes, M. P. Fernández-García, A. Guedes, P. B. Tavares, J.-M. Grenèche, J. P. Araújo, C. Freire, Chem. Mater. 2012, 24, 1496.

[160] M. Grigorova, H. J. Blythe, V. Blaskov, V. Rusanov, V. Petkov, V. Masheva, D. Nihtianova, L. M. Martinez, J. S. Muñoz, M. Mikhov, J. Magn. Magn. Mater. 1998, 183, 163.

[161] K. L. Lopez Maldonado, P. de la Presa, M. A. de la Rubia, P. Crespo, J. de Frutos, A. Hernando, J. A. Matutes Aquino, J. T. Elizalde Galindo, J. Nanopart. Res. 2014, 16, 1.

[162] A. T. Ngo, P. Bonville, M. P. Pileni, J. Appl. Phys. 2001, 89, 3370.

[163] Q. C. Sun, C. S. Birkel, J. Cao, W. Tremel, J. L. Musfeldt, ACS Nano 2012, 6, 4876.

[164] C. Vázquez-Vázquez, M. A. López-Quintela, M. C. Buján-Núñez, J. Rivas, J. Nanopart. Res. 2011, 13, 1663.

[165] J. Barbosa, B. Almeida, A. M. Pereira, J. P. Araújo, I. Gomes, J. Mendes, J. Non-Cryst. Solids 2008, 354, 5250.

[166] C. Suchomski, C. Reitz, D. Pajic, Z. Jaglicic, I. Djerdj, T. Brezesinski, Chem.Mater. 2014, 26, 2337.

[167] S. Küçükdermenci, D. Kutluay, Y. Avgýn, Mater. Tehnol. 2013, 47, 71.

[168] K. P. Polyakova, V. A. Seredkin, V. V. Polyakov, A. A. Lepeshev, V. F. Pavlov, "Deposition and properties of polycrystalline cobalt ferrite films for magneto-optical recording", presented at *Proceedings of SPIE - The International Society for Optical Engineering*, 1997.

[169] D. E. Achatz, F. J. Heiligtag, X. Li, M. Link, O. S. Wolfbeis, Sensors Actuat. B-Chem. **2010**, 150, 211.

[170] J.-M. Hu, Z. Li, L.-Q. Chen, C.-W. Nan, Adv. Mater. 2012, 24, 2869.

[171] A. Roy, R. Gupta, A. Garg, Adv. Cond. Matter Phys. 2012, 2012, 926290.

[172] H. Ishiwara, J. Nanosci. Nanotechnol. 2012, 12, 7619; V. Garcia, M. Bibes, Nat. Commun. 2014, 5, 4289.

[173] X. Lu, Y. Kim, S. Goetze, X. Li, S. Dong, P. Werner, M. Alexe, D. Hesse, Nano Lett. 2011, 11, 3202.

[174] N. Ortega, A. Kumar, J. F. Scott, R. S. Katiyar, J. Phys. Condens. Matter 2015, 27, 504002.

[175] L. Wang, D. Wang, Q. Cao, Y. Zheng, H. Xuan, J. Gao, Y. Du, Sci. Rep. 2012, 2, 223.

[176] W. Eerenstein, N. D. Mathur, J. F. Scott, Nature 2006, 442, 759; F. Zavaliche, H. Zheng, L. Mohaddes-Ardabili, S. Y. Yang, Q. Zhan, P. Shafer, E. Reilly, R. Chopdekar, Y. Jia, P. Wright, D. G. Schlom, Y. Suzuki, R. Ramesh, Nano Lett. 2005, 5, 1793; C.-W. Nan, M. I. Bichurin, S. Dong, D. Viehland, G. Srinivasan, J. Appl. Phys. 2008, 103, 031101.

[177] F. Manfred, J. Phys. D: Appl. Phys. 2005, 38, R123.

[178] N. A. Hill, J. Phys. Chem. B 2000, 104, 6694.

[179] R. Ramesh, N. A. Spaldin, Nat Mater 2007, 6, 21.

[180] M. Etier, C. Schmitz-Antoniak, S. Salamon, H. Trivedi, Y. Gao, A. Nazrabi, J. Landers, D. Gautam, M. Winterer, D. Schmitz, H. Wende, V. V. Shvartsman, D. C. Lupascu, Acta Mater. 2015, 90, 1.

[181] Y. Shen, J. Sun, L. Li, Y. Yao, C. Zhou, R. Su, Y. Yang, J. Mater. Chem. C 2014, 2, 2545.

[182] S. H. Xie, Y. Y. Liu, J. Y. Li, Front. Phys. 2012, 7, 399.

[183] L. Zhang, J. Zhai, W. Mo, X. Yao, J. Amer. Ceram. Soc. 2010, 93, 3267; Y. Q. Liu, B. Zhang, Y. H. Wu, J. Zhang, D. Li, Y. Liu, M. B. Wei, J. H. Yang, Superlattice. Microst. 2013, 61, 174.

[184] P. Zhao, Z. Zhao, D. Hunter, R. Suchoski, C. Gao, S. Mathews, M. Wuttig, I. Takeuchi, Appl. Phys. Lett. 2009, 94, 243507.

[185] V. Tileli, M. Duchamp, A. K. Axelsson, M. Valant, R. E. Dunin-Borkowski, N. M. Alford, Nanoscale 2015, 7, 218.

[186] L. Zhu, Y. Dong, X. Zhang, Y. Yao, W. Weng, G. Han, N. Ma, P. Du, J. Alloys Compd. 2010, 503, 426; W. Chen, S. Shannigrahi, X. F. Chen, Z. H. Wang, W. Zhu, O. K. Tan, Solid State Commun. 2010, 150, 271; H. R. C. S. Andrade, L. M. Seara, N. D. S. Mohallem, "Synthesis and characterization of $BaTiO_3/CoFe_2O_4$ thin films", presented at *MRS Proceedings*, 2011; Y.-D. Xu, G. Wu, H.-L. Su, M. Shi, G.-Y. Yu, L. Wang, J. Alloys Compd. 2011, 509, 3811; Y. L. Dong, P. Y. Du, W. J. Weng, G. R. Han, G. L. Zhao, J. Electroceram. 2008, 21, 327.

[187]   J. C. Wang, P. Zheng, R. Q. Yin, L. M. Zheng, J. Du, L. Zheng, J. X. Deng, K. X. Song, H. B. Qin, Ceram. Int. 2015; F. Wang, Y. W. Mai, D. Wang, R. Ding, W. Shi, Sensor. Actuat. A-Phys. 2015, 233, 195.

[188]   K. K. Mohaideen, P. A. Joy, J. Eur. Ceram. Soc. 2014, 34, 677.

[189]   V. K. Verma, V. R. Singh, K. Ishigami, G. Shibata, T. Harano, T. Kadono, A. Fujimori, F. H. Chang, H. J. Lin, D. J. Huang, C. T. Chen, Y. Zhang, J. Liu, Y. Lin, C.-W. Nan, A. Tanaka, Phys. Rev. B 2014, 89, 115128; F. Aguesse, A.-K. Axelsson, M. Valant, N. M. Alford, Scr. Mater. 2012, 67, 249.

[190]   R. C. Rai, S. Wilser, M. Guminiak, B. Cai, M. L. Nakarmi, Appl. Phys. A: Mater. Sci. Process. 2012, 106, 207.

[191]   S. Roy, S. B. Majumder, J. Appl. Phys. 2012, 112, 043520.

[192]   A. Gruverman, A. Kholkin, A. Kingon, H. Tokumoto, Appl. Phys. Lett. 2001, 78, 2751.

[193]   G. Caruntu, A. Yourdkhani, M. Vopsaroiu, G. Srinivasan, Nanoscale 2012, 4, 3218; S. S. Hongliang Lu, Xiaofeng Gu, Shuli He, Chonglin Chen, Gangbing Song, Zhonghou Cai, Haiming Guo, Hongjun Gao, Li Sun, J. Nano R. 2013, 22, 23; K.-i. Mimura, K. Hiramatsu, W. Sakamoto, T. Yogo, Mater. Lett. 2012, 89, 40.

[194]   S. Roy, S. B. Majumder, Phys. Lett. A 2011, 375, 1538.

[195]   J. T. S. Irvine, D. C. Sinclair, A. R. West, Adv. Mater. 1990, 2, 132.

[196]   R. Grigalaitis, M. M. Vijatović Petrović, J. D. Bobić, A. Dzunuzovic, R. Sobiestianskas, A. Brilingas, B. D. Stojanović, J. Banys, Ceram. Int. 2014, 40, 6165.

[197]   J. Mohapatra, A. Mitra, D. Bahadur, M. Aslam, J. Alloy. Compd. 2015, 628, 416.

[198]   M. Niederberger, G. Garnweitner, "Nonaqueous synthesis of barium titanate nanocrystals in acetophenone as oxygen supplying agent", presented at *Mater. Res. Soc. Symp. Proc.*, 2005.

Appendix

Declaration

I am very grateful to the collaborators who helped me with their expertise to conduct the research within the framework of this Ph.D. thesis. Through combining our fields of expertise, we were able to produce results of scientific nature and contribute to literature. I cordially thank to the colloborators whose names and contributions are listed below:

Chapter 2 Single component $BaTiO_3$ thin films:

Yanuo Shi (D-MATL, ETH Zurich) performed the sputter deposition of Pt electrodes in clean room conditions. Dr. Florian J. Heiligtag (D-MATL, ETH Zurich) carried out the IR measurements and helped with the discussion of the data and nanoparticle synthesis. Ayse Cagil Kandemir (D-MATL, ETH Zurich) provided support with the standard topography measurements with AFM. Dr. Elena Tervoort (D-MATL, ETH Zurich) took the TEM images of the as-synthesized $BaTiO_3$ nanoparticles.

Chapter 3 $CoFe_2O_4$ - SiO_2 nanocomposite thin films:

Dr. Nicholas Bingham (D-MATL, ETH Zurich and Paul Scherrer Institute) helped with the acquisition and discussion of magnetic, magneto-optical and synchrotron measurements' data. Dr. Florian J. Heiligtag (D-MATL, ETH Zurich) synthesized the dispersion of SiO_2 nanoparticles. Beamline scientists Dr. Nicolas Pilet (Swiss Light Source, Paul Scherrer Institute) and Dr. Peter Warnicke (Swiss Light Source, Paul Scherrer Institute) offered scientific and technical support during the synchrotron measurements and also discussion of the data.

Chapter 4 $BaTiO_3$ - $CoFe_2O_4$ magnetoelectric thin films

Dr. Nicholas Bingham (D-MATL, ETH Zurich and Paul Scherrer Institute) performed the VSM measurements, wrote the first proposal for the usage of PEEM beamline, supported all of the beamline measurements and helped with the discussion of the data. Dr. Florian J. Heiligtag helped during the acquisition of the synchrotron data. Dr. Nicolas Pilet (Swiss Light Source, Paul Scherrer Institute), Dr. Peter Warnicke (Swiss Light Source, Paul Scherrer Institute) and Dr. Carlos A.F. Vaz (Swiss Light Source, Paul Scherrer Institute) offered scientific and technical support during the synchrotron measurements and also discussion of the data. Yanuo Shi (D-MATL, ETH Zurich) carried out the Pt sputter deposition and provided the training to use the Gamry impedance measurement system. Dr. Michele Buzzi (Swiss Light Source, Paul Scherrer Institute) performed the PFM-assisted local poling of the synchrotron samples and provided technical support during the PEEM measurements.

Acknowledgements: